POLITECNICO DI TORINO

Collegio di Ingegneria Chimica e dei Materiali

Corso di Laurea Magistrale in
Ingegneria Chimica e dei Processi Sostenibili

Tesi di Laurea Magistrale

Alumina-silica aerogels functionalised with amino groups for CO_2 capture

Relatori
Prof. Luigi Manna
Prof. Mauro Banchero
Dott.ssa Marta Gallo

Candidata
Fabiana Mangano (s315751)

Anno Accademico 2023/2024

SOMMARIO ESTESO

La temperatura media globale è aumentata di circa 0.74 °C nel secolo scorso, con effetti più pronunciati sulla superficie terrestre rispetto a quella oceanica. Le emissioni di gas serra, fra cui l'anidride carbonica (CO_2), attribuite alle attività umane come la combustione di combustibili fossili e la deforestazione, sono identificate come principali responsabili del riscaldamento globale. Questo innalzamento della temperatura provoca una serie di conseguenze negative per i sistemi naturali, tra cui il disgelamento dei ghiacci e delle nevi, l'aumento dei livelli del mare e le interruzioni del ciclo idrologico. Per mitigare gli effetti negativi delle emissioni di CO_2, è necessario sviluppare tecnologie innovative ed efficienti per la sua cattura e stoccaggio (CCS). Le tecnologie correntemente utilizzate si basano sull'utilizzo di assorbenti liquidi per la cattura della CO_2, ma negli ultimi tempi si stanno cercando soluzioni alternative quali gli adsorbenti solidi come ad esempio gli aerogel. Gli aerogel di silice, in particolare, costituiscono una classe di materiali eccezionali con proprietà che li rendono particolarmente adatti per le applicazioni di cattura di CO_2. Questi materiali presentano una combinazione straordinaria di caratteristiche, tra cui un'alta superficie specifica, bassa densità, proprietà isolanti termiche eccellenti e porosità modulabile; tutto ciò li rende candidati ideali per lo sviluppo di adsorbenti di nuova generazione. Inoltre, l'incorporazione di ossidi metallici in qualità di gruppi funzionali all'interno della matrice degli aerogel di silice può migliorarne significativamente le capacità di assorbimento e selettività. È importante sottolineare che gli aerogel sono già validi adsorbenti, ma la loro selettività verso la CO_2 può essere migliorata mediante la funzionalizzazione della matrice.

Questo lavoro si concentra sulla sintesi di aerogel di silice-allumina funzionalizzati con ammine e sulla valutazione della loro efficacia nella cattura di CO_2. L'introduzione di gruppi amminici nella struttura porosa degli aerogel di silice, infatti, rappresenta un ulteriore strumento per conferire loro proprietà tali da renderli adatti come adsorbenti per la cattura della CO_2. Inoltre, questo tipo di materiale è stato sintetizzato per la prima volta all'interno di questo progetto di ricerca e non ha precedenti nella letteratura.

I campioni funzionalizzati di aerogel di silice-allumina (AlSi) sono stati preparati, tramite un processo one-pot, ovvero una procedura più rapida, semplice, economica rispetto ad una funzionalizzazione in più step. La funzionalizzazione con gruppi amminici è stata ottenuta tramite l'uso di (3-amminopropil) trimetossisilano (APTES) di cui si è variata la quantità aggiunta durante la sintesi: 2.5 mmol, 7.5 mmol e 22.5 mmol (le moli indicate sono quelle di APTES inserite rispetto a 30 mmol di silice).

I campioni così ottenuti sono stati caratterizzati per appurare le loro proprietà chimico-fisiche e sono anche stati sottoposti a test mirati a verificarne la capacità di adsorbire CO_2. Le sintesi degli aerogel di silice e allumina funzionalizzati con gruppi amminici sono risultate efficaci. In particolare, come è già stato sottolineato in precedenza, la funzionalizzazione di aerogel di allumina-silice mediante APTES rappresenta una novità rilevante nel panorama scientifico, in quanto non sono presenti precedenti in letteratura che descrivano tali materiali. Le caratterizzazioni hanno mostrato che gli aerogel di allumina-silice con o senza gruppi amminici sono stati sintetizzati con successo. Inoltre, si è osservato che l'aumento del contenuto di APTES porta ad un incremento della quantità di gruppi amminici presenti nell'aerogel, come evidenziato dagli spettri infrarossi (FTIR). Anche le analisi XPS confermano la presenza di azoto, e quindi di gruppi amminici, sulla superficie degli aerogel funzionalizzati.

Le analisi termogravimetriche (TGA) hanno rivelato che gli aerogel AlSi-APTES subiscono una perdita di peso significativa tra 150°C e 800°C, attribuibile alla degradazione di componenti organiche. Il campione con 22.5 mmol di APTES presenta la perdita di massa maggiore in questo intervallo di temperatura, pari al 32.8%, coerentemente con il più alto contenuto di specie organiche derivanti dall'ammina e, probabilmente, dai precursori.

Le isoterme di adsorbimento di azoto classificano i campioni come tipo IV con cappio di isteresi H1, tipico dei materiali mesoporosi. L'area superficiale BET diminuisce all'aumentare del contenuto di APTES, passando da 695 m^2/g per il campione con 2.5 mmol a 527 m^2/g per quello con 22.5 mmol. Anche il volume dei pori segue la stessa tendenza, variando da 1.5 cm^3/g a 1.2 cm^3/g. I risultati delle caratterizzazioni dimostrano che l'incorporazione di APTES durante il processo di sintesi influenza le proprietà degli aerogel di allumina-silice, in particolare diminuendone l'area superficiale e il volume dei pori, ma introducendo gruppi amminici, e rendendo, quindi, i campioni particolarmente promettenti per applicazioni di cattura della CO_2.

Le prove di assorbimento di CO_2 mostrano che gli aerogel AlSi-APTES con 2.5 mmol e 7.5 mml possono adsorbire circa 0.9 mmol/g di CO_2 a temperatura ambiente e pressione atmosferica. Non si osservano differenze significative tra i due campioni, suggerendo che la funzionalizzazione con un basso contenuto di APTES non conferisce un vantaggio apprezzabile in questo intervallo di composizione. Un risultato molto interessante si osserva nel caso del campione con 22.5 mmol che arriva ad assorbire fino a 2 mmol/g di anidride carbonica, indicando che sopra una certa soglia di contenuto di APTES si ha un significativo vantaggio nell'adsorbimento di CO_2. Inoltre, esperimenti condotti a basse pressioni parziali di CO_2 mostrano che anche i campioni con contenuto minore di ammine risultano vantaggiosi rispetto al campione non funzionalizzato in quanto assorbono più gas rispetto al campione di riferimento.

In conclusione, gli aerogel allumina-silice funzionalizzati con gruppi amminici rappresentano una classe di materiali estremamente promettenti per applicazioni di cattura e stoccaggio della CO_2. Le loro eccezionali proprietà strutturali e chimiche, unite all'elevata area superficiale e porosità, li rendono ideali per questo scopo. Un passaggio successivo potrebbe essere quello di effettuare dei test di adsorbimento con miscele di gas invece della CO_2 pura, per verificare se i campioni funzionalizzati presentano anche un vantaggio in termini di selettività.

Ulteriori ricerche saranno necessarie per ottimizzare le prestazioni di assorbimento e sviluppare processi di produzione su larga scala, ma i risultati ottenuti in questa tesi aprono la strada a nuove soluzioni per la mitigazione del cambiamento climatico.

ABSTRACT

To overcome climate challenges, emerging CO_2 capture technologies focus on innovative solid and chemical adsorbents like aerogels. Aerogels, in particular silica aerogel, have emerged as an exceptional class of materials with unique properties. In particular, functionalizing the silica matrix with metal oxides can significantly enhance their adsorption capacity and selectivity. For this reason, in this research, alumina is added to the aerogels to improve both mechanical and adsorption properties (due to the basic character of alumina). Furthermore, functionalizing alumina-silica aerogels with amino groups could improve their ability to adsorb CO_2. Alumina-silica aerogels functionalised with amino groups (AlSi with (3-aminopropyl) trimetossisilano, also called APTES) for CO_2 capture are here synthesized for the first time by a one-pot process. Various samples of AlSi-APTES were prepared by varying the number of APTES moles added during the synthesis: 2.5 mmol, 7.5 mmol, and 22.5 mmol (moles of APTES relative to 30 mmol of silica). Characterization results show that the increase in APTES content leads to an increase in the number of amino groups present in the aerogel. The analyses demonstrate that the incorporation of amino groups significantly changes the properties of the alumina-silica aerogels, reducing both the surface area and pore volume. Regarding CO_2 adsorption, no significant differences are observed between the samples with 2.5 and 7.5 mmol of APTES, suggesting that low functionalization does not confer a significant advantage in this molar range. An interesting result is obtained with the sample with the highest amine content (22.5 mmol of APTES) where the absorption of CO_2 far exceeds other samples demonstrating that with enough APTES, it is possible to absorb significant quantities of CO_2. It is worth noting that at low CO_2 partial pressures, even samples with a lower amine content are advantageous with respect to the non-functionalized sample as they absorb more CO_2 than the reference sample.

TABLE OF CONTENTS

FIGURE LIST **9**

TABLE LIST **12**

ABBREVIATIONS **13**

UNITS OF MEASUREMENT **15**

Introduction **17**

Silica aerogels **19**

1.1 Introduction 19

1.2 Characteristics, physical properties, and some related applications 20

1.3 Alumina-silica aerogels 22

1.4 Amine-modified silica aerogels 24

1.5 Alumina-silica aerogels functionalised with amino groups 26

Materials and methods **28**

2.1 Chemicals 28

2.2 Preparation 28

2.2.1 Gel synthesis: Sol-Gel process 28

2.2.2 Supercritical drying process 29

2.3 Characterization 31

2.3.1 FTIR 31

2.3.2 TGA 32

2.3.3 X-ray diffraction 32

2.3.4 N_2 adsorption 33

2.3.5 XPS 34

2.4 CO_2 adsorption - volumetric 34

2.5 CO_2 adsorption – in situ FTIR 35

Alumina-silica aerogels **36**

3.1 Introduction 36

3.2 Preparation of AlSi aerogel 36

3.2.1 Gel synthesis 36

3.2.2 Supercritical drying process 38

3.3 Characterization 41

3.3.1 FTIR 41

3.3.2 TGA 42

3.3.3 X-ray diffraction 43

3.3.4 N_2 adsorption 45

3.3.5 XPS ... 46
3.4 Preparation of AlSi_H_2O_prima ... 50
3.4.1 Gel synthesis ... 50
3.4.2 Supercritical drying process ... 52
3.5 Characterisation of AlSi_H_2O_prima ... 53
3.5.1 FTIR ... 53
3.5.2 TGA ... 53
3.6 Preparation of AlSi_H_2O_prima2 ... 54
3.6.1 Gel synthesis ... 54
3.6.2 Supercritical drying process ... 55
3.7 Characterisation of AlSi_H_2O_prima2 ... 57
3.7.1 FTIR ... 57
3.7.2 TGA ... 58
Alumina-silica aerogels functionalized with amino groups ... 60
4.1 Introduction ... 60
4.2 Preparation of AlSi – APTES ... 61
4.2.1 Gel synthesis ... 61
4.3 Preparation of AlSi – APTES (2.5 mmol) ... 63
4.3.1 Gel synthesis ... 63
4.3.2 Supercritical drying process ... 65
4.3.3 Reproduction ... 67
4.4 Characterization of AlSi – APTES (2.5 mol) ... 69
4.4.1 FTIR ... 69
4.4.2 TGA ... 70
4.4.3 X–ray diffraction ... 72
4.4.4 N_2 adsorption ... 73
4.4.5 XPS ... 80
4.5 Preparation of AlSi – APTES (7.5 mmol) ... 83
4.5.1 Gel synthesis ... 83
4.5.2 Supercritical drying ... 84
4.5.3 Reproduction ... 85
4.6 Characterization of AlSi – APTES (7.5 mmol) ... 87
4.6.1 FTIR ... 87
4.6.2 TGA ... 88
4.6.3 X–ray diffraction ... 90
4.6.4 N_2 adsorption ... 91

4.6.5 XPS ... 95
4.7 Preparation of AlSi – APTES (22.5 mmol) ... 99
4.7.1 Gel synthesis ... 99
4.7.2 Supercritical drying process ... 100
4.8 Characterisation of AlSi – APTES (22.5 mmol) ... 101
4.8.1 FTIR ... 101
4.8.2 TGA ... 102
4.8.3 N_2 Adsorption ... 103
4.8.4 XPS ... 105
CO_2 adsorption performance ... 109
5.1 Volumetric tests ... 109
5.1.1 Silica – alumina aerogels ... 109
5.1.2 AlSi – APTES (2.5 mmol, 7.5 mmol, and 22.5 mmol) ... 110
5.2 In-situ IR measurements ... 113
5.2.1 Interaction with CO_2 ... 113
Conclusion ... 116

FIGURE LIST

Figure 1: Atmospheric concentration of carbon dioxide from 1960 up to now [1]..... 17
Figure 2: Sol-gel process to produce aerogels [5]...... 19
Figure 3: Structure of silica aerogels [5]...... 20
Figure 4: Tetramethyl orthosilicate (TMOS). 23
Figure 5: Aluminium-tri-sec-butoxide. 23
Figure 6: Main steps and reactions involved in the formation of ASAs [12]. 23
Figure 7: Amine groups as scrubber of the carbon dioxide [15] 25
Figure 8: Sol-gel procedure to form alumina-silica aerogels [13] 26
Figure 9: A depiction of the phase diagram of a pure compound along with an examination of the various pathways associated with each aerogel drying method [2]..... 30
Figure 10: Scheme of the system for the supercritical drying with Carbon Dioxide. 31
Figure 11: The sample covered with ethanol...... 38
Figure 12: Samples of gels after being covered for a week with ethanol...... 38
Figure 13: Al - Si aerogel in autoclave. 39
Figure 14: Autoclave. 39
Figure 15: Samples after supercritical drying...... 40
Figure 16: Focus on the volume shrinkage...... 40
Figure 17: FTIR of Al-Si aerogel...... 42
Figure 18: Residual mass % vs Temperature of Al-Si aerogel...... 43
Figure 19: XRD Al-Si aerogel at high angles. 44
Figure 20: XRD Al-Si aerogel at low angles. 44
Figure 21: BET curve of Al-Si aerogel...... 45
Figure 22: BJH curve of Al-Si aerogel...... 46
Figure 23: Survey of AlSi sample. 47
Figure 24: high-resolution spectra of C in AlSi sample. 47
Figure 25: high-resolution spectra of O in AlSi sample...... 48
Figure 26: high-resolution spectra of N in AlSi sample...... 49
Figure 27: high-resolution spectra of Al in AlSi sample...... 50
Figure 28: Samples of AlSi_H_2O_prima. 51
Figure 29: Sample of AlSi_H_2O_prima after the supercritical drying process..... 52
Figure 30: FTIR of AlSi_H2O_prima aerogels. 53
Figure 31: TGA of AlSi_H2O_prima. 54
Figure 32: Gel of AlSi_H_2O_prima2...... 55
Figure 33: Aerogels of the AlSi_H_2O_prima2. 56
Figure 34: Aerogels of the AlSi_H_2O_prima2 without glass cylinders. 56
Figure 35: FTIR of AlSi_H_2O_prima2...... 58
Figure 36: TGA of AlSi_H_2O_prima2. 59
Figure 37: APTES molecule. 60
Figure 38: Al – Si – APTES aerogel after rapid gelation...... 63
Figure 39: Al – Si – APTES aerogel after rapid gelation (focus on the structure)...... 63
Figure 40: AlSi – APTES (2.5 mmol) aerogel of the second attempt. 65
Figure 41: Focus on the volume shrinkage...... 65
Figure 42: Samples after the supercritical drying. 66
Figure 43: Gel of AlSi-APTES (2.5 mmol)_R. 67
Figure 44: AlSi - APTES (2.5 mmol)_R aerogels...... 68
Figure 45: FTIR of AlSi – APTES (2.5 mmol) aerogel...... 69
Figure 46: FTIR for AlSi - APTES (2.5 mmol) aerogels (reproduction)..... 70

Figure 47: TGA of AlSi - APTES (2.5 mmol) aerogel. 71
Figure 48: TGA for AlSi - APTES (2.5 mmol)_R aerogels. 71
Figure 49: XRD at high angles of AlSi - APTES (2.5 mmol) aerogel. 72
Figure 50: XRD at low angles of AlSi - APTES (2.5 mmol) aerogels. 73
Figure 51: BET of AlSi - APTES (2.5 mmol) aerogel. 74
Figure 52: BJH of AlSi - APTES (2.5 mmol) aerogel. 74
Figure 53: BET of AlSi-APTES (2.5 mmol)_R aerogels. 75
Figure 54: BJH of AlSi-APTES (2.5 mmol)_R aerogels. 76
Figure 55: BET of xerogel AlSi+APTES (2.5 mmol) 77
Figure 56: BJH of xerogel AlSi+APTES (2.5 mmol) 78
Figure 57: BET of AlSi-APTES (2.5 mmol)_R xerogels. 79
Figure 58: BJH of AlSi-APTES (2.5 mmol)_R xerogels. 79
Figure 59: Survey spectrum of AlSi+APTES (2.5 mmol) sample* 80
Figure 60: high-resolution spectra of C in AlSi+APTES (2.5 mmol) sample* 81
Figure 61: high-resolution spectra of O in AlSi+APTES (2.5 mmol) sample* 81
Figure 62: high-resolution spectra of N in AlSi+APTES (2.5 mmol) sample* 82
Figure 63: high-resolution spectra of Al in AlSi+APTES (2.5 mmol) sample* 83
Figure 64: Gel of AlSi - APTES (7.5 mmol) 84
Figure 65: Samples of AlSi - APTES (7.5 mmol) aerogel. 85
Figure 66: Supercritical drying of AlSi - APTES (7.5 mmol)_R aerogels. 86
Figure 67: FTIR of AlSi - APTES (7.5 mmol) aerogel. 88
Figure 68: FTIR of AlSi - APTES (7.5 mmol)_R aerogels. 88
Figure 69: TGA of AlSi - APTES (7.5 mmol) aerogel. 89
Figure 70: TGA of AlSi - APTES (7.5 mmol)_R aerogels. 90
Figure 71: XRD at high angles of AlSi - APTES (7.5 mmol) aerogels. 90
Figure 72: XRD at low angles of AlSi - APTES (7.5 mmol) aerogels. 91
Figure 73: BET of AlSi - APTES (7.5 mmol) aerogel. 91
Figure 74: BJH of AlSi - APTES (7.5 mmol) aerogel. 92
Figure 75: BET of AlSi - APTES (7.5 mmol)_R aerogels. 93
Figure 76: BJH of AlSi - APTES (7.5 mmol)_R aerogels. 93
Figure 77: BET of AlSi+APTES (7.5 mmol) 94
Figure 78: BJH of AlSi+APTES (7.5 mmol) 95
Figure 79: Survey of AlSi+APTES (7.5 mmol) sample*. 96
Figure 80: high-resolution spectra of C in AlSi+APTES (7.5 mmol) sample*. 96
Figure 81: high-resolution spectra of O in AlSi+APTES (7.5 mmol) sample*. 97
Figure 82: high-resolution spectra of N in AlSi+APTES (7.5 mmol) sample*. 98
Figure 83: high-resolution spectra of Al in AlSi+APTES (7.5 mmol) sample*. 98
Figure 84: Supercritical drying of the AlSi - APTES (22.5 mmol) aerogels. 100
Figure 85: FTIR of AlSi-APTES (22.5 mmol) aerogels. 102
Figure 86: TGA of AlSi-APTES (22.5 mmol) aerogels. 103
Figure 87: BET of AlSi-APTES (22.5 mmol) aerogels. 104
Figure 88: BJH of AlSi-APTES (22.5 mmol) aerogels. 104
Figure 89: Survey of AlSi+APTES (22.5 mmol) sample*. 105
Figure 90: high-resolution spectra of C in AlSi+APTES (22.5 mmol) sample*. 106
Figure 91: high-resolution spectra of O in AlSi+APTES (22.5 mmol) sample*. 106
Figure 92: high-resolution spectra of N in AlSi+APTES (22.5 mmol) sample*. 107
Figure 93: high-resolution spectra of Al in AlSi+APTES (22.5 mmol) sample*. 108
Figure 94: Run1 and Run2 of silica alumina aerogels. 109

Figure 95: Run1 and Run2 of AlSi+APTES (2.5 mmol) sample. 110
Figure 96: Run1 and Run2 of AlSi+APTES (7.5 mmol) sample. 111
Figure 97: Run1 and Run2 of the AlSi-APTES (22.5 mmol) sample. 111
Figure 98: Comparison between Run1 of AlSi_APTES (2.5 mmol), AlSi_APTES (7.5 mmol), AlSi_APTES (22.5 mmol) and AlSi. 112
Figure 99: FTIR analysis and differences for the AlSi and CO_2 system at increasing equilibrium pressures. 114
Figure 100: FTIR analysis and differences for the AlSi – APTES (2.5 mmol) and CO_2 system at increasing equilibrium pressures. 114
Figure 101: FTIR analysis and differences for the AlSi – APTES (7.5 mmol) and CO_2 system at increasing equilibrium pressures. 115

TABLE LIST

Table 1: An example of the unusual properties of silica aerogels [5] 21
Table 2: Overview of the different methods developed to obtain AMSAs. 25
Table 3: Details of the reactants involved in the sol-gel process. 28
Table 4: Molar ratio between reagents of AlSi 36
Table 5: Theoretical mass quantity of reagents 37
Table 6: Dimensions, density, and volume shrinkage of Al-Si aerogel samples 41
Table 7: Summary of the textural properties of Al-Si aerogels 46
Table 8: Mass quantities of reagents of solution A 50
Table 9: Mass quantities of reagents of solution B 51
Table 10: Dimensions, density, and volume shrinkage of AlSi_H_2O_prima aerogel 52
Table 11: Mass quantities of the reagents of Solution A 54
Table 12: Mass quantities of the reagents of the solution B 54
Table 13: Dimensions, density, and volume shrinkage of AlSi_H2O_prima2 aerogels: 57
Table 14: Mass quantities for the reagents in the solution A 61
Table 15: Mass quantities for the reagents in the solution B 61
Table 16: Molar ratio between reagents of AlSi - APTES 62
Table 17: Mass quantities of the reagents of solution A 63
Table 18: Mass quantities of the reagents of the solution B 63
Table 19: Molar ratio between reagents of AlSi - APTES (2.5 mmol) 64
Table 20: Dimensions, density, and volume shrinkage of AlSi - APTES (2.5 mmol) aerogel 66
Table 21: Mass quantities of the reagents of solution A 67
Table 22: Mass quantities of the reagents of solution B 67
Table 23: Dimensions, density, and volume shrinkage of AlSi - APTES (2.5 mmol)_R aerogel. 68
Table 24: Summary of the textural properties of the AlSi - APTES (2.5 mmol) aerogels 75
Table 25: Textural properties of AlSi-APTES (2.5 mmol)_R aerogels. 76
Table 26: Summary of the textural properties of the AlSi - APTES (2.5 mmol) xerogels 78
Table 27: Textural properties of AlSi-APTES (2.5 mmol)_R xerogels. 80
Table 28: Mass quantities of the reagents of the solution A 83
Table 29: Mass reagents of the solution B 83
Table 30: Molar ratio of reagents of AlSi - APTES (7.5 mmol) 84
Table 31: Dimensions, density, and volume shrinkage of AlSi - APTES (7.5 mmol) aerogel 85
Table 32: Mass quantities of the reagents of the solution A 86
Table 33: Mass quantities of the reagents of the solution B 86
Table 34: Dimensions, density, and volume shrinkage of the AlSi - APTES (7.5 mmol)_R aerogel 87
Table 35: Summary of the textural properties of AlSi - APTES (7.5 mmol) aerogels 92
Table 36: Mass quantities of the reagents of the solution A 99
Table 37: Mass quantities of the reagents of the solution B 99
Table 38: Molar ratio of reagents of AlSi - APTES (22.5 mmol) 100
Table 39: Dimensions, density, and volume shrinkage of the production of AlSi - APTES (22.5 mmol) aerogel 101
Table 40: Textural properties of AlSi-APTES (22.5 mmol) aerogels. 105

ABBREVIATIONS

GHGs	greenhouse gas
CO_2	carbon dioxide
CCS	carbon capture and storage
Al_2O_3	alumina
$-NH_2$	ammino groups
SiO_2	silica
ASA	alumina-silica-based aerogels
MEMS	microelectromechanical systems
AMSA	amine-modified silica aerogels
SCD	supercritical drying
TEOS	tetraethyl orthosilicate
TMOS	tetramethyl orthosilicate
ATSB	aluminium-tri-sec-butoxide
$AlCl_3$	aluminium chloride
AMSA	amine-modified silica aerogel
APTES	3-(Aminopropyl) triethoxysilane
RLCA	reaction-limited cluster-cluster aggregation
RLMC	reaction limited monomer cluster growth
EtOH	ethanol
FESEM	field emission scanning electron microscopy
XPS	X-ray Photoelectron Spectroscopy
FTIR	Fourier Transform Infrared
XRD	X-Ray Diffraction

MOF	metal-organic framework
BET	Brunauer–Emmett–Teller
BJH	Barrett-Joyner-Halenda

UNITS OF MEASUREMENT

bar	bar
Pa	Pascal
°C	degree Celsius
cm^2	square centimetre
g	gram
h	hour
kg	kilogram
kJ	kilojoule
kW	kilowatt
kWh	kilowatt hour
m	meter
MJ	megajoule
mol	mol
MPa	megapascal
Nm^3	normal cubic meter
sec	second
V	volt

Introduction

Global climate change, predominantly characterized by the phenomenon of global warming, stands as one of the most formidable challenges confronting human society in the 21st century. Over the past century, the global average temperature has witnessed an increase of approximately 0.74 °C (with a range of 0.56 – 0.92 °C). Temperature elevations have been more pronounced on terrestrial surfaces than on oceanic surfaces. The escalating concentration of greenhouse gases (GHGs) attributed to human activities such as fossil fuel combustion and deforestation is identified as a key driver of the global temperature rise. This substantial warming trend triggers a cascade of adverse consequences for natural systems, including the melting of snow and ice, rising sea levels, and disruptions in the hydrological cycle [1].

Of all GHGs, carbon dioxide (CO_2), which constitutes approximately 60% of global GHG emissions, primarily arises from the combustion of fossil fuels and is acknowledged as the principal driver of global warming [1]. Given the far-reaching impacts of carbon emissions on both social and economic development, climate change has transcended its origins as a purely academic subject to become a pressing international concern with profound political, economic, and diplomatic implications (***Figure 1*** shows the increase in the atmospheric concentration of carbon dioxide).

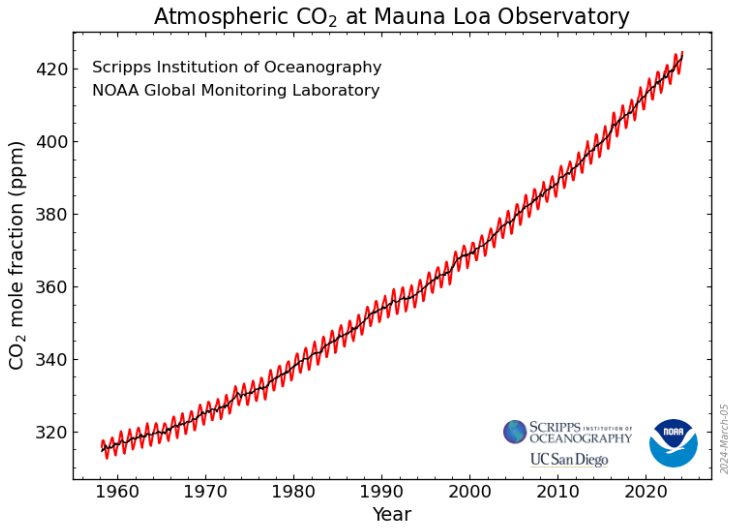

Figure 1: Atmospheric concentration of carbon dioxide from 1960 up to now [1].

To mitigate the adverse effects of CO_2 emissions, there is an urgent need for innovative and efficient technologies for carbon capture and storage (CCS). Given the urgent societal and environmental imperatives, CO_2 capture technology must be both economically viable and scalable.

There are three primary methods for CO_2 capture: pre-combustion, post-combustion, and oxycombustion. These methods entail various processes for separating CO_2 from gas mixtures, including absorption, physical/chemical adsorption, membrane separation, and cryogenic separation. However, challenges exist with these technologies, including their high energy consumption, corrosion risks to equipment, degradation of aqueous amines used in liquid phase absorption, potential generation of toxic by-products, and excessive solvent loss through evaporation [2].

To address these challenges, recent advancements in CO_2 capture technology focus on solid physical and chemical adsorbents, such as zeolites, metal-organic frameworks (MOFs), activated carbon, mesoporous silica, aerogels, mesoporous alumina, metal oxides, covalent organic polymers, and amine-based materials. These emerging technologies offer promising solutions to overcome the drawbacks associated with traditional CO_2 capture methods [2].

Among these mentioned methods, the adsorptive separation using organic functionalized porous materials is often considered the most straightforward and effective approach for CO_2 capture. Therefore, significant attention has been directed toward the development of CO_2 adsorbents with high adsorption capacities and exceptional selectivity, to facilitate their practical implementation.

Silica aerogels have emerged as a remarkable class of materials with exceptional properties that make them highly attractive for CO_2 capture applications [3], [4], [5]. These materials exhibit an extraordinary combination of characteristics, including high surface area, low density, excellent thermal insulating properties, and tuneable porosity, making them ideal candidates for the development of next-generation adsorbents. Furthermore, by incorporating metal oxides as functional groups within the silica aerogel matrix, the adsorption capacity and selectivity can be significantly enhanced. It is important to underline that aerogels are already good adsorbents but their selectivity towards CO_2 can be improved by functionalizing the matrix [6].

In the above-cited context, the production of novel functionalized aerogels for CO_2 capture may represent a promising route to be investigated. For example, alumina (Al_2O_3) is a metal oxide that has gained attention as a potential functionalisation agent for silica aerogels due to its versatile surface chemistry and reactivity. It is also known that silica aerogels functionalised with amines are suitable for CO_2 capture and that alumina can present characteristics favourable to CO_2 capture (such as a basic character) [4]. This work aims to combine these two fronts to obtain alumina-silica aerogels functionalised with amines and test their effectiveness in CO_2 capture. This type of material has been synthesized for the first time as part of part of this research project and there are no precedents in the literature.

Chapter 1

Silica aerogels

1.1 Introduction

Aerogels have a relatively long history, with their inception dating back to 1931 when Steven Kistler, conducting research at the College of the Pacific in Stockton, California, developed the first aerogels. According to Kistler, the term "aerogel" indicates gels in which the liquid is replaced with a gas, without collapsing the gel solid network. This definition largely aligns with the actual understanding of aerogels. [7].

Aerogels exhibit diverse classifications depending on their visual presentation (including monoliths, powders, and films), their structural characteristics (microporous, mesoporous, or mixed porous), or by categorizing their composition (organic, inorganic, or hybrid) [2].

One of the most studied aerogels is the silica-based one. Silica aerogels (SiO_2) are extraordinary substances, and they represent a groundbreaking innovation in solid-state materials. They are known for their unique combination of properties, making them invaluable in a wide range of applications, from insulation to aerospace technology, and even as a medium for scientific research.

In general, aerogels are produced through a sol-gel process, in which nanoparticles suspended in a liquid solution (i.e., a sol) interconnect and form a continuous, porous, nanostructured network of particles across the volume of the liquid medium (i.e., a gel) [7], [8]. To obtain their characteristic properties, a specific drying procedure is essential, during which the liquid within the pores is replaced with air while preserving the solid framework. Supercritical drying (SCD) is the most employed method. This results in a porous silica framework containing only air (***Figure 2***).

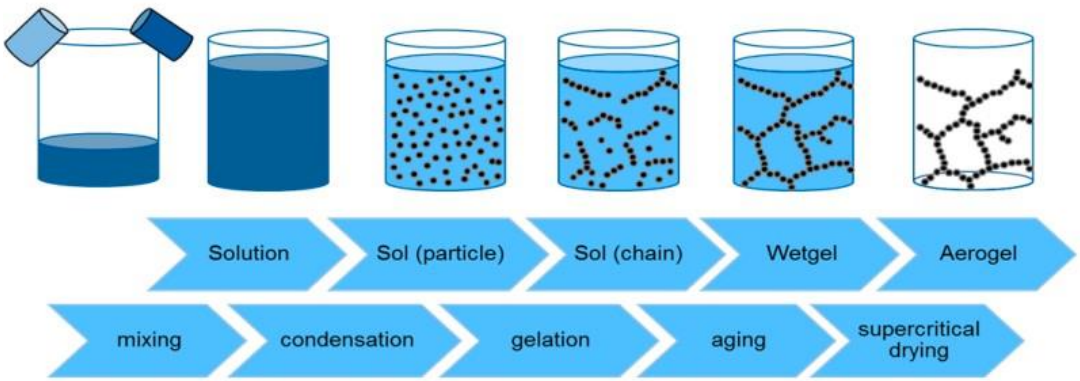

Figure 2: Sol-gel process to produce aerogels [5].

The drying process of the gel stands out as the most crucial stage in aerogel synthesis. It holds significant importance as it can directly impact the pore structure, including porosity and surface area, of the final product. This impact arises from the shrinkage induced by capillary pressure during drying [2].

A particular aspect that is worthy of analysis is the difference between aerogels and xerogels. Xerogels are similar porous materials formed by drying a gel and they also result in a solid structure with interconnected pores, akin to a sponge. With respect to aerogels, they are obtained through conventional drying methods, where the liquid solvent is evaporated or removed under atmospheric pressure, which cannot avoid a significant extent of collapse in their final porous structure. Consequently, aerogels exhibit higher specific surface areas, superior insulating properties and are lighter than xerogels[9].

1.2 Characteristics, physical properties, and some related applications

The solid structure of silica aerogel is comprised of silica nanoparticles, which are essentially the oxide of silicon. The specific way these nanoparticles bond together to form the aerogel's framework can vary and is primarily influenced by the chemical processes employed in the preparation of the aerogel precursor gel [7].

If silica aerogels are produced by low-temperature drying (CO_2), they typically possess an abundance of unreacted silanol (Si-OH) groups on the surface of their skeletal structure (with high-temperature drying there are no -OH groups and the matrix is hydrophobic). These silanol groups contribute to the high hydrophilicity of silica aerogels, meaning that they readily absorb water upon contact and can even draw in moisture from the surrounding atmosphere (***Figure 3***) [7].

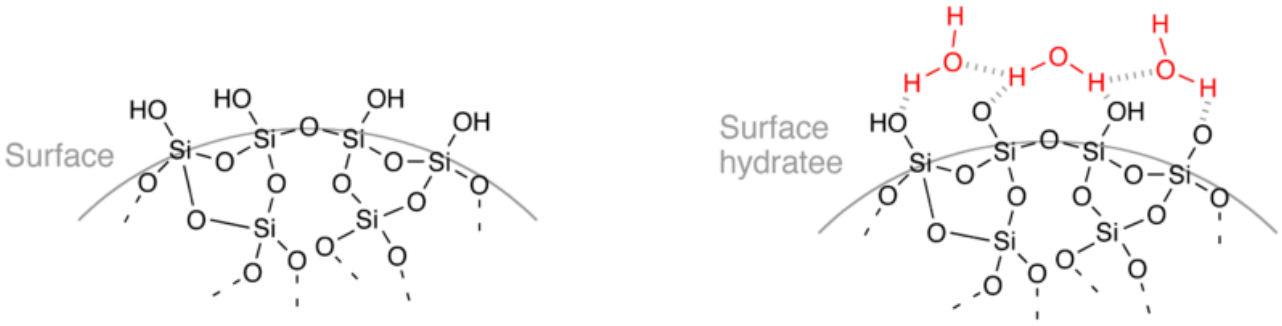

Figure 3: Structure of silica aerogels [5].

A silica aerogel of exceptional purity and quality will typically display remarkable transparency, often accompanied by a distinctive bluish tint. This bluish hue arises from the phenomenon known as Rayleigh scattering, where the shorter wavelengths of light interact with the nanoparticles forming the aerogel's structural framework. When touched, a high-quality silica aerogel

may have a slightly adhesive or sticky feel, with the specific tactile sensation varying depending on the aerogel's density [7].

Silica aerogels have an amorphous nature. Typically, they exhibit a prominent mesoporous structure with interconnected pore sizes falling within the range of 5 to 100 nm. The average pore diameter typically falls between 20 and 40 nm. As a result of this intricate pore structure, silica aerogels are associated with a notably high specific surface area, which makes them excellent candidates for various applications in catalysis, adsorption, and filtration. Their large surface area allows for enhanced chemical reactivity, which is exploited in catalytic processes, while their porous structure can be used to adsorb and separate molecules and particles from gases and liquids. An example of these unusual properties is shown in ***Table 1*** [5].

Table 1: An example of the unusual properties of silica aerogels [5]

Specific surface area	500 – 1200 m^2/g
Porosity	80 – 99.8 %
Density	0.003 – 0.35 g/cm^3
Thermal insulation value	0.005 W/m K
Dielectric constant (k)	1.0 – 2.0
Index of refraction	~1.05

One of the prominent attributes of silica aerogels lies in their remarkably low thermal conductivity, establishing them as among the most renowned thermal insulating materials. Additionally, these aerogels can be engineered to achieve optical transparency, although they are inherently fragile. This intriguing combination of properties opens exciting possibilities for both opaque and transparent insulating components, as well as daylighting devices, provided they can be reinforced to enhance their mechanical stability [10].

The optical characteristics of silica aerogels, particularly their transparency and scattering properties, constitute another significant set of features. These attributes often come into play in conjunction with their thermal properties, especially when aiming for transparent thermal insulation solutions, such as in window applications. The acoustic properties of silica aerogels are intimately linked to their thermal insulation capabilities. The transmission of sound through aerogels depends on various factors, including the nature and pressure of the interstitial gas, the aerogel's density, and its overall texture. In this regard, silica aerogels excel as acoustic insulators [10], [11].

Another significant category of characteristics pertains to the mechanical properties of silica aerogels. These materials exhibit notably low compressive strength, tensile strength, and elastic modulus, with these properties heavily dependent on the connectivity of the aerogel network and its density.

1.3 Alumina-silica aerogels

Aerogels can be derived from a single precursor (referred to as pure aerogels) or a combination of precursors from various sources (known as hybrid aerogels). A typical example is a class of aerogels where two or more elements are blended. For instance, combinations may involve elements like titanium, zirconium, or aluminium [8], [12]. This fusion leads to the obtainment of materials characterized by diverse properties, which can be customized to suit specific intended applications. Alumina-silica aerogel, also known as alumina-silica-based aerogel (ASA), is a fascinating hybrid aerogel that has garnered significant attention in the field of materials science.

Due to their crystalline and fibrous network microstructure, which remains stable even at elevated temperatures, alumina aerogels exhibit superior thermal stability compared to pure silica ones. Additionally, alumina aerogels demonstrate also higher mechanical properties. However, pure Al_2O_3 aerogels are, in general, characterized by lower surface areas compared to pure silica ones and their bulk density is not as low as that of silica's. The subclass of alumina-silica aerogels combines the unique characteristics of both silica and alumina, allowing the synthesis of a high-surface-area material resistant to high temperatures and with improved mechanical properties [12].

The synthesis of alumina-silica aerogels is a multistep process involving precise control over precursor selection, sol-gel chemistry, and supercritical drying conditions. Typically, the synthesis of aerogel composites of this nature follows a two-step acid-base sol-gel procedure.

Alumina and silica sols are separately prepared, with a solvent (mostly ethanol), and in the presence of HCl and NH_4OH acting as the prevalent acid and alkaline catalysts, respectively. The necessity for distinct sol preparations arises from the heightened reactivity of aluminium alkoxides in water compared to alkoxysilanes, owing to their lower electronegativity and greater Lewis's acidity. The accelerated hydrolysis of aluminium alkoxides can result in alumina precipitation before its binding to hydrolysed silica precursors, potentially causing phase segregation [8].

Silicon alkoxides such as tetraethyl orthosilicate ($Si(OC_2H_5)_4$) and tetramethyl orthosilicate ($Si(OCH_3)_4$) are commonly chosen as silica precursors for ASAs (***Figure 4***).

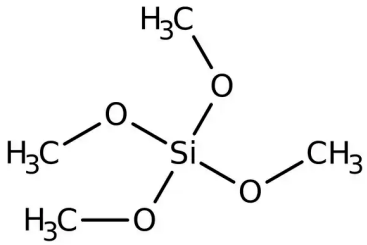

Figure 4: Tetramethyl orthosilicate (TMOS).

As far as alumina precursors are concerned, various synthetic compounds have been employed, with aluminium-tri-sec-butoxide ($Al[OCH(CH_3)C_2H_5]_3$) and aluminium chloride ($AlCl_3$) being the most frequently used (***Figure 5***).

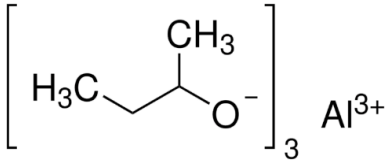

Figure 5: Aluminium-tri-sec-butoxide.

These precursors are dissolved in a suitable solvent, often ethanol or a combination of ethanol and water, to form a sol. The two formed sols are combined and undergo polycondensation reactions, so leading to the formation of a wet gel with a three-dimensional network structure. The gel is then subjected to supercritical drying to form an aerogel (***Figure 6***). The prevalent method employed for alumina-silica aerogels involves high-temperature ethanol supercritical drying (C_2H_6O). However, alternative drying techniques, such as methanol, carbon dioxide, and acetone supercritical drying, as well as ambient pressure drying, have also been explored [8].

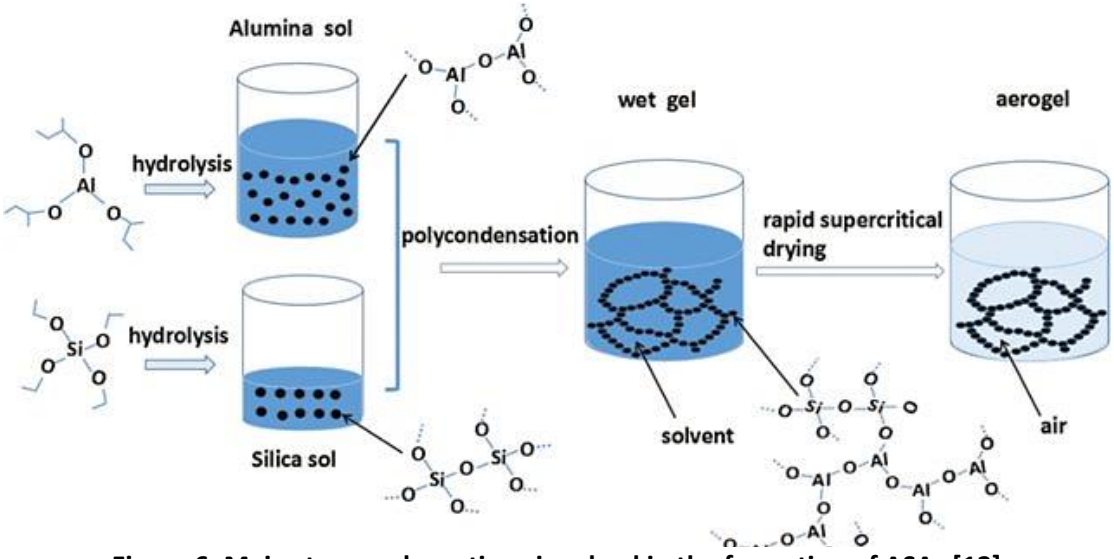

Figure 6: Main steps and reactions involved in the formation of ASAs [12].

ASAs have found a multitude of potential applications, particularly in scenarios where high-temperature environments are involved. ASA materials have demonstrated their suitability in various domains, including catalysis, thermal protection/insulation systems, and environmental applications as adsorbents [8].

1.4 Amine-modified silica aerogels

Amine-modified silica aerogels (AMSAs) represent a fascinating and highly versatile class of aerogels. These aerogels are derived from traditional silica aerogels through a process of functionalization, where amine groups are introduced into the aerogel's porous structure. This modification imparts unique properties to the material, making it particularly valuable as an adsorbent for CO_2 capture [13].

When silica aerogels are characterized by an appropriate pore structure and a significant specific surface area, they exhibit substantial physical adsorption capabilities. However, owing to the inherent inertness of the surface Si-OH groups on silica aerogels, the capacity for CO_2 adsorption through physical adsorption alone is severely limited. Recent studies have demonstrated that the introduction of amino groups into silica aerogels serves as an effective method for enhancing their CO_2 capture capacity [13]. The inherent basic properties of amines play a pivotal role in facilitating the absorption of a significant amount of CO_2. Notably, these interactions are reversible, enabling the capture and subsequent release of CO_2, a critical aspect of the process (***Figure 7***). Although the specific reaction mechanisms may vary, they fundamentally involve equilibrium reactions leading to the formation of carbamates and bicarbonates [14]. Carbamates result from the interaction of primary amines such as R_1NH_2 and secondary amines like R_1R_2NH with CO_2 in the absence of water. Bicarbonates, on the other hand, are generated under conditions involving water or a substantial partial pressure of CO_2 through the hydrolysis of carbamates. This reaction additionally yields a fresh supply of amine, ready to engage once more in CO_2 capture. These chemical interactions not only enhance the CO_2 adsorption capacity of silica aerogels but also address the limitations of poor physical adsorption selectivity and slow adsorption rates [4], [6], [15].

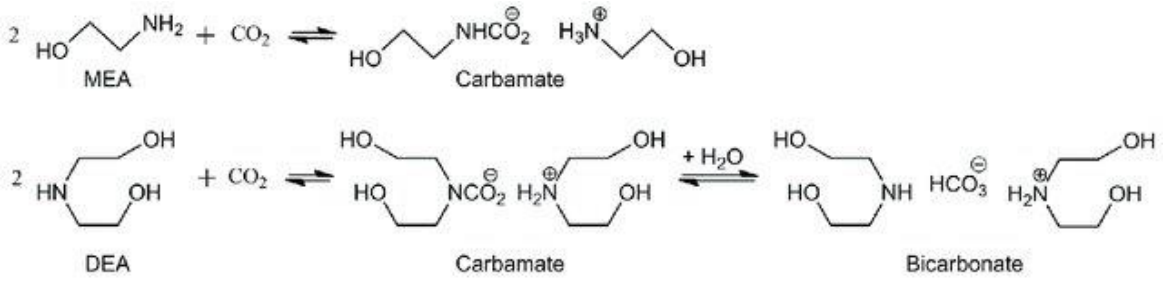

Figure 7: Amine groups as scrubber of the carbon dioxide [15]

In the realm of CCS applications, amines must embody specific physical and chemical characteristics to effectively facilitate CO_2 capture. Firstly, they need to exhibit solubility in water or other compatible liquids without forming stable compounds with the acid gas, ensuring optimal interaction with CO_2. Maintaining a high boiling temperature, ideally not lower than 100°C, is crucial to prevent excessive volatility and ensure stability under varying operational conditions, including the selective gas elimination temperature. Furthermore, amines should possess high molecular weight and robust intermolecular interactions to bolster their efficacy in capturing CO_2. Low viscosity is also essential, promoting faster diffusion kinetics for efficient CO_2 absorption. Additionally, a higher pKa value signifies a greater basicity of the amine, which enhances its capacity for CO_2 absorption. These combined attributes make amines well-suited for their role in carbon capture applications [16].

Different methods have been developed to obtain AMSAs. ***Table 2*** represents a summary of the common processes present in literature to obtain this type of aerogel [6].

Table 2: Overview of the different methods developed to obtain AMSAs.

METHOD	DESCRIPTION
Traditional two-phase method [17], [18], [19], [20]	Amine-modified silica aerogel can be prepared by soaking wet silica gel in a solution of 3-(Aminopropyl) triethoxysilane (APTES) and ethanol. APTES diffuses into the gel through capillary force and subsequently grafts onto the gel surface via a condensation reaction with Si–OH groups. However, a low CO_2 adsorption capacity was noted, indicating that the grafted amines could compromise the textural properties of the aerogel.
Model of the anionic surfactant [20], [21]	According to the anionic surfactant model, amines are directly incorporated into the

	surfactant-mediated amine matrix. However, the introduced surfactant is difficult to remove from pure silica, potentially damaging the pores during the drying process.

To overcome the above-mentioned limitations, an innovative and simple co-precursor sol-gel procedure has been developed (***Figure 8***) [6], [22], [23], [24]. First, APTES, the amine-containing precursor, is hydrolysed and mixed with TEOS silica precursor to produce silica sol. After the sol is prepared, it undergoes gelation to form a three-dimensional network structure. This gel is then subjected to supercritical drying. The resulting amine-modified silica aerogel boasts a high surface area, low density, and tuneable surface chemistry due to the presence of amine groups. The specific properties of the amine-modified silica aerogel can be fine-tuned by adjusting the concentration of the amine precursor, the sol-gel parameters, and the supercritical drying conditions [6].

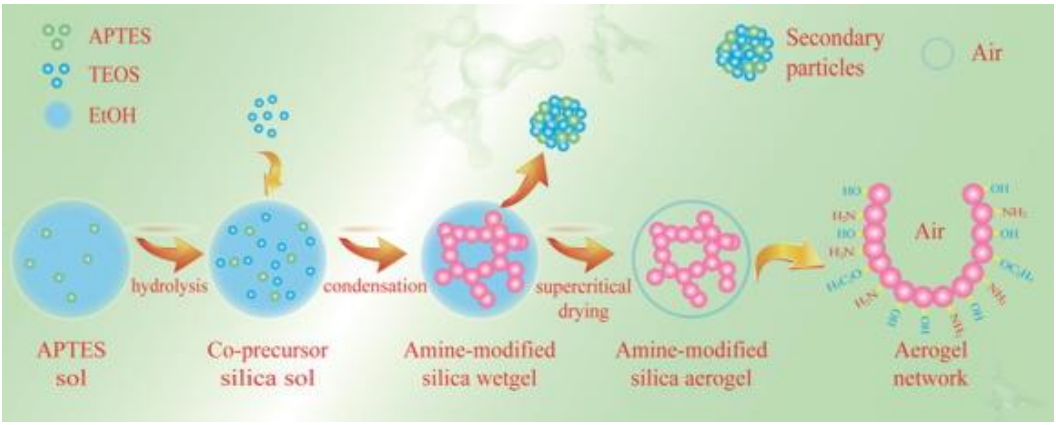

Figure 8: Sol-gel procedure to form alumina-silica aerogels [13]

In the case of amine-modified aerogels, amine groups are either chemically grafted to the aerogel's surface through strong covalent bonds or introduced into the pore structure via weak physical molecular forces. However, there is a potential risk of pore collapse and disruption of the aerogel's structure, which can impact its adsorption capacity. This issue is particularly significant when applying or regenerating amine-modified silica aerogels (AMSA), especially in the presence of moisture. Therefore, it is fundamental to explore methods that can facilitate the preparation of AMSA with a stable structure and consistent properties. One way to prepare a more resistant structure is by using alumina[13].

1.5 Alumina-silica aerogels functionalised with amino groups

With the idea of obtaining materials for CO_2 capture, it may be advantageous to combine the properties of silica aerogels, alumina, and amines, but there are no examples in the literature. The

scope of the thesis, then, is to synthesise, for the first time, this new type of aerogels by introducing amine functional groups into the porous structure of alumina-silica aerogels. In particular, the introduction of the amines is proposed through a one-pot process, which therefore avoids the need for a further step (and additional time) for functionalization.

One of the key features of this type of aerogel is its high surface area and well-defined pore structure. This structural advantage is a result of the silica aerogel's low density and nanometre-sized pores, which provide an enormous internal surface area. The presence of alumina allows it to have high thermal stability, good mechanical properties, and basic character. The large surface area, coupled with the amine functionalization, enables these aerogels to exhibit remarkable adsorption capabilities. They can potentially capture a wide range of substances, including heavy metals, organic compounds, and gases, making them invaluable in environmental remediation, water purification, and air quality control. In the following chapters, the tests carried out to obtain the non-functionalised alumina-silica aerogels as well as those functionalized with the amino groups are presented.

Chapter 2

Materials and methods

2.1 Chemicals

The following materials were used for the synthesis:

Table 3: Details of the reactants involved in the sol-gel process.

Reactant	Chemical formula	MM (g/mol)	Purity (%)	Productor
ATSB	$Al[OCH(CH_3)C_2H_5]_3$	152.25	97	ThermoScientific
TMOS	$Si(OCH_3)_4$	246.32	≥ 98	Fluka
Hydrochloric acid	HCl	36.46	37	Sigma-Aldrich
2 – butanol	$C_4H_{10}O$	74.12	/	Emplura (SUPELCO)
Ammonium hydroxide	NH_4OH	35.04	30.33	Sigma-Aldrich
Water	H_2O	18.01	/	MERK (Lichrosolu for chromatography)
Ethanol	C_2H_6O	46.07	ACS-Reag.	Carlo Erba
APTES	$C_9H_{23}NO_3Si$	221.372	99	Sigma-Aldrich

2.2 Preparation

2.2.1 Gel synthesis: Sol-Gel process

The sol-gel process is a versatile and widely utilized method to produce aerogels, providing a unique route to engineer materials with exceptional porosity and tailored properties. The process typically initiates with the formation of a stable colloidal suspension of nanoparticles in a liquid medium (sol). This sol undergoes controlled gelation, transitioning into a three-dimensional network known as a gel. The gel is then subjected to supercritical drying to remove the liquid component, leaving behind an aerogel with an intricate nanoporous structure. This method allows for precise control over the aerogel's composition, pore size distribution, and surface area. The sol-gel process has proven especially valuable in synthesising aerogels from various precursors, including silica,

metal oxides, and organic polymers, so enabling a broad range of functionalities from lightweight thermal insulators to efficient catalyst supports. The versatility and controllability inherent in the sol-gel synthesis procedure make it a pivotal technique for advancing the development and application of aerogels in diverse fields [6].

2.2.2 Supercritical drying process

Supercritical drying is a controlled process employed for the conversion of a contained liquid within a substance into a gas in the absence of surface tension and capillary stress[25], [26]. This procedure is widely employed as the predominant method for converting gels into aerogels.

When a liquid is extracted from a porous material, like a gel, through evaporation or boiling, the capillary stress within the pores of the material can lead to the collapse of the struts in the pore network, causing the material to shrink. This phenomenon, known as "capillary stress," intensifies as more molecules evaporate, especially when the liquid has high surface tension, enhancing molecular attraction and, consequently, the stress on the material's pores [25].

Since the start is from an alcohol gel, low-temperature drying requires an exchange of solvent (alcohol-liquid CO_2), a process that is not present in high-temperature drying where it is the alcohol that becomes supercritical. Supercritical drying of a gel involves elevating the temperature and pressure of the liquid contained in the material beyond its critical point, so transforming it into a supercritical fluid. As the liquid approaches its critical point, molecules move more freely, reducing their stickiness and decreasing surface tension. Consequently, the capillary stress exerted by the liquid diminishes. At the critical point, the supercritical fluid loses all surface tension, rendering it unable to exert capillary stress [25], [26].

At this point, the supercritical fluid can be expelled from the material's pores by depressurising the fluid while maintaining it above its critical temperature (isothermal depressurization). Eventually, when enough fluid is expelled, and when it is cooled below the critical point, there is an insufficient number of molecules to condense into a liquid. Instead, the fluid reverts into a gas (***Figure 9***) [25], [26].

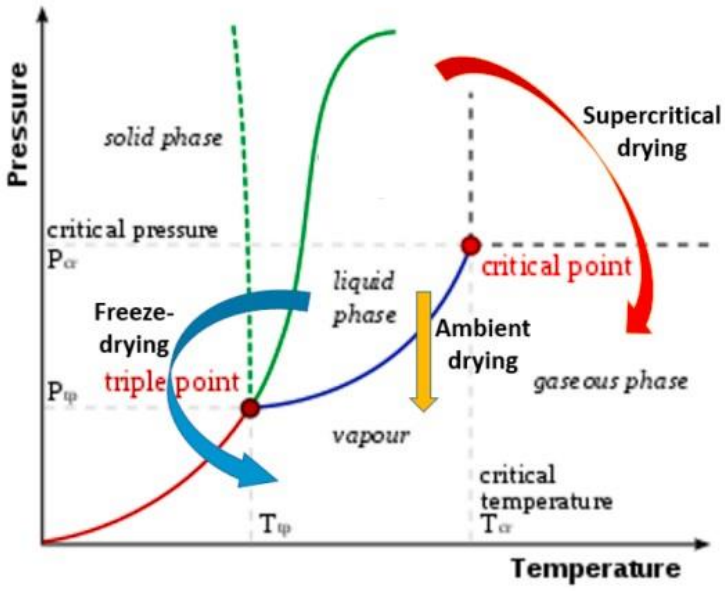

Figure 9: A depiction of the phase diagram of a pure compound along with an examination of the various pathways associated with each aerogel drying method [2].

Supercritical drying can be conducted at low or high temperatures. The aerogels obtained with solvents at high temperatures have different characteristics from those obtained at low temperatures. For example, a silica aerogel dried with supercritical CO_2 (i.e. at low temperature) is hydrophilic, while it is hydrophobic when dried with supercritical methanol (i.e. at high temperature). Fluids suitable for supercritical drying at low temperatures encompass carbon dioxide (whose critical point is at 304.25 K and 7.39 MPa) and freon (whose critical point is approximately 300 K at 3.5–4 MPa) [25].

Figure *10* represents a scheme of the supercritical drying system that uses carbon dioxide (CO_2) as the working fluid. The system operates as follows: the CO_2 is stored in a pressurized cylinder. A pump moves the carbon dioxide from the cylinder through the system. The CO_2 then passes through a heater, which increases its temperature. A control valve (V1) regulates the flow of heated carbon dioxide into the impregnation vessel. This vessel is located inside a heating oven to maintain the desired temperature and pressure during the process. The heated CO_2 impregnates the material inside the vessel. Another control valve (V2) regulates the flow of impregnated carbon dioxide from the vessel to the outlet. The impregnated gas passes through a heated discharge valve before being released through a vent.

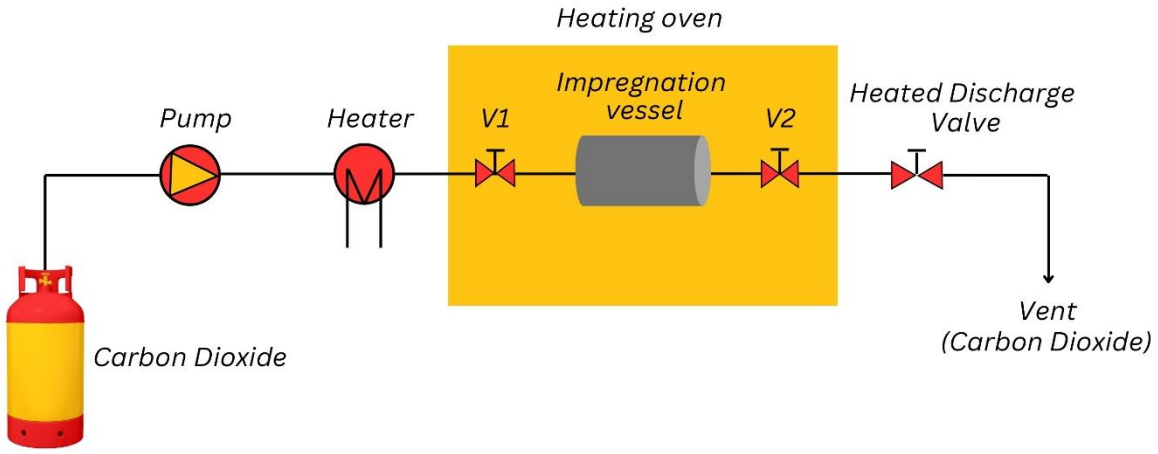

Figure 10: Scheme of the system for the supercritical drying with Carbon Dioxide.

As it has already been discussed, supercritical drying offers distinct advantages in aerogel production. The most notable benefit is the minimal shrinkage of pore structure, which is attributed to the inherent absence of surface tension within the gel's pores. This characteristic ensures the preservation of the high surface area and pore volumes, essential for various applications. However, the process entails prolonged solvent exchange, making it time-consuming. Moreover, its high cost limits its widespread application despite its efficacy in producing aerogels with superior structural properties [27], [28].

2.3 Characterization

2.3.1 FTIR

Fourier Transform Infrared (FTIR) analysis is a powerful technique employed in the characterization of materials since it provides valuable insights into their chemical composition. By measuring the absorption of infrared light at different wavelengths, FTIR spectroscopy allows the functional groups present in material matrices to be identified. As far as aerogels are concerned since they are often composed of intricate networks of inorganic and organic components, FTIR analysis helps elucidate the nature of bonds, such as O-H, C-H, and Si-O, offering a detailed molecular fingerprint [29].

What is more, FTIR is fundamental in studying the interaction between aerogel components and any modifications introduced during their synthesis. The obtained information can be used to optimize the synthesis process, enhance material properties, and tailor aerogels for specific applications like environmental remediation, catalysis, or as lightweight and efficient thermal insulators. The detailed chemical insights gained through FTIR analysis contribute to a

comprehensive understanding of aerogel composition, guiding the development of advanced materials with tailored functionalities [29].

The experimental studies reported in the present thesis have been conducted with a *Equinox 55 Bruker* instrument. Spectra are recorded at a resolution of 2 cm^{-1} on pelletized powders after outgassing the sample at room temperature (residual pressure of 0.1 Pa). For IR analysis with "probe molecules" (in this case CO_2), the samples were degassed at a temperature of 120 °C for one hour. The obtained information is the identification of the functional groups present in the sample.

2.3.2 TGA

The TGA curve typically illustrates the weight loss of materials as a function of temperature. This analysis helps understand how a material responds to changes in temperature. As the temperature increases, the TGA curve may reveal distinct stages of weight loss corresponding to processes such as desorption of physically adsorbed water, decomposition of organic components, or structural rearrangements [30].

Understanding the TGA curve is crucial for optimizing the synthesis and application of aerogels, as it provides insights into their thermal behaviour and stability under different conditions [30].

The present experimentation utilises a *DSC/TGA 92-16.18 Setaram apparatus*. Approximately 10-20 mg of the specimen are deposited into an alumina crucible. A gradual heating ramp of 10 °C/min is implemented until a temperature of 800 °C is reached. The procedure is conducted in a regulated environment, employing a flux of oxygen to facilitate the elimination of volatile degradation by-products.

2.3.3 X-ray diffraction

X-Ray Diffraction (XRD) analysis, at high and low angles, respectively, plays a pivotal role in determining the crystalline structure and porous order of aerogels [31], [32]. Low-angle analyses allow the order of the long-range structure to be evaluated, i.e. to verify whether the porosities of the sample are ordered (in this case peaks at low angles are observed) or not. At high angles, peaks are an index of the order that occurs on the short (atomic) range, i.e. the crystallinity [31], [32].

XRD patterns reveal diffraction peaks corresponding to specific crystal planes, aiding researchers in identifying the crystalline phases potentially present in the aerogel matrix. This insight is particularly crucial for understanding the impact of synthesis parameters and thermal treatment on the resulting structure and for tailoring aerogels with enhanced properties. The detailed structural

information obtained through XRD analysis advances the design and development of aerogels with precisely tuned properties for diverse technological applications [33], [34].

X-Ray Diffraction data are here obtained through the utilization of a *Panalytical Empyrean instrument* (Cu Kα radiation, Malvern Panalytical, Almelo, The Netherlands) operating at 40 kV and 40 mA, equipped with a solid-state detector (PIXcel1D). The measurements are conducted both within a high-angle (5-60°) and low-angle range (0.7-10°).

2.3.4 N_2 adsorption

Nitrogen adsorption is a widely employed technique for characterizing the textural properties of materials. By subjecting samples to nitrogen gas at varying pressures (the temperature is maintained constant at 77 K), it is possible to investigate their adsorption and desorption behaviours, so revealing crucial information about pore size distribution and specific surface area. The resulting nitrogen adsorption isotherm typically classifies materials into various categories, such as type I, II, III, or IV, each one being indicative of different pore structures [35], [36], [37].

The nitrogen adsorption-desorption isotherms reported in this work are procured by employing an *ASAP 2020 Plus analyzer* (Micromeritics, Norcross, GA, USA). Before conducting the analysis, all samples undergo degassing at 70 °C under a nitrogen atmosphere with a pressure of 10 mmHg for 3 hours. The determination of the surface area utilises the Brunauer–Emmett–Teller (BET) method, while the calculation of the pore volume employs the Barrett–Joyner–Halenda (BJH) method, based on desorption isothermal data.

The Brunauer–Emmett–Teller formulation stands as the predominant method utilized for assessing the surface area of porous materials. Initially developed with the assumption of a statistical multilayer coverage on non-microporous surfaces, was later applied to microporous materials under specific conditions. Within the BET theory, the interactions between adjacent adsorbed molecules, except those in the vertical direction, are considered negligible. Additionally, it presumes that the adsorption energy remains constant across the different adsorption sites. This approach helps achieve precise measurements of specific surface areas, reaching values as low as 0.01 $m^2 g^{-1}$, and allows for the determination of pore diameters spanning from 0.3 to 100 nm, achieved by analysing the interaction between a gas, such as N_2, and the adsorbent material [2], [28].

The Barrett-Joyner-Halenda is the prevailing approach for determining the pore volume and pore-size distribution within mesoporous solids, employing principles derived from the Kelvin equation. This theory relies on two primary assumptions: firstly, pores possess a cylindrical shape, and secondly, the amount of adsorbate results from both physical adsorption on pore walls and

capillary condensation occurring within mesopores. However, it has been observed that Kelvin-based equations, such as those employed in the BJH method, tend to underestimate pore size, particularly for narrow mesopores with diameters below 10 nm, by approximately 20–30% [2], [28].

Aerogels, renowned for their high porosity and surface area, often exhibit pronounced nitrogen adsorption, highlighting their suitability for applications like gas storage, catalysis, and environmental remediation. The nitrogen adsorption analysis not only quantifies the extent of microporosity and mesoporosity but also aids in optimizing the synthesis parameters to tailor aerogels with desired pore characteristics for specific industrial or scientific purposes [37].

2.3.5 XPS

X-ray Photoelectron Spectroscopy (XPS) stands as a potent technique capable of furnishing crucial data regarding elemental composition, oxidation states of elements, and, under favourable circumstances, the distribution of one phase relative to another. Widely employed in investigating metal-oxide interactions, XPS offers insights into electronic structures at interfaces, facilitating the comprehension of charge transfer phenomena at metal/oxide interfaces. Moreover, its surface sensitivity enables the detection of minute alterations in surface chemical composition [38]. By bombarding a sample with X-rays, XPS generates photoelectrons from the material's surface. A deep study of these photoelectrons gives information about the elemental composition, chemical states, and bonding environments of the atoms within the top few nanometres of the sample. Through careful analysis of the emitted photoelectrons' energies, it is possible to obtain details about oxidation states, chemical interactions, and surface contaminants present in the material [39].

In this work, a VersaProbe 5000 by Physical Electronic instrument, with a monochromatic radiation source AL Kalpha 1486.6 eV, was employed. Initially, a thoroughgoing analysis is garnered via a survey spectrum, encompassing all discernible signals. Following this, detailed spectra concentrating on singular elements such as Carbon (C), Oxygen (O), Nitrogen (N), and Aluminium (Al) are procured to distinguish their distinct chemical contexts.

2.4 CO_2 adsorption - volumetric

The analysis for carbon dioxide adsorption is conducted utilizing the same instrument employed for nitrogen adsorption, namely an *ASAP 2020 Plus analyzer* (Micromeritics, Norcross, GA, USA). Before the analysis, all samples undergo degassing at 120°C under a nitrogen atmosphere with a pressure of 10 mmHg for 2 hours. After this preparatory step, two consecutive runs are performed. The initial run aims to quantify the amount of CO_2 adsorbed, while the subsequent run

helps investigate the presence of any irreversible phenomena, providing a comprehensive understanding of the adsorption process. The first and the second run are executed at ambient temperature (25 °C) and between them, a degassing phase at ambient temperature is carried out.

2.5 CO_2 adsorption – in situ FTIR

The experimental studies reported in the present thesis have been conducted with an *Equinox 55 Bruker* instrument. In this case, a thin tablet of aerogel was positioned in the analysis cell and subjected to degassing at 120 °C for 2h (residual pressure of 0.1 Pa) to remove any residual moisture and contamination from the pores. Subsequently, the cell was connected to a source of pure carbon dioxide to introduce increasing gas quantities (at room temperature) into the sample and FTIR spectra were acquired at the same time. Finally, the cell was connected to an empty line to remove the carbon dioxide at room temperature and a last FTIR spectrum was acquired.

Chapter 3

Alumina-silica aerogels

3.1 Introduction

The first step involves the formation of the alumina-silica aerogels with the sol-gel process and the subsequent characterization of the sample. This allows a precise technique for the formation of the reference aerogel to be established.

3.2 Preparation of AlSi aerogel

3.2.1 Gel synthesis

The synthesis was inspired by that of Tamon et al. [40]

- For the preparation of the solution A: TMOS in 2 – butanol and HCl solution 0.01 M.
- For the preparation of the solution B: 20 wt.% ATSB in 2 – butanol.

The proportions employed in the synthesis by Tamon et al. [40] were adopted to calculate the mass of the chemicals. ***Table 4*** illustrates the molar ratio between reagents of AlSi normalised on TMOS + ATSB.

Table 4: Molar ratio between reagents of AlSi

Sample	ATSB	TMOS	TMOS + ATSB	Ammonia Solution 1.0 M	HCl solution 0.01 M	2 – butanol	H_2O^*
AlSi	0.1	0.9	1	8	0.9	6	8.9

*This value represents the sum of moles of the water in ammonia solution and HCl solution.

According to **Table *4***, the following calculations were performed (it has been assumed M=18,01 g/mol e rho=1,00 g/mL):

- 0.9 mol TMOS → 0.9 mol H_2O in HCl solution → 16.21 g = $16.2 \cdot 10^{-3}$ L H_2O → $1.62 \cdot 10^{-4}$ mol or $5.900 \cdot 10^{-3}$ g of pure HCl
- 0.1 mol ATSB (0.1 mol corresponds to 24.63 g of ATSB) $\xrightarrow{20\ wt.\%}$ 20 : 80 = 24.63 : x → x = 98.53 g of 2 – butanol

- 8 mol H_2O in Ammonia solution → 144.1 g = $144 \cdot 10^{-3}$ L H_2O → 0.14408 pure NH_3 → 2.454 pure g NH_3
- 6 mol 2 – butanol (444.7 g) of which 1.329 mol = 98.53 g for ATSB and 4.671 mol = 346.2 g for TMOS

The above-calculated quantities were scaled to obtain the following masses of reagents (***Table 5***):

Table 5: Theoretical mass quantity of reagents

Sample	ATSB	TMOS	Ammonia Solution 1.0 M	HCl solution 0.01 M	2 – butanol
AlSi	1.6603 g	9.1533 g	9.6010 g	1.2415 g	23.0882 g

For the synthesis, cylindrical beakers of 25 mL (primarily for the preparation of solution B) and 100 mL (for solution A and the final solution A+B) were utilized. Subsequently, the beakers were covered with parafilm. A magnetic stirrer, "*IKA Werke*," was used for agitation. For heating, the solutions were placed in a thermostatic bath heated on the magnetic stirrer plate ("*AREX - Heating Magnetic Stirrer*") with a probe for temperature control ("*VTF - Digital Thermoregulator*").

Firstly, solution A was prepared, and mixed at around 200 rpm at ambient temperature for 1.5 hours. Secondly, solution B was obtained and mixed at around 200 rpm at ambient temperature for 5 minutes. After, solutions A and B were mixed at 80 °C for two hours. In the end, Ammonia solution (1.0 M) was added; after a couple of minutes the stirring was stopped, the solution was poured into a beaker containing cylindrical glass moulds and it was kept at 80 °C until jellification was reached. Finally, the gel was typically formed within a few minutes. Once the samples of gel were ready, they were covered with ethanol for a week for ageing. Ageing serves to strengthen the structure of the alumina-silica network. The hydrolysis and condensation reactions can also require a prolonged time; therefore, they continue to occur even during ageing, consolidating the structure. Therefore, more bridges should condense and form, making the structure more resistant [41]. The sample was covered with ethanol to avoid solvent evaporation from the gel (which would result in the formation of a xerogel) (**Figure *11***).

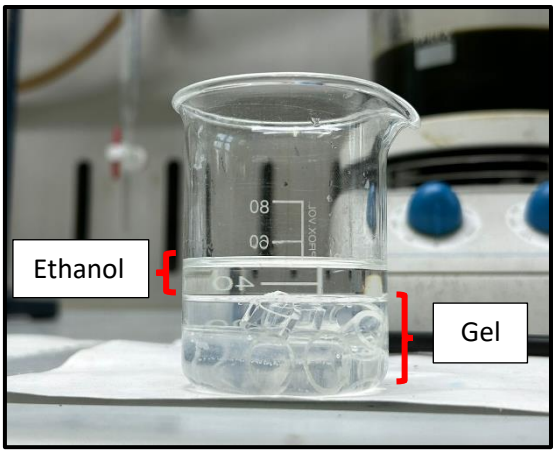

Figure 11: The sample covered with ethanol.

After a week, the gel samples, inside glass cylinders, have the shape shown in **Figure *12***:

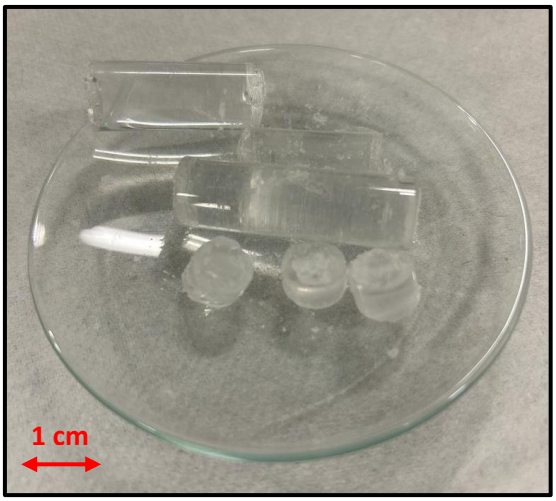

Figure 12: Samples of gels after being covered for a week with ethanol.

3.2.2 Supercritical drying process

The gels underwent supercritical drying with carbon dioxide in an autoclave (40 mL stainless steel vessel with an internal diameter of 14 mm), where samples were separated with glass wool and initially immersed in ethanol (***Figure 13***).

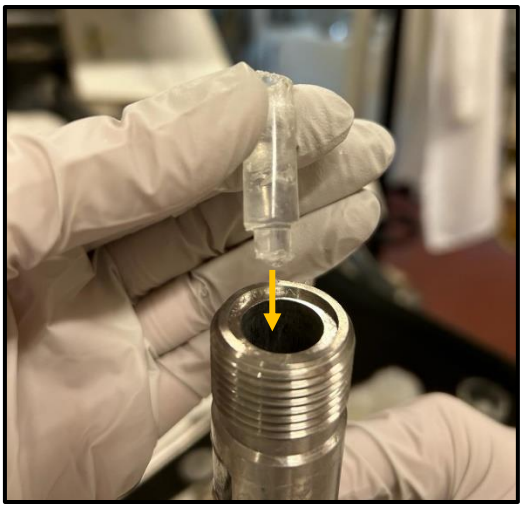

Figure 13: Al - Si aerogel in autoclave.

Subsequently, the autoclave underwent pressurization to 105 bar using carbon dioxide and it was heated up to 40 °C, over 90 minutes (***Figure 14***).

Figure 14: Autoclave.

After the extraction of ethanol, the autoclave was subjected to depressurization (at 5 ml/min) followed by natural cooling. Ultimately, samples of aerogel were acquired.

The formed aerogels underwent a slight volume shrinkage. The noticeable variance in diameter between the specimen and the encompassing mould is evident (***Figure 15, Figure 16***).

Figure 15: Samples after supercritical drying.

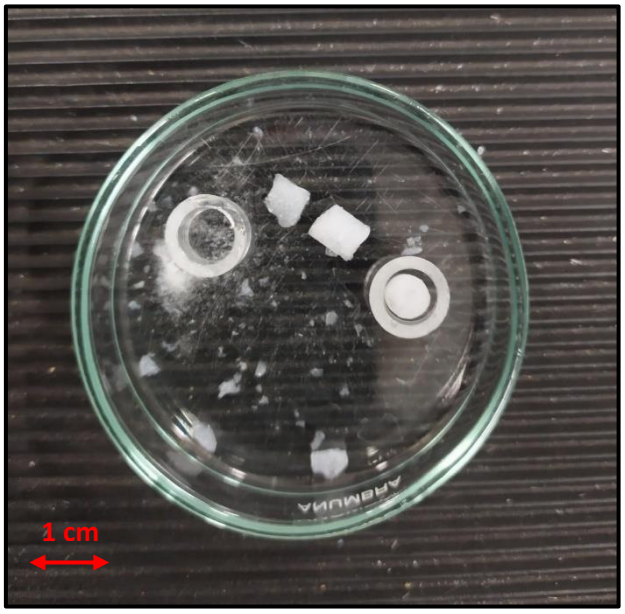

Figure 16: Focus on the volume shrinkage.

A precision balance was employed for weighing with a single measurement (one measurement of diameter and one measurement of the length were conducted). It was assumed that the aerogel would retain a cylindrical shape corresponding to the geometry of the moulds.

Table 6 shows the dimensions, density, and volume shrinkage of the different samples. The internal diameters of the glass cylinders are 10.8 mm and 7 mm. The volumetric shrinkage was calculated starting from the shrinkage of the diameter and length. The shrinkage of the diameter was calculated by measuring the initial and final diameter, while for the shrinkage of the length (since the initial length of the samples is not known) it was assumed that it is equal in percentage to that of the diameter.

Table 6: Dimensions, density, and volume shrinkage of Al-Si aerogel samples

Internal diameter, cm	h, cm	Final volume, cm^3	Starting volume, cm^3	Volume shrinkage, cm^3	Weight, g	Apparent density, g/cm^3
0.58	1.13	0.30	0.52	0.22	0.0384	0.13
0.58	1.49	0.39	0.69	0.30	0.0574	0.15
0.58	1.60	0.42	0.74	0.32	0.0700	0.17
0.88	1.57	0.95	1.78	0.83	0.1591	0.17
0.83	2.33	1.26	2.77	1.51	0.2268	0.18

The obtained density range of the aerogels, which falls between 0.13 and 0.18 g/cm^3, aligns closely with the findings documented in the literature [6], [11].

3.3 Characterization

3.3.1 FTIR

The composition of the alumina-silica aerogel can be further studied by FTIR analysis (***Figure 17***). The broadband between 3200 and 3700 cm^{-1} is attributable to –OH which can be either silica (silanols) or alumina [42]. The peaks around 2900 cm^{-1} can be ascribed to -CH groups of organic components [43]. This likely happens because one of the precursor molecules (most probably ATSB) is not completely hydrolysed, and some alkyl chains remain in the material. This phenomenon is also observed with similar precursors in the formation of titania aerogels [40]. It is, therefore, necessary to evaluate whether the presence of organic components can influence the effectiveness of the sample and understand whether a heat treatment is necessary to remove the organic component, keeping in mind that a thermal treatment would certainly alter the specific surface and porosity of the samples. According to the literature, -OH groups from adsorbed water also give a signal around 1640 cm^{-1} [44]. The various peaks around 1400 cm^{-1} are also probably attributable to the presence of N [42], [45], [46].

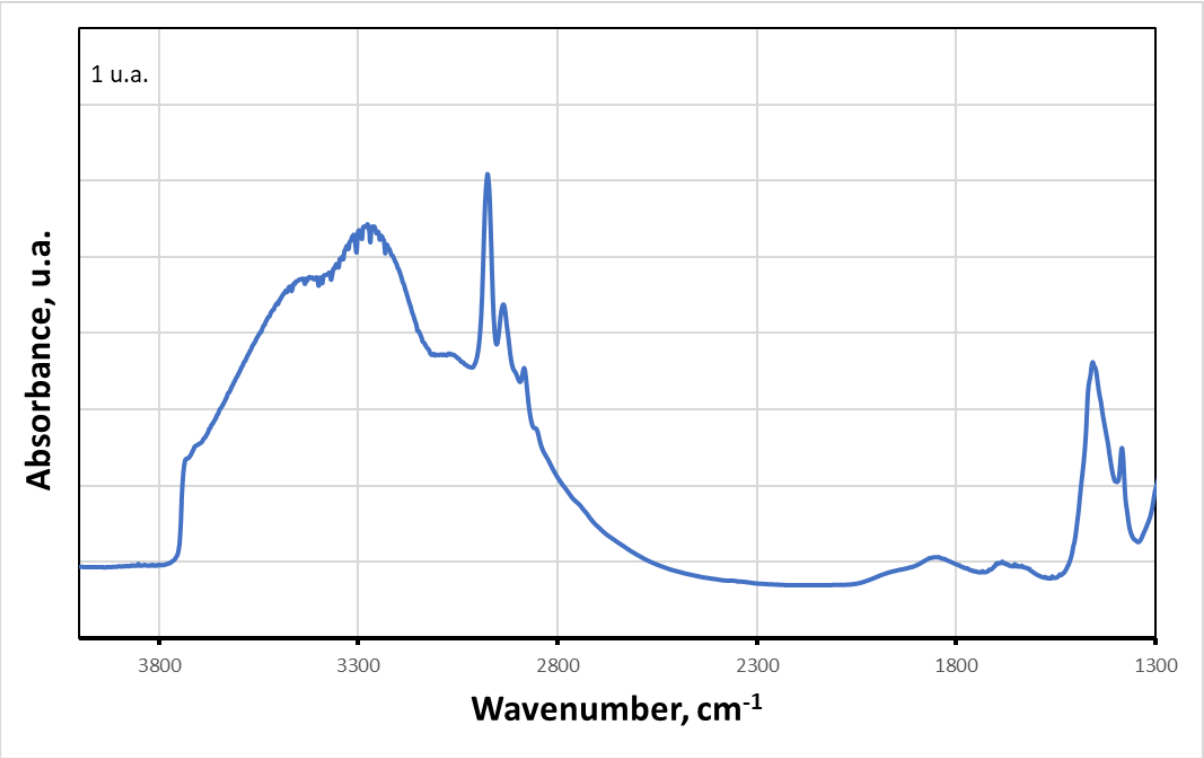

Figure 17: FTIR of Al-Si aerogel.

3.3.2 TGA

The samples of alumina-silica aerogels exhibit weight losses with the temperature rise (***Figure 18***). When a TGA analysis is carried out on pure silica (without organic components) this loses physiosorbed water (5-10 wt.% depending on the hydrophilicity of the silica) when it is heated up to 150 °C and then, mass loss occurs above 300 °C due to the condensation of the vicinal silanols (silanol condensation, in fact, results in water release) [47]. This second loss usually accounts for a 1-2 wt.% mass decrease.

Before 150 °C, the Al-Si aerogels experience a mass loss of 20.6 %, while, between 150 °C and 800 °C, the mass loss is approximately 32.6 %. This last value is considerably higher than that ascribable to the condensation of the silanols and, for this reason, it can be attributed to the degradation of residual organic components from the synthesis process, in agreement with what was observed with the FTIR analyses [47].

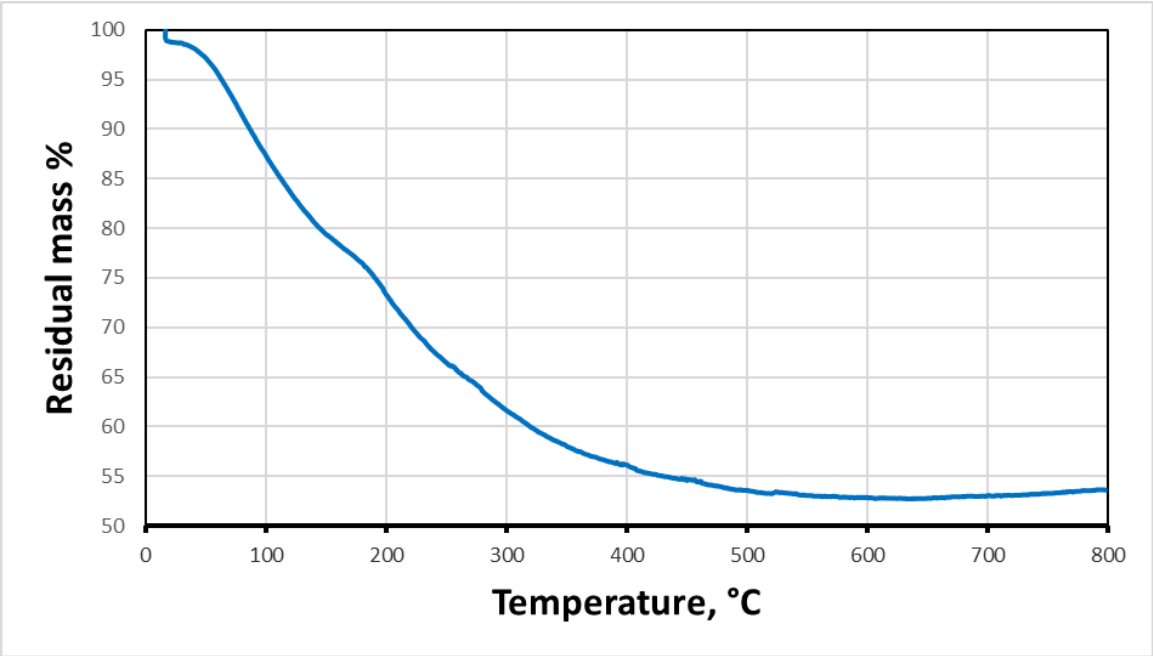

Figure 18: Residual mass % vs Temperature of Al-Si aerogel.

It is interesting to observe that the mass rises at the end of the test. This is an artefact due to a buoyancy effect (artefact is observed for all samples).

3.3.3 X-ray diffraction

The XRD technique was used at high angles to check if the material is crystalline or amorphous and at low angles to observe the possible presence of an ordered mesostructure.

At high angles (where short-range order occurs, i.e., crystalline order), the sample presents only an amorphous halo, i.e., not crystalline (***Figure 19***). This is consistent with the synthesis method since the sol-gel process leads to amorphous structures [32], [35], [36].

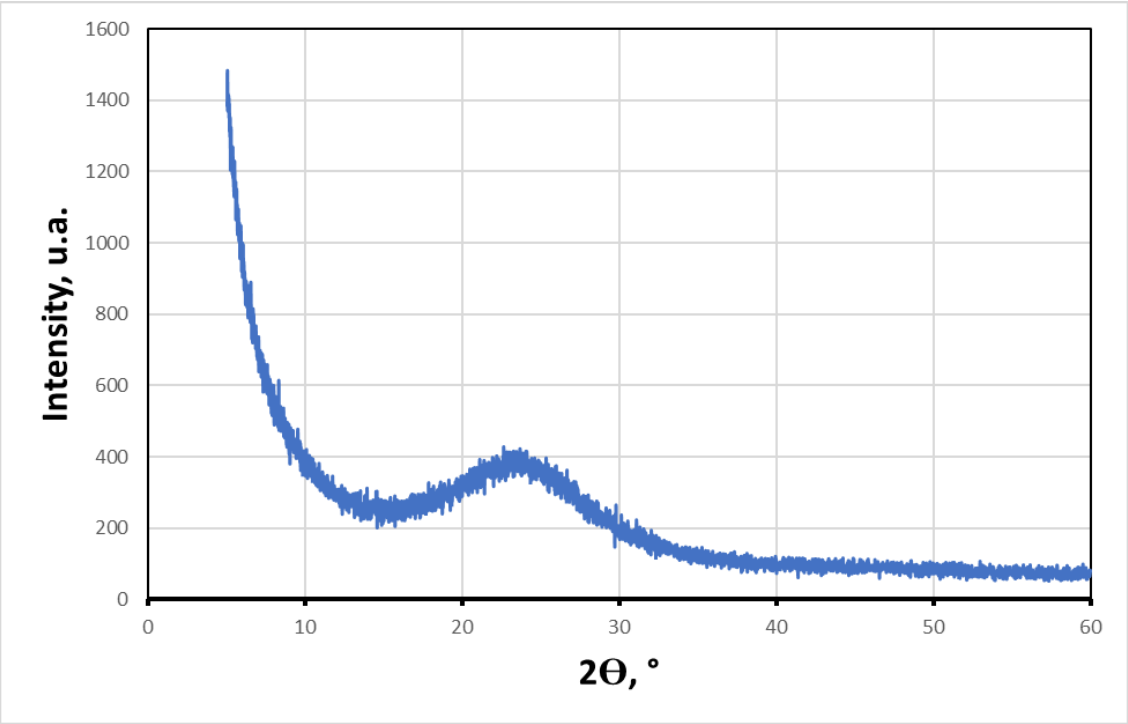

Figure 19: XRD Al-Si aerogel at high angles.

At low angles, where long-range ordering occurs (typically the presence of ordered mesoporosity) a rather broad peak above 2° is observed (***Figure 20***). This could be indicative of a lamellar structure [31], [33], [48].

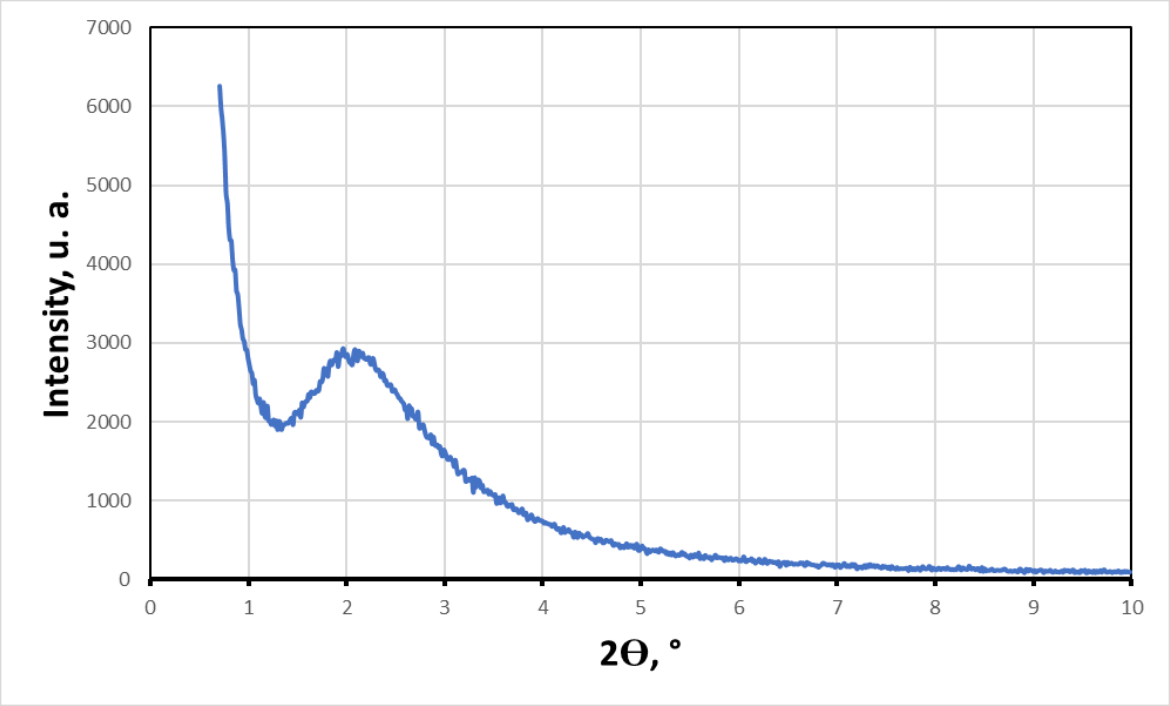

Figure 20: XRD Al-Si aerogel at low angles.

3.3.4 N_2 adsorption

The textural properties of the aerogel samples were evaluated by using the nitrogen adsorption/desorption test.

- Nitrogen adsorption isotherm

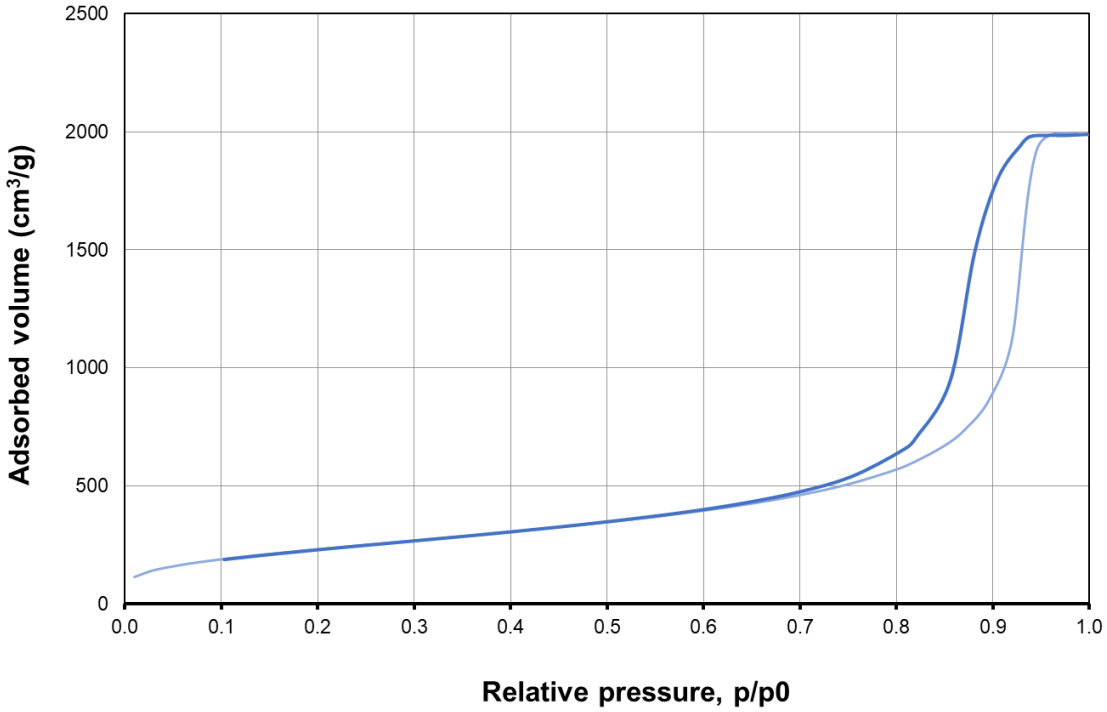

Figure 21: BET curve of Al-Si aerogel.

The specific surface area is calculated according to the Brunauer–Emmett–Teller (BET) method. The curve is type IV according to the IUPAC classification with a loop of type H1. This means that the material is mesoporous with uniform porosities and in a narrow range [49], [50]. The specific surface area is 868 m^2/g. It is a high value and comparable to that reported in the literature for similar systems [40]. The porous volume is 3.0 cm^3/g (***Figure 21***).

- BJH Graph

The pore volume and pore size distributions are obtained with the total adsorbed volume and the desorption data according to the Barret–Joyner–Halenda (BJH) method (***Figure 22***) [51]. The distribution is single-mode, rather narrow, and with a maximum of approximately 15.2 nm. This indicates that the pores are uniform in size and belong to the meso-range [49].

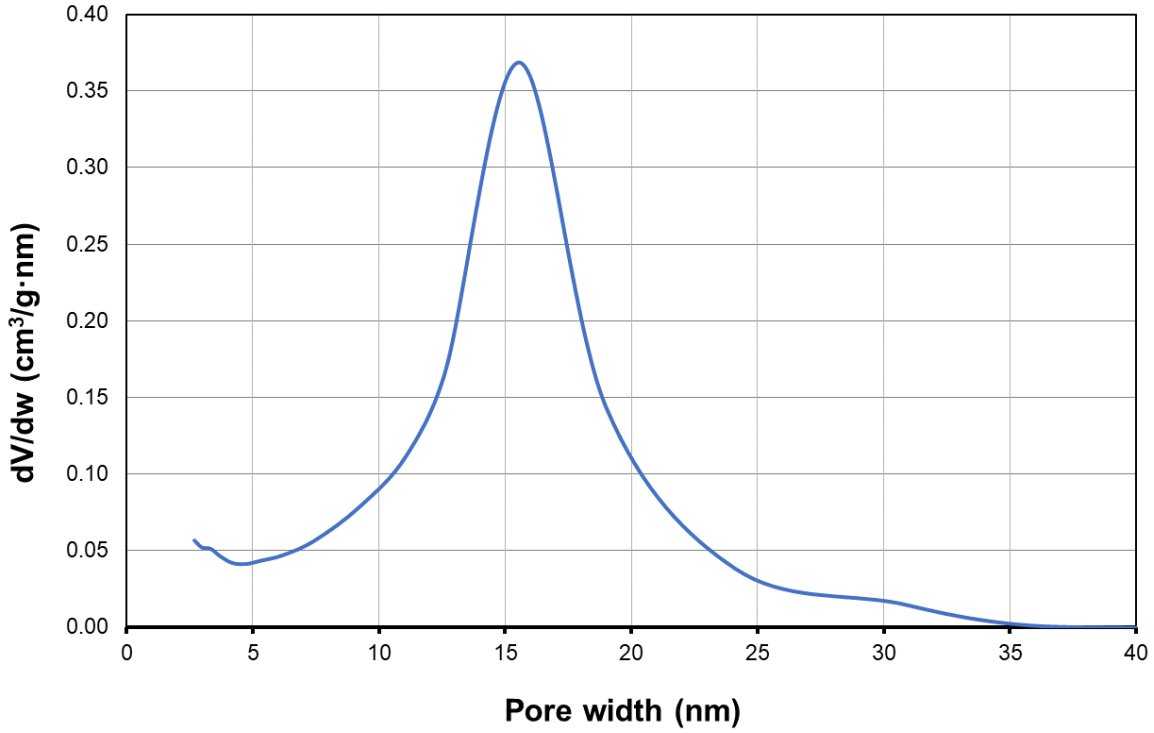

Figure 22: BJH curve of Al-Si aerogel.

Table 7 shows a summary of the textural properties of Al-Si samples.

Table 7: Summary of the textural properties of Al-Si aerogels

TEXTURAL PROPERTIES		
Specific surface area	**Porous volume**	**Average pore diameter**
868 m^2/g	3.0 cm^3/g	15.2 nm

3.3.5 XPS

XPS analysis facilitates elucidating a material surface's elemental composition and chemical environment [52]. This analytical technique provides invaluable insights into samples' elemental composition, chemical states, and surface morphology [39].

Initially, a comprehensive overview is obtained through a survey spectrum, encompassing all signals (***Figure 23***). Subsequently, high-resolution spectra focusing on individual elements, namely Carbon (C) (***Figure 24***), Oxygen (O) (***Figure 25***), Nitrogen (N) (***Figure 26*****Figure *26***), and Aluminium (Al) (***Figure 27***), are acquired. The atomic percentages of these elements are delineated on the survey spectrum for a comprehensive understanding. Notably, in the AlSi sample, the presence of Aluminium (Al) is relatively limited, accompanied by detectable Nitrogen (N) content, highlighting a nuanced chemical composition deserving further investigation.

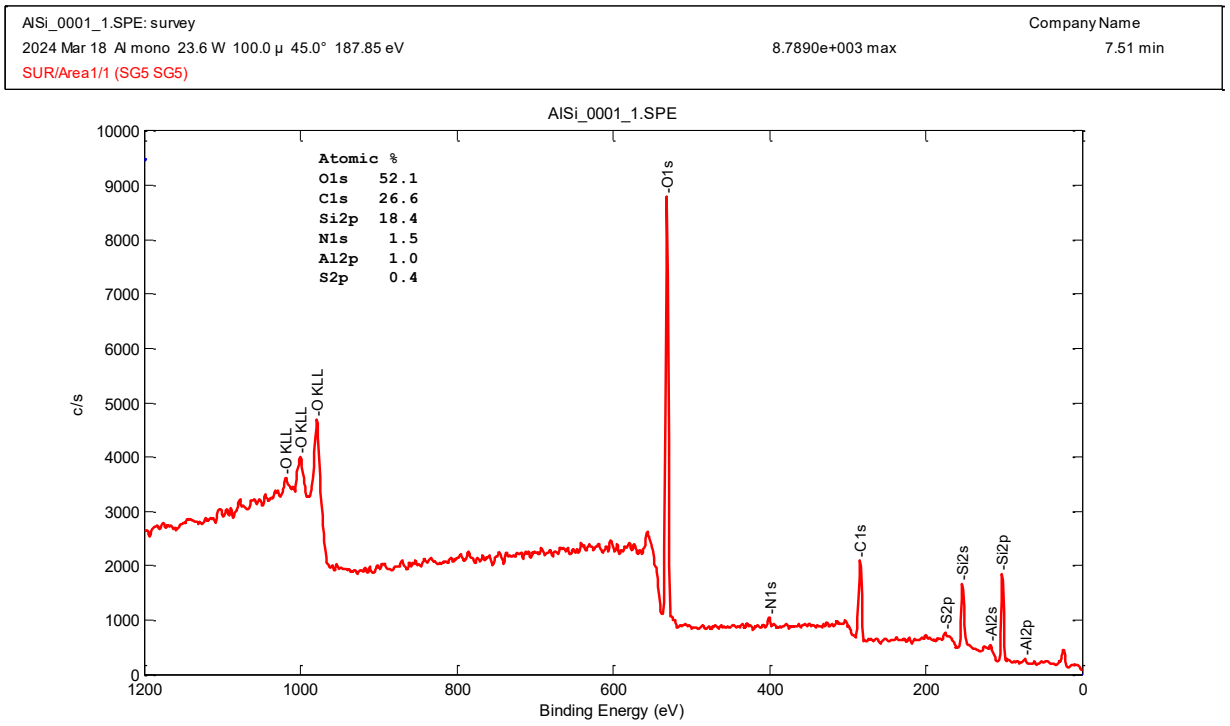

Figure 23: Survey of AlSi sample.

In ***Figure 24***, the peak at 285 eV indicates the presence of Carbon, according to the results obtained by Tago T. [53].

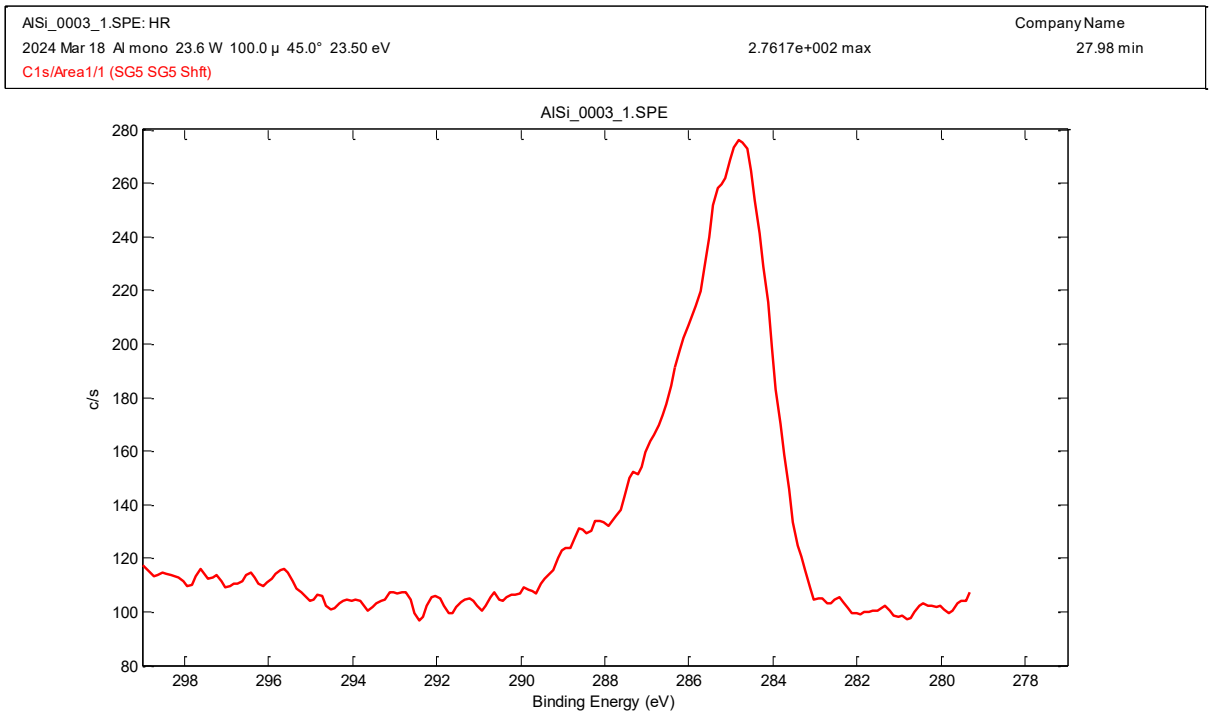

Figure 24: high-resolution spectra of C in AlSi sample.

In ***Figure 25***, the peak at 533 eV shows the presence of Oxygen and this is in line with what can be found in the literature [38], [52].

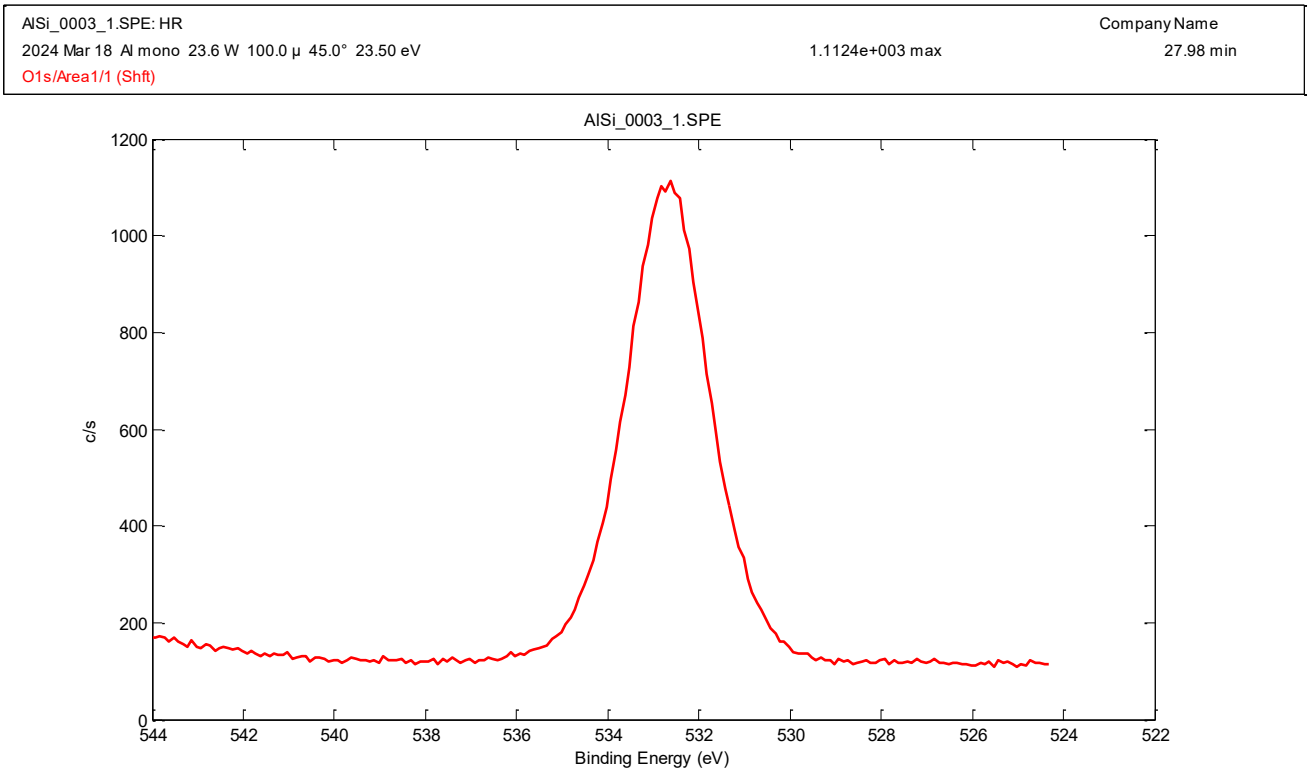

Figure 25: high-resolution spectra of O in AlSi sample.

In ***Figure 26***, the presence of deprotonated and protonated nitrogen is shown through the peaks at 399.6 and 401.7 eV, respectively, which is also confirmed in the works by Zhu W. [54] and Brunel [55]. However, it can be noted that the N signal is low and disturbed, which is consistent with the IR peak around 1450 cm^{-1}.

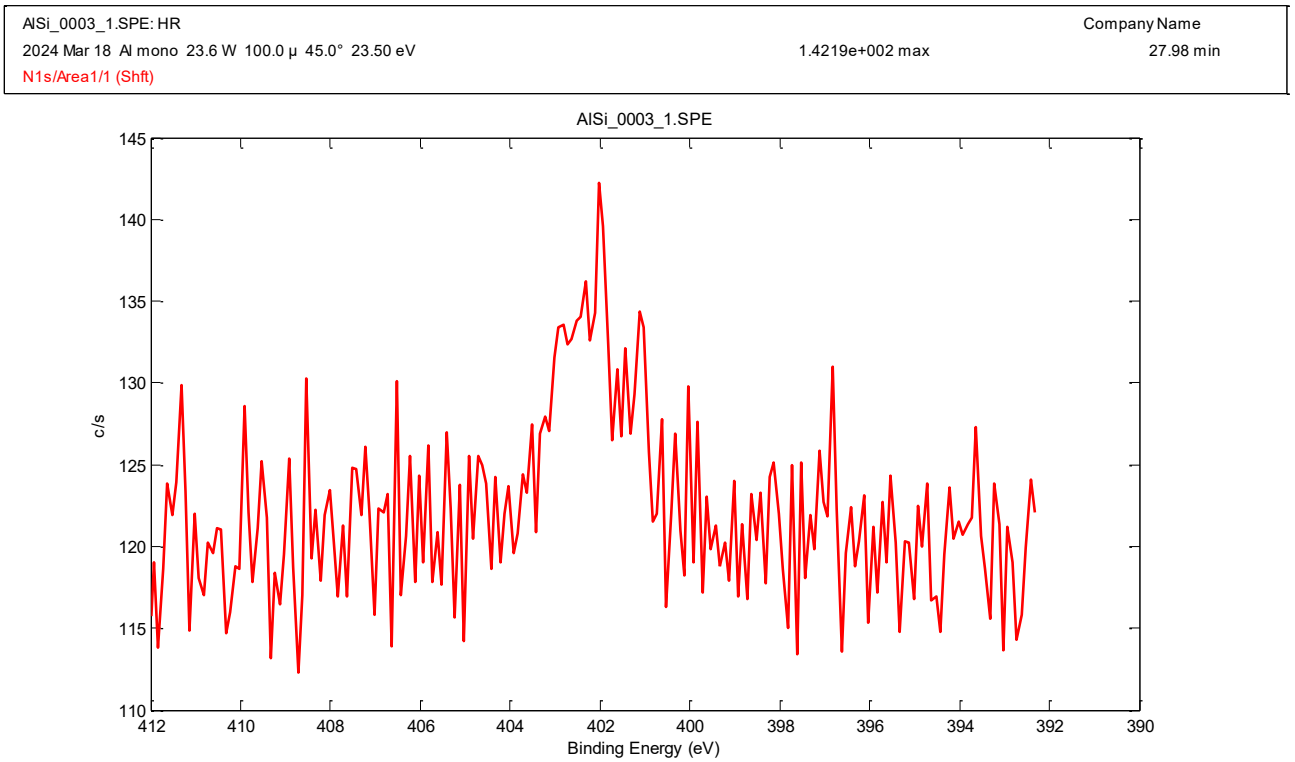

Figure 26: high-resolution spectra of N in AlSi sample.

In ***Figure 27***, the highest peak detected is at 75 eV and it can be attributed to Al since it is similar to the results obtained by Figueiredo N. [38].

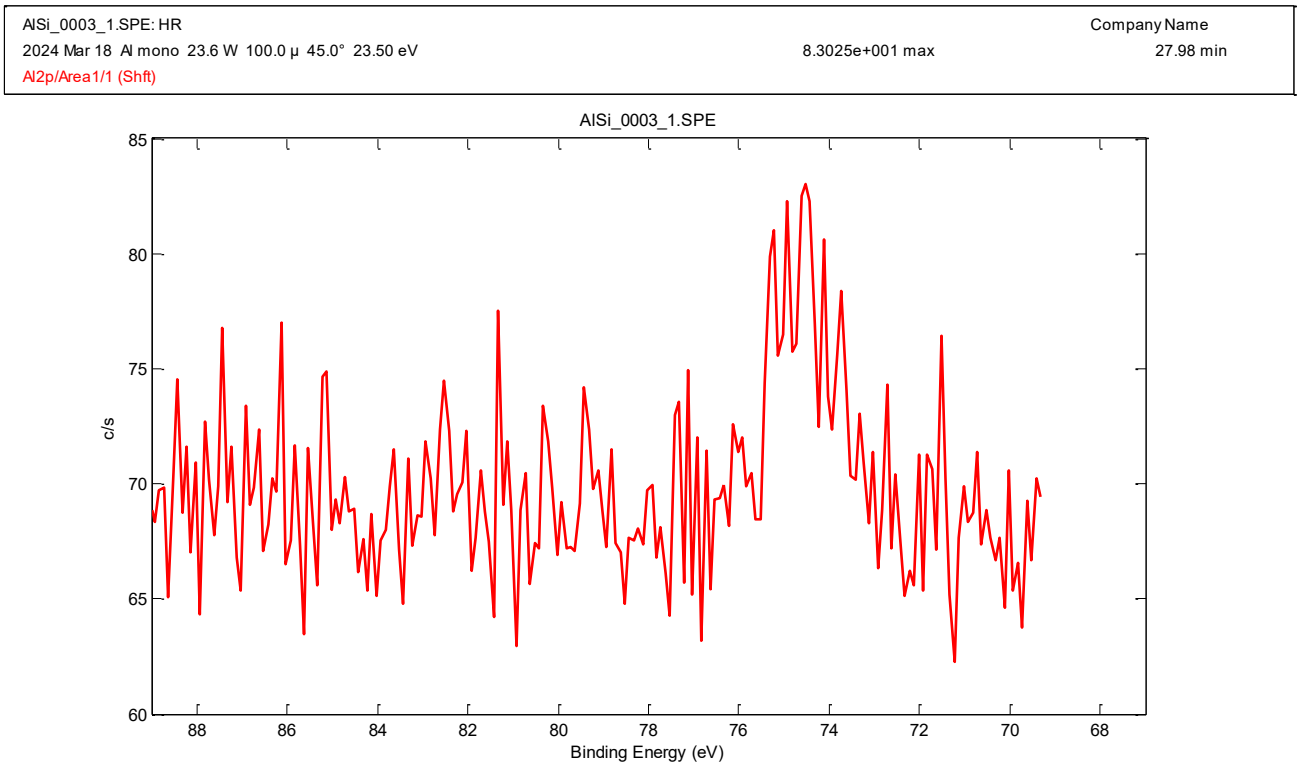

Figure 27: high-resolution spectra of Al in AlSi sample.

3.4 Preparation of AlSi_H_2O_prima

3.4.1 Gel synthesis

Following the previous considerations, the purpose of this second attempt of synthesis is to eliminate/reduce the organic residues in the samples. To pursue this objective, it is hypothesized that the presence of the residues is due to poor hydrolysis of the precursors. Indeed, most of the water is added with the basic catalyst, i.e. in the final phase of the synthesis and may, therefore, not provide the precursors sufficient time to hydrolyse completely. Therefore, water is here added at an early stage of the synthesis (without altering the molar ratios compared to the AlSi synthesis). The amount of water in the catalyst solution (which is now more concentrated than that of the previous AlSi sample) is reduced to allow it to be added during the early stages of the synthesis procedure and not only in the last step (i.e. when the basic catalyst is added) (***Table 8***, ***Table 9***).

Table 8: Mass quantities of reagents of solution A

Solution	2 – butanol	TMOS	HCl solution 0.01 M
Solution A	5.7816 g	2.2890 g	0.3108 g

Table 9: Mass quantities of reagents of solution B

Solution	2 – butanol	ATSB
Solution B	1.6539 g	0.4510 g

Additional reagents:

- H_2O = 1.2400 g
- Ammonia solution (2.0 M) = 1.2146 g

For the synthesis, cylindrical beakers of 25 mL (primarily for the preparation of solution B) and 100 mL (for solution A and the final solution A+B) were utilized. Subsequently, the beakers were covered with parafilm. A magnetic stirrer, "*IKA Werke*," was used for agitation. For heating, the solutions were placed in a thermostatic bath heated on the magnetic stirrer plate ("*AREX - Heating Magnetic Stirrer*") with a probe for temperature control ("*VTF - Digital Thermoregulator*").

Initially, solution A underwent preparation, being stirred at an ambient temperature, at around 200 rpm for 1 hour and 30 minutes. Subsequently, solution B was prepared and mixed under similar conditions for 5 minutes. A combination of solutions A and B was stirred for approximately 1 hour, then, water was introduced, and the solution was mixed for another hour. After, ammonia solution (2.0 M) was added, and the resulting solution was poured into a beaker housing cylindrical glass moulds waiting for the gel to be formed at ambient temperature. Since the solution was still liquid after an entire night, the samples were heated at 80 °C for about 20 minutes to achieve gelation. (***Figure 28***). After gelation, the samples were covered with ethanol and left to age for 1 week.

Figure 28: Samples of AlSi_H_2O_prima.

3.4.2 Supercritical drying process

The gels underwent supercritical drying utilizing carbon dioxide in an autoclave (40 mL stainless steel vessel with an internal diameter of 14 mm) for 90 minutes under conditions of 105 bar and 40 °C. During this process, samples were partitioned using glass wool and initially immersed in ethanol. The resultant aerogels experienced volume shrinkage (***Figure 29***). It can also be observed that the samples are opaque and chalk-like. This change in appearance, with respect to the AlSi sample, is probably attributable to the early addition of water since already the gel was whitish.

Figure 29: Sample of AlSi_H_2O_prima after the supercritical drying process.

A precision balance was employed for weighing with a single measurement (one measurement of diameter and one measurement of the length were conducted). It was assumed that the aerogel would retain a cylindrical shape corresponding to the geometry of the moulds.

Table *10* shows the dimensions, density, and volume shrinkage of the sample. The internal diameters of the glass cylinders are 10.8 mm and 7 mm. The volumetric shrinkage was calculated starting from the shrinkage of the diameter and length. The shrinkage of the diameter was calculated by measuring the initial and final diameter, while for the shrinkage of the length (since the initial length of the samples is not known) it was assumed that it is equal in percentage to that of the diameter.

Table 10: Dimensions, density, and volume shrinkage of AlSi_H_2O_prima aerogel

Internal diameter, cm	h, cm	Final volume, cm^3	Starting volume, cm^3	Volume shrinkage, cm^3	Weight, g	Apparent density, g/cm^3
0.97	1.09	0.81	1.11	0.30	0.1656	0.21

3.5 Characterisation of AlSi_H_2O_prima

3.5.1 FTIR

The analysis of the alumina-silica aerogel composition can be conducted through FTIR examination (refer to ***Figure 30***). The broad spectrum within the range of 3200 to 3700 cm^{-1} is associated with –OH groups. Peaks observed around 2900 cm^{-1} are linked to -CH groups from organic components. However, their relative intensity is decidedly lower than the similar peaks found for AlSi. It indicates that this strategy may have worked in promoting greater hydrolysis of the precursors. As reported in the literature, -OH groups from adsorbed water contribute to a signal around 1640 cm^{-1} [44]. The diverse peaks in the vicinity of 1400 cm^{-1} are also likely attributed to the presence of N [42], [43], [45], [46].

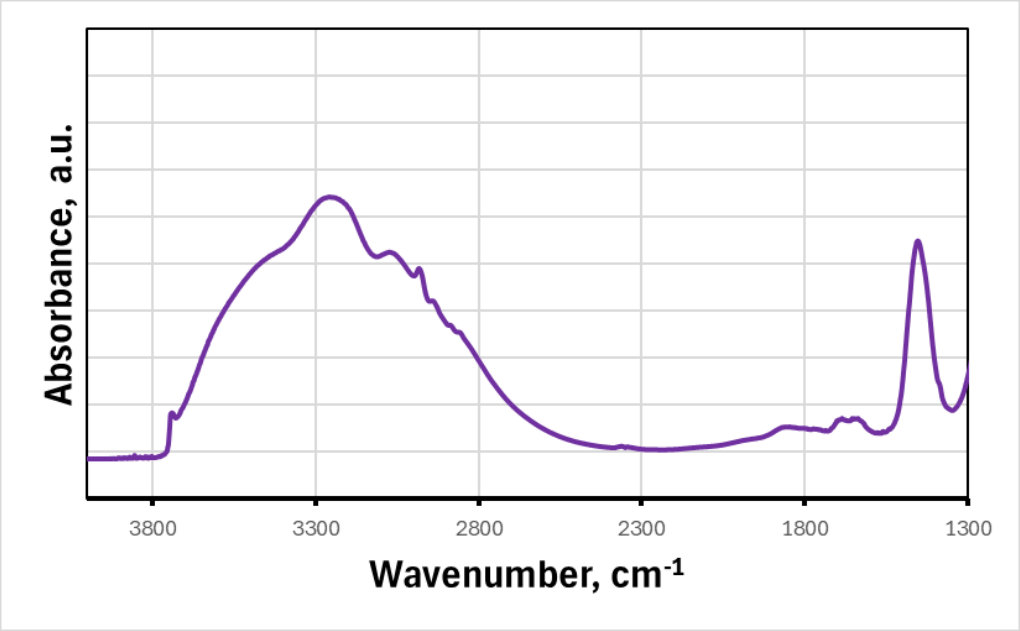

Figure 30: FTIR of AlSi_H2O_prima aerogels.

3.5.2 TGA

The AlSi_H_2O_prima aerogel specimens demonstrate a reduction in weight as the temperature increases, as illustrated in ***Figure 31***. Up to 150 °C, there is a 10.6 % decrease in mass for the aerogels. In the temperature range from 150 °C to 800 °C, the mass loss amounts to around 17 %. This last datum can be considered an improvement with respect to the initial AlSi synthesis: the organic content decreased as was hypothesized since the hydrolysis of the precursors was promoted by the early addition of water.

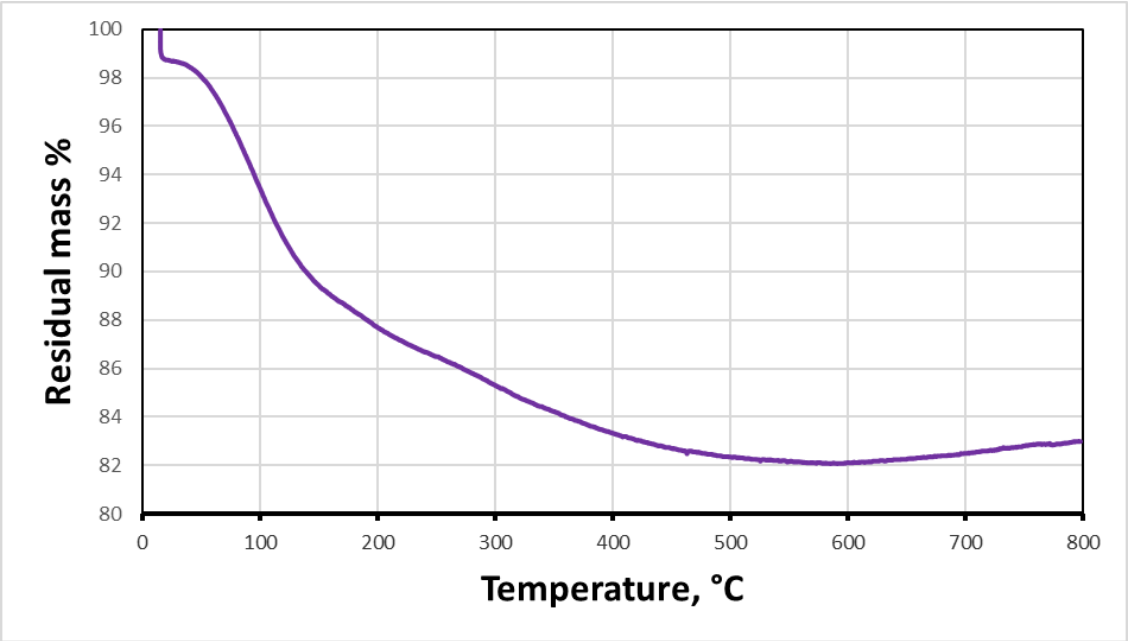

Figure 31: TGA of AlSi_H2O_prima.

It is interesting to observe that the mass rises at the end of the test. This is an artefact due to a buoyancy effect (artefact is observed for all samples).

3.6 Preparation of AlSi_H_2O_prima2

3.6.1 Gel synthesis

In the previous synthesis, AlSi_H_2O_prima, an energetic contribution (i.e. heating at 80°C for two hours) was provided to achieve gelation in a limited time. The purpose of the synthesis proposed in this section is to eliminate it by doubling the concentration of the ammonia solution. By doubling the basic catalyst amount, the gelation kinetics is expected to accelerate, so avoiding the above-cited energy input (

Table 11, ***Table 12***).

Table 11: Mass quantities of the reagents of Solution A

Solution	2 – butanol	TMOS	HCl solution 0.01 M
Solution A	5.7790 g	2.3060 g	0.3251 g

Table 12: Mass quantities of the reagents of the solution B

Solution	2 – butanol	ATSB

Solution B	1.6537 g	0.4162 g

Additional reagents included:

- H2O = 1.2345 g
- Ammonia solution (4.0 M) = 1.2550 g

For the synthesis, cylindrical beakers of 25 mL (primarily for the preparation of solution B) and 100 mL (for solution A and the final solution A+B) were utilized. Subsequently, the beakers were covered with parafilm. A magnetic stirrer, "*IKA Werke*," was used for agitation. For heating, the solutions were placed in a thermostatic bath heated on the magnetic stirrer plate ("*AREX - Heating Magnetic Stirrer*") with a probe for temperature control ("*VTF - Digital Thermoregulator*").

The same synthesis process of AlSi_H_2O_prima was followed. Since the solution remained liquid, the samples were again heated up to 80°C for approximately 20 minutes to induce gelation (***Figure 32***). Therefore, the increase in the catalyst content was not sufficient to significantly accelerate the gelation kinetics at ambient temperature. After gelation, the samples were covered with ethanol and left to age for 1 week.

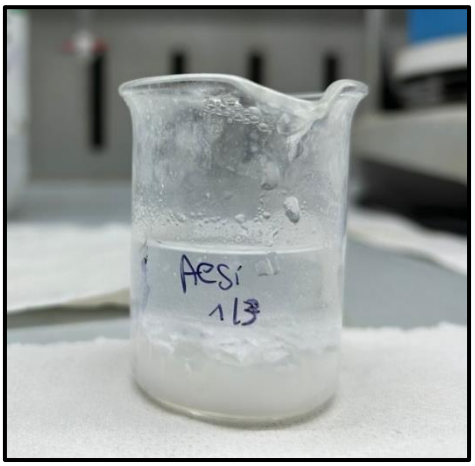

Figure 32: Gel of AlSi_H_2O_prima2.

3.6.2 Supercritical drying process

The gels were subjected to supercritical drying using carbon dioxide in an autoclave (40 mL stainless steel vessel with an internal diameter of 14 mm) for 90 minutes under conditions of 105 bar and 40 °C. Throughout this procedure, samples were separated using glass wool and initially soaked in ethanol. The resulting aerogels exhibited volume reduction (***Figure 33***, ***Figure 34***). These samples have a chalk-like appearance, like the previous ones.

Figure 33: Aerogels of the AlSi_H_2O_prima2.

Figure 34: Aerogels of the AlSi_H_2O_prima2 without glass cylinders.

A precision balance was employed for weighing with a single measurement (one measurement of diameter and one measurement of the length were conducted). It was assumed that the aerogel would retain a cylindrical shape corresponding to the geometry of the moulds.

Table 13 presents the dimensions, density, and volume shrinkage of various samples. The glass cylinders have internal diameters of 10.8 mm and 7 mm. The volumetric shrinkage was calculated starting from the shrinkage of the diameter and length. The shrinkage of the diameter was calculated

by measuring the initial and final diameter, while for the shrinkage of the length (since the initial length of the samples is not known) it was assumed that it is equal in percentage to that of the diameter.

Table 13: Dimensions, density, and volume shrinkage of AlSi_H2O_prima2 aerogels:

Internal diameter, cm	h, cm	Final volume, cm^3	Starting volume, cm^3	Volume shrinkage, cm^3	Weight, g	Apparent density, g/cm^3
1.07	1.04	0.94	0.96	0.02	0.1030	0.11
0.92	1.58	1.05	1.70	0.65	0.1224	0.12
0.63	0.71	0.22	0.30	0.08	0.0284	0.13
0.62	1.07	0.32	0.47	0.15	0.0336	0.10

3.7 Characterisation of AlSi_H_2O_prima2

3.7.1 FTIR

The investigation of the composition of alumina-silica aerogel can be explored by using FTIR analysis (see ***Figure 35***). Within the spectrum range from 3200 to 3700 cm^{-1}, the presence of –OH groups is evident. Additionally, peaks detected at around 2900 cm^{-1} correspond to -CH groups originating from organic constituents, and they are less pronounced when compared to those observed in the *AlSi_H_2O_prima* sample and, above all, in the AlSi sample. Previous studies have pointed out that the signal around 1640 cm^{-1} is indicative of the presence of Al-OH. Moreover, the various peaks near 1400 cm^{-1} are probably associated with the presence of N, as suggested by the existing literature [43], [45], [46].

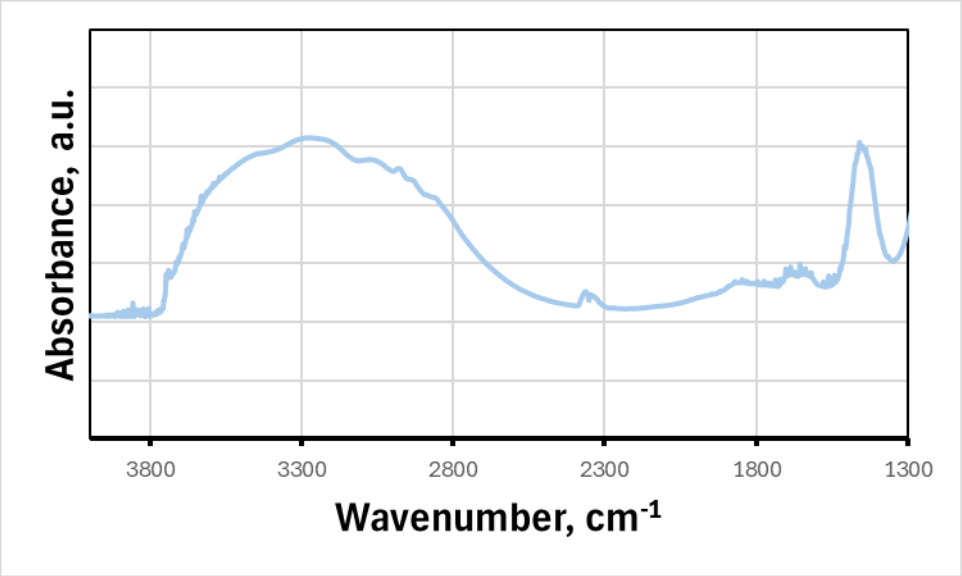

Figure 35: FTIR of AlSi_H_2O_prima2.

3.7.2 TGA

Figure 36 depicts a noticeable decline in the weight of the AlSi_H2O_prima aerogel samples with rising temperatures. Specifically, up to 150°C, there is a reduction in mass by 7.7% for the aerogels. Subsequently, within the temperature span from 150°C to 800°C, the loss in mass reaches approximately 13.9 %. Also, in this case, a notable enhancement with respect to the original AlSi synthesis was obtained. The new approach involved promoting the hydrolysis of the precursors earlier on, so resulting in a decrease in the organic content, as had already been discussed. It is interesting to observe that the mass rises at the end of the test. This is an artefact due to a buoyancy effect (artefact is observed for all samples).

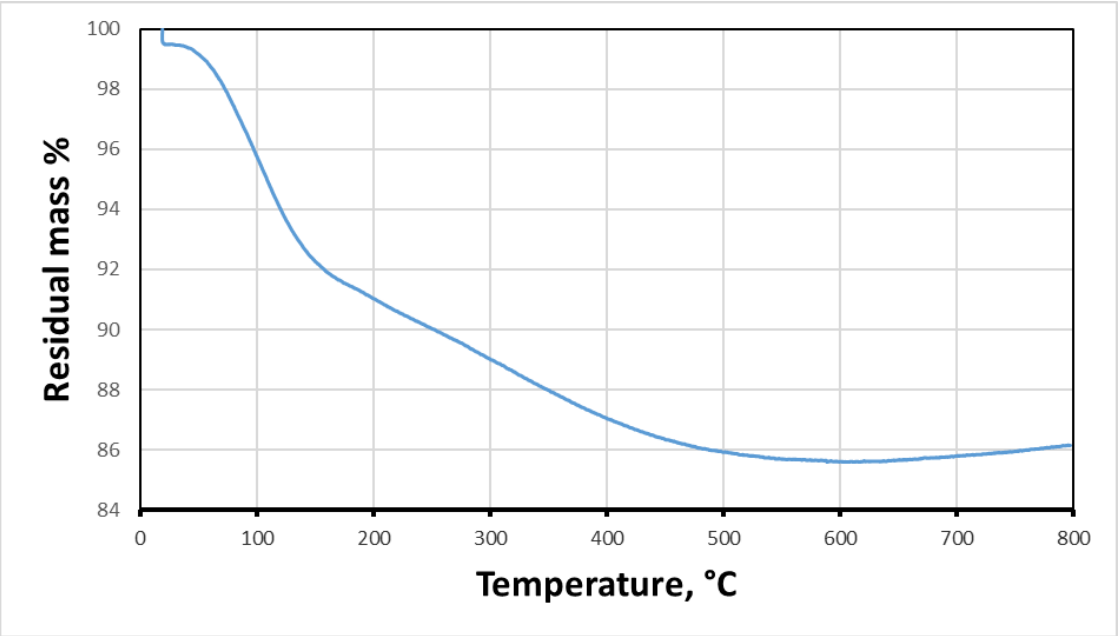

Figure 36: TGA of AlSi_H_2O_prima2.

To conclude, an alumina-silica aerogel was successfully synthesized, albeit with residual organic compounds likely stemming from incomplete precursor hydrolysis. To address this, exploratory syntheses were conducted, altering the timing of water addition during synthesis. This adjustment resulted in a reduction of organic content in the final samples. However, it was observed that this second series of samples exhibited increased fragility.

Subsequently, to test and compare the functionalized aerogels, the initial AlSi samples were kept as a reference. This decision was partly influenced also by the uncertainty about the impact of the organic content on the adsorption performance of CO_2. Therefore, despite the successful reduction in the organic content, the original AlSi samples remained the preferred choice for the subsequent experimentation.

Chapter 4

Alumina-silica aerogels functionalized with amino groups

4.1 Introduction

Once the process for the realization of the alumina-silica aerogel has been optimized, it is necessary to identify a suitable synthesis step for the introduction of the amino groups.

When chemical interactions occur, amine-functionalized compounds form covalent bonds with solid supports, resulting in what is referred to as a 'Class II' sorbent. Among the various types of amino silanes, tri amine-grafted silica exhibits the highest CO_2 uptake due to its elevated nitrogen concentration. However, this increased uptake potential can also lead to potential issues such as pore blockage, which are attributed to the larger molecular size of the tri-amine-grafted silica. The most used bonding agent for modifying silica surfaces is (3-Aminopropyl) triethoxysilane ($C_9H_{23}NO_3Si$), also called APTES (***Figure 37***) [56].

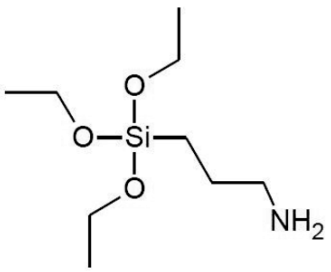

Figure 37: APTES molecule.

In the present work, the amino groups are introduced directly during the sol-gel synthesis and not with a subsequent treatment, to avoid further time and resource-consuming steps. APTES is chosen because it is a molecule suitable for this purpose, as shown in the literature [6].

In the sol-gel synthesis, the presence of water is fundamental because it hydrolyses the APTES. This compound has four branches: three contain alkyl chains, and one ends with an amino group. In the presence of the water, each alkyl chain is detached and becomes an alcohol while the oxygen molecule of APTES, which remains bound to the silicon, becomes an -OH (the hydrogen comes from water). This step is fundamental because the newly-formed -OH group of the APTES can then condense with the -OH of the silica or alumina matrix and therefore form a covalent bond

with the solid support. Since each molecule of APTES has three molecules of oxygen, three moles of water are theoretically needed for each mole of APTES to achieve its complete hydrolysation.

As it has just been explained, to guarantee the formation of covalent bonds between the alumina-silica network and APTES, this must be hydrolysed. Solution A already contains some H_2O (deriving from the HCl solution) which, however, serves to hydrolyse the TMOS. Consequently, H_2O was added to the synthesis to ensure the hydrolysis of APTES. Similar to the work by Shao [6], in which to obtain a silica aerogel functionalized with amines (with a one-pot co-condensation technique) they hydrolysed APTES and added TMOS, the same path was chosen for the first synthesis. In Shao's work [6], they started by solubilizing the APTES with H_2O and then added the silica precursor to obtain gelation, so initially we thought of adding the APTES to solution A which is the one containing H_2O (deriving from the HCl solution), which is left stirring for longer and contains the less reactive precursor (TMOS) (the alumina precursor is quite reactive, so it's best not to mix it with anything). By doing so, however, we obtained the gelatine of solution A before being able to add solution B and so we decided to change the order of the added reagents for the other aerogels.

After the first unsuccessful trial previously described, it was attempted a second approach in which solutions A and B were first prepared as explained in *paragraph 3.2* while APTES and H_2O were added only after A and B had been mixed. For conciseness, only the second synthesis procedure (where APTES is added after mixing solutions A and B) is described in the subsequent paragraphs.

4.2 Preparation of AlSi – APTES

4.2.1 Gel synthesis

Table 14: Mass quantities for the reagents in the solution A

Solution	2 – butanol	TMOS	HCl solution 0.01 M
Solution A	7.6975 g	3.0532 g	0.4531 g

Table 15: Mass quantities for the reagents in the solution B

Solution	2 – butanol	ATSB
Solution B	2.1988 g	0.5620 g

Additional reagents:

- H_2O = 0.4343 g

- APTES = 0.3928 g

Table *16* shows the molar ratio between reagents of the AlSi – APTES aerogels defined in the function of TMOS + ATSB. It was chosen to work with an excess quantity of water to guarantee the hydrolysis of all the chemical species, considering that the moles of water required to hydrolyse one mole of the reagents are three for APTES, four for TMOS, and three in the case of ATSB.

Table 16: Molar ratio between reagents of AlSi - APTES

Sample	ATSB	TMOS	TMOS + ATSB	Ammonia Solution 1.0 M	HCl solution 0.01 M	2 – butanol	APTES	H_2O^*
AlSi - APTES	0.1	0.9	1	8	0.9	6	0.11	10

*This value represents the sum of moles of the water in ammonia solution, HCl solution, and of the water added together with APTES.

For the synthesis, cylindrical beakers of 25 mL (primarily for the preparation of solution B) and 100 mL (for solution A and the final solution A+B) were utilized. Subsequently, the beakers were covered with parafilm. A magnetic stirrer, "*IKA Werke*," was used for agitation. For heating, the solutions were placed in a thermostatic bath heated on the magnetic stirrer plate ("*AREX - Heating Magnetic Stirrer*") with a probe for temperature control ("*VTF - Digital Thermoregulator*").

Solution A (mixed for 1h30 at room temperature at around 200 rpm) and solution B (mixed for 5 minutes at room temperature at around 200 rpm) were separately prepared and then mixed. After APTES and H_2O were immediately added. Then the system was heated up to 80 °C under magnetic stirring. Theoretically, the solution should have been left at 80 °C for two hours to form the gel. Instead, as soon as the solutions A, B, H_2O, and APTES were mixed, and heated, rapid gelation was observed, which made it impossible to add the basic catalyst ammonia solution (***Figure 38***, ***Figure 39***).

Figure 38: Al – Si – APTES aerogel after rapid gelation.

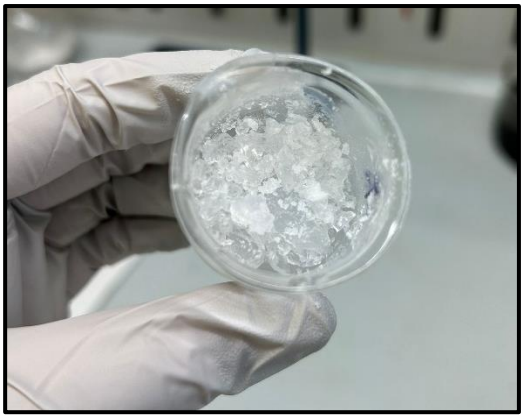

Figure 39: Al – Si – APTES aerogel after rapid gelation (focus on the structure).

To overcome this problem, the following sample was prepared without heating. It is assumed that the absence of heating would slow down the gelation kinetics and therefore allow enough time to add the last reagent (Ammonia solution).

4.3 Preparation of AlSi – APTES (2.5 mmol)

4.3.1 Gel synthesis

For experimental practical reasons, in this synthesis, the quantities of the reagents are rescaled with respect to those of the previous synthesis, but the molar ratios have been kept the same (

Table* 17**, ***Table 18).

Table 17: Mass quantities of the reagents of solution A

Solution	2 – butanol	TMOS	HCl solution 0.01 M
Solution A	11.5484 g	4.5729 g	0.6266 g

Table 18: Mass quantities of the reagents of the solution B

Solution	2 – butanol	ATSB
Solution B	3.3044 g	0.8680 g

Additional reagents:

- H_2O = 0.5649 g

- APTES = 0.5656 g
- Ammonia solution (1.0 M) = 4.8116 g

During the synthesis, 2.5 mmol of APTES are arbitrarily introduced (compared to 30 mmol of TMOS) and for this reason, the sample is identified with the name AlSi – APTES (2.5 mmol).

Table 19 presents the molar ratio between reagents of AlSi – APTES (2.5 mmol) as a function of TMOS + ATSB. It was chosen to work with an excess quantity of water to guarantee the hydrolysis of all the chemical species.

Table 19: Molar ratio between reagents of AlSi - APTES (2.5 mmol)

Sample	ATSB	TMOS	TMOS + ATSB	Ammonia Solution 1.0 M	HCl solution 0.01 M	2 – butanol	APTES	H_2O^*
AlSi – APTES (2.5 mmol)	0.1	0.9	1	8	0.9	6	0.075	10

*This value represents the sum of moles of the water in ammonia solution, HCl solution, and of the water added together with APTES.

For the synthesis, cylindrical beakers of 25 mL (primarily for the preparation of solution B) and 100 mL (for solution A and the final solution A+B) were utilized. Subsequently, the beakers were covered with parafilm. A magnetic stirrer, "*IKA Werke*," was used for agitation.

First, solution A was prepared and mixed (at approximately 200 rpm) at room temperature for 1h30. Then, solution B was prepared and mixed (at approximately 200 rpm) at room temperature for 5 minutes. Then, A and B were combined and, by keeping constant stirring, H_2O and APTES were added at room temperature. The solution was mixed for 1h (200 rpm, T amb), then, after the addition of ammonia solution and a further 2-minute mixing time, it was poured into cylindrical glass samples and left to gel at ambient temperature. Gelation occurred in 1h30. Finally, the gel was covered with ethanol and left to age for seven days before drying in supercritical CO_2 (***Figure 40***).

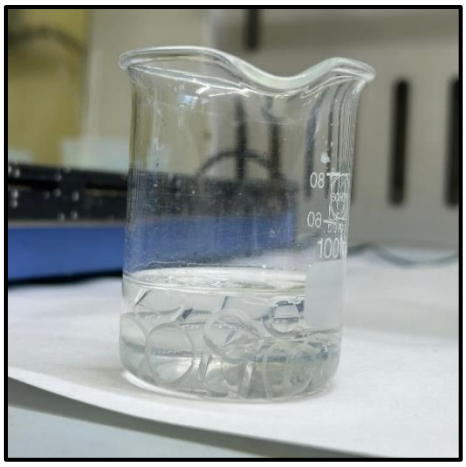

Figure 40: AlSi – APTES (2.5 mmol) aerogel of the second attempt.

4.3.2 Supercritical drying process

The gels underwent supercritical drying with carbon dioxide in an autoclave (40 mL stainless steel vessel with an internal diameter of 14 mm) for 90 minutes (105 bar and 40 °C), where the samples were separated with propylene wool. The formed aerogels underwent a volume shrinkage (***Figure 41***, ***Figure 42***).

Figure 41: Focus on the volume shrinkage.

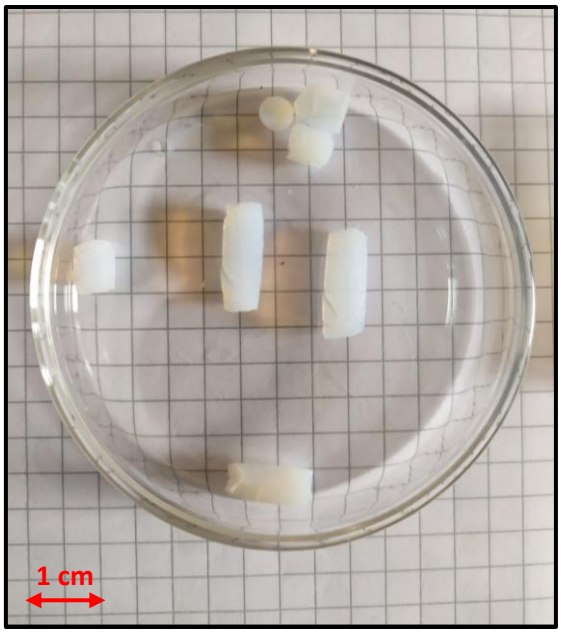

Figure 42: Samples after the supercritical drying.

A precision balance was employed for weighing with a single measurement (one measurement of diameter and one of the length were conducted). It was assumed that the aerogel would retain a cylindrical shape corresponding to the geometry of the moulds.

Table 20 shows the dimensions, density, and volume shrinkage of the different samples. The diameters of the glass cylinders are 7 mm and 10.8 mm. The volumetric shrinkage was calculated starting from the shrinkage of the diameter and length. The shrinkage of the diameter was calculated by measuring the initial and final diameter, while for the shrinkage of the length (since the initial length of the samples is unknown) it was assumed that it is equal in percentage to that of the diameter.

Table 20: Dimensions, density, and volume shrinkage of AlSi - APTES (2.5 mmol) aerogel

Internal diameter, cm	h, cm	Final volume, cm^3	Starting volume, cm^3	Volume shrinkage, cm^3	Weight, g	Apparent density, g/cm^3
0.55	1.37	0.325	0.670	0.345	0.0753	0.23
0.50	1.40	0.275	0.754	0.479	0.0783	0.28
0.48	1.05	0.190	0.590	0.400	0.0639	0.34
0.46	1.63	0.270	0.954	0.684	0.1022	0.38
0.53	0.65	0.143	0.330	0.187	0.0333	0.23
0.50	0.48	0.094	0.258	0.164	0.0301	0.32

4.3.3 Reproduction

The synthesis of the AlSi-APTES (2.5 mmol) aerogels has been repeated to verify the reproducibility of our results. The quantities used for the synthesis are reported in ***Table 21*** and ***Table 22***.

Table 21: Mass quantities of the reagents of solution A

Solution	2 – butanol	TMOS	HCl solution 0.01 M
Solution A	5.7760 g	2.3094 g	0.3573 g

Table 22: Mass quantities of the reagents of solution B

Solution	2 – butanol	ATSB
Solution B	1.6542 g	0.4328 g

Additional reagents:

- H_2O = 0.2969 g
- APTES = 0.3203 g
- Ammonia solution (1.0 M) = 2.4197 g

The gel obtained after the synthesis is shown in ***Figure 43***. "*AlSi-APTES (2.5 mmol)_R*" is the name of the sample, where "R" means "reproduction". This nomenclature will be used for all the samples that have been reproduced.

Figure 43: Gel of AlSi-APTES (2.5 mmol)_R.

After the supercritical drying, the aerogels appear fragile and opaque (***Figure 44***).

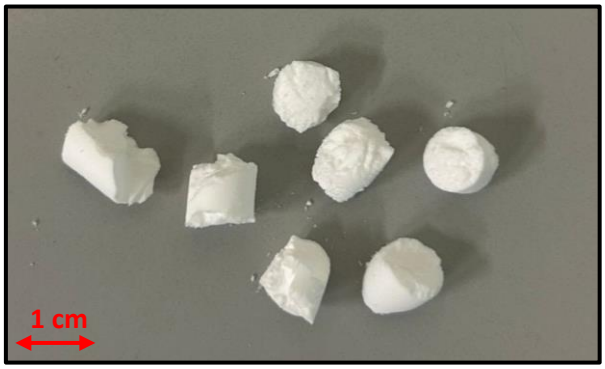

Figure 44: AlSi - APTES (2.5 mmol)_R aerogels.

A precision balance was employed for weighing with a single measurement (one measurement of diameter and one of the length were conducted). It was assumed that the aerogel would retain a cylindrical shape corresponding to the geometry of the moulds.

Table 23 presents data on the dimensions, density, and volume shrinkage observed across various samples. The glass cylinders used in the experiment have diameters of 7 mm and 10.8 mm. The volumetric shrinkage was calculated starting from the shrinkage of the diameter and length. The shrinkage of the diameter was calculated by measuring the initial and final diameter, while for the shrinkage of the length (since the initial length of the samples is unknown) it was assumed that it is equal in percentage to that of the diameter.

Table 23: Dimensions, density, and volume shrinkage of AlSi - APTES (2.5 mmol)_R aerogel.

Internal diameter, cm	h, cm	Final volume, cm^3	Starting volume, cm^3	Volume shrinkage, cm^3	Weight, g	Apparent density, g/cm^3
0.77	0.38	0.177	0.213	0.036	0.0099	0.06
0.63	0.57	0.178	0.403	0.225	0.0098	0.06
0.65	0.78	0.259	0.569	0.310	0.0143	0.06
0.68	0.65	0.236	0.496	0.260	0.0179	0.08
0.76	0.48	0.218	0.265	0.0470	0.0097	0.04

4.4 Characterization of AlSi – APTES (2.5 mol)

4.4.1 FTIR

The spectral region spanning from 3200 to 3700 cm^{-1} is associated with the presence of –OH. The signals observed at approximately 2900 cm^{-1} can be linked to -CH groups found in organic constituents. As reported in the existing literature, a signal related to Al-OH is identifiable around 1640 cm^{-1} [42], [43]. Peaks centred at 1600 cm^{-1} are indicative of the existence of amino groups [27], [28]. Additionally, the diverse peaks observed around 1400 cm^{-1} are likely linked to the organic components, as discussed in references [26] (***Figure 45***). Consistently with the addition of APTES during the synthesis, the presence of amino groups in the sample can be observed. The presence of organic components, however, can be attributable both to the alkyl chain of APTES and to the incomplete hydrolysis of the precursors, in agreement with what was observed for the AlSi reference sample.

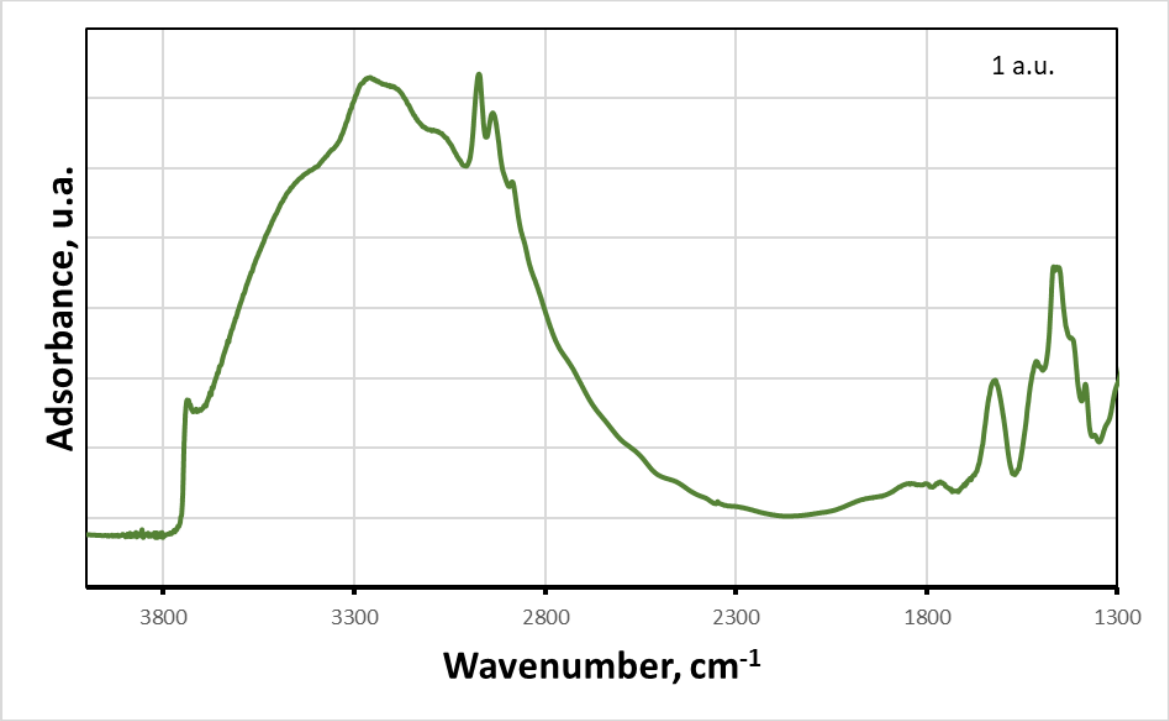

Figure 45: FTIR of AlSi – APTES (2.5 mmol) aerogel.

Figure 46 shows the FTIR of the reproduction. The observed trend of the curve, mirroring that depicted in ***Figure 45***, serves as an indicative validation that the sample reproduction test has effectively resulted in aerogels harbouring identical surface groups.

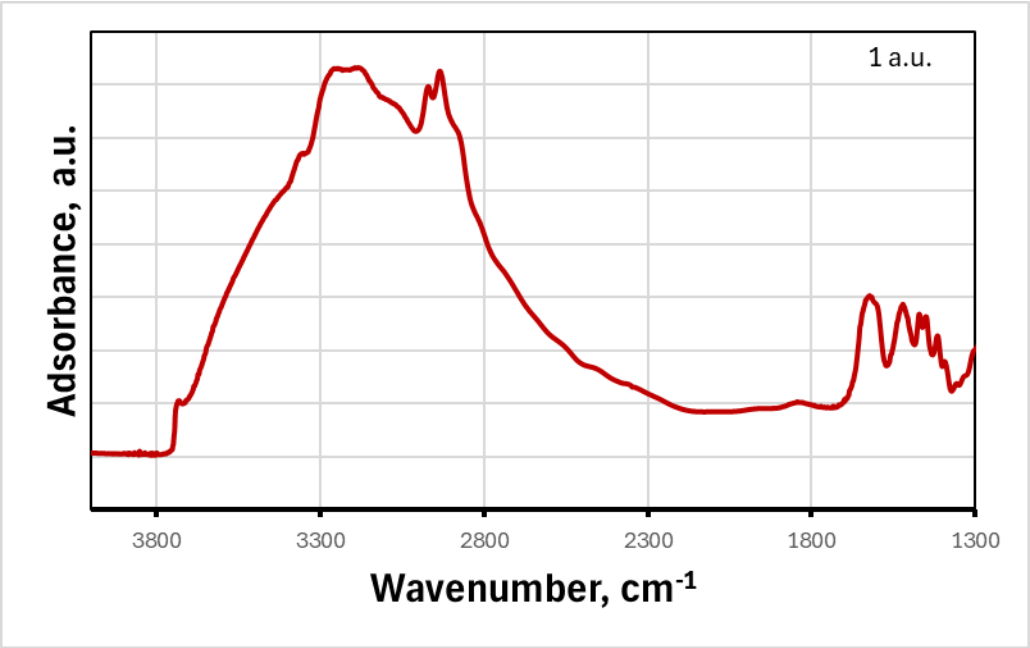

Figure 46: FTIR for AlSi - APTES (2.5 mmol) aerogels (reproduction)

4.4.2 TGA

AlSi – APTES (2.5 mmol) aerogels exhibit weight losses with the temperature rise (***Figure 47***). Before 150 °C, these samples experienced a mass loss of 10.2 % due to physiosorbed water. Between 150 °C and 800 °C, the degradation of organic components determined a mass loss of approximately 20.2 %. This value is attributable both to organic residues of precursors (also observed in AlSi) and to the amines introduced during the synthesis. Since these two contributions cannot be separated (as the degradation temperatures fall in the same range) it is not possible to deduce the mass content of amines from this measurement. Furthermore, it is noted that the mass loss is lower than that observed in the sample as such. This phenomenon could be justified by the fact that in the samples with APTES, the H_2O is added at least one hour before the gelation begins (with the addition of the basic catalyst), so it is likely that in these samples the hydrolysis of the precursors is greater and, therefore, there are fewer organic residues than those present in the AlSi sample (consistently with what was also observed under IR).

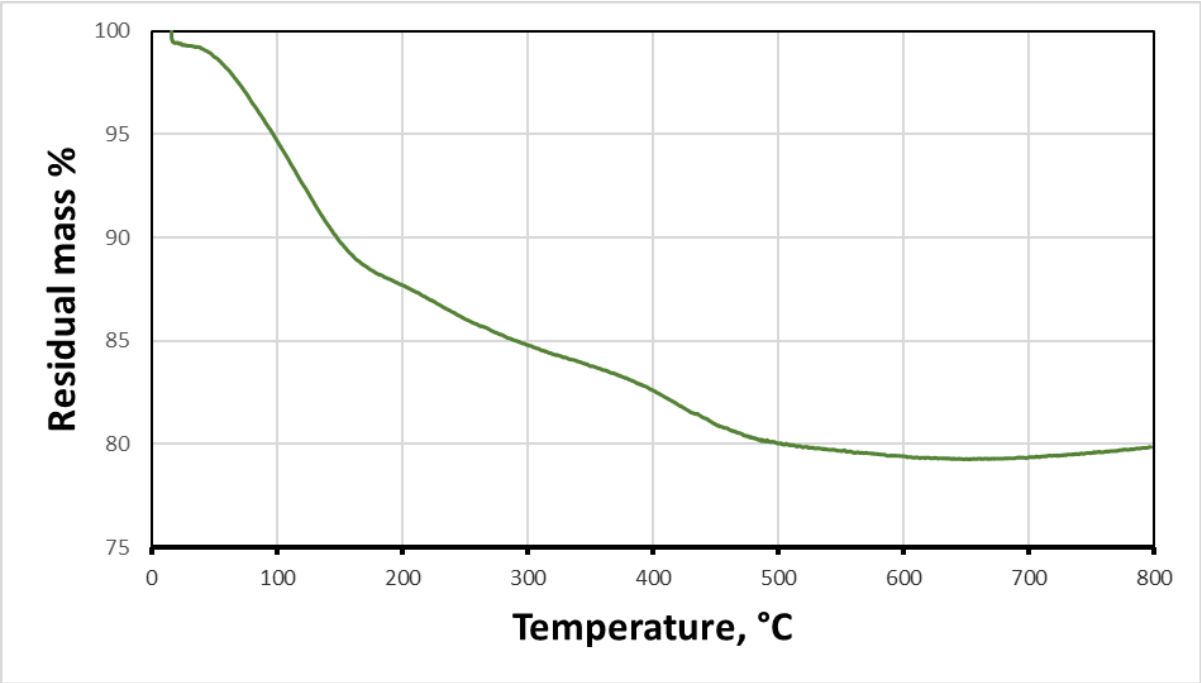

Figure 47: TGA of AlSi - APTES (2.5 mmol) aerogel.

Figure 49 shows the TGA for the reproduction of the AlSi – APTES (2.5 mmol) aerogels. Up to 150°C, the specimens underwent a decrease in mass by 10.4%, attributable to the removal of physiosorbed water. Subsequently, during the temperature range spanning from 150°C to 800°C, the decomposition of organic constituents led to a loss in mass of around 21.8%. The mass losses of this sample are comparable to those of the AlSi-APTES sample (2.5 mmol).

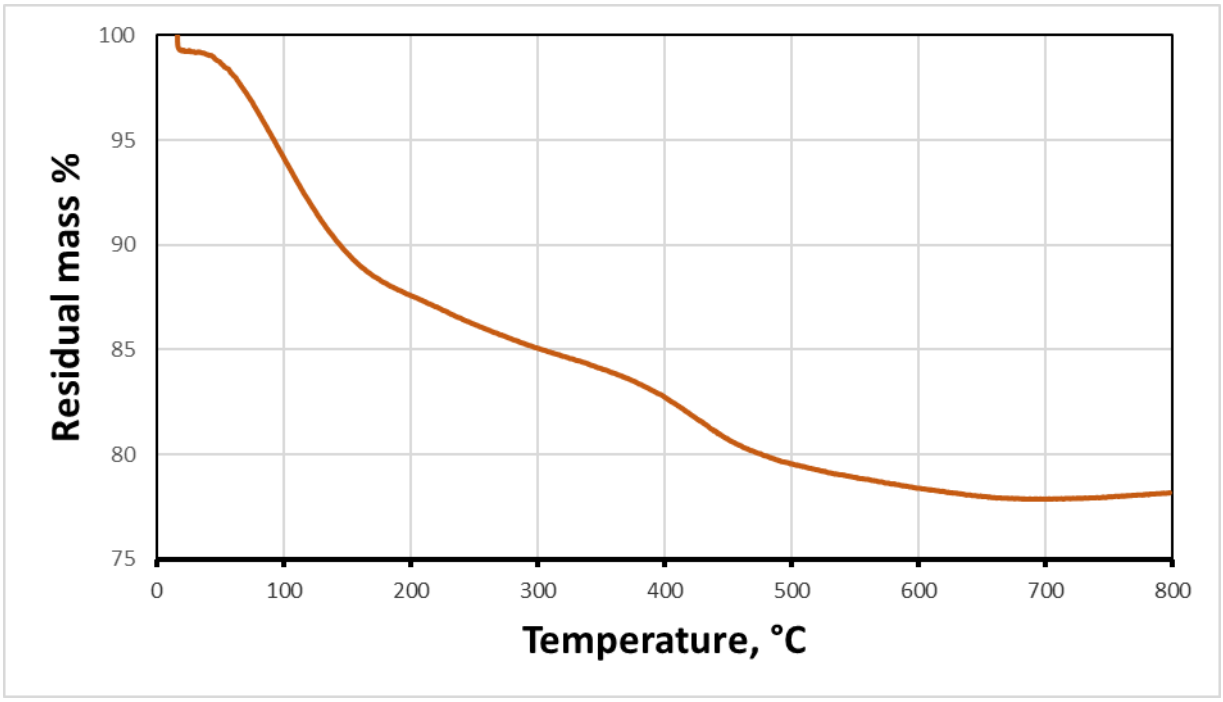

Figure 48: TGA for AlSi - APTES (2.5 mmol)_R aerogels.

It is interesting to observe that the mass rises at the end of the test. This is an artefact due to a buoyancy effect (artefact is observed for all samples).

4.4.3 X–ray diffraction

At high angles (***Figure 49***) the sample presents only an amorphous halo [32], [35], [36]

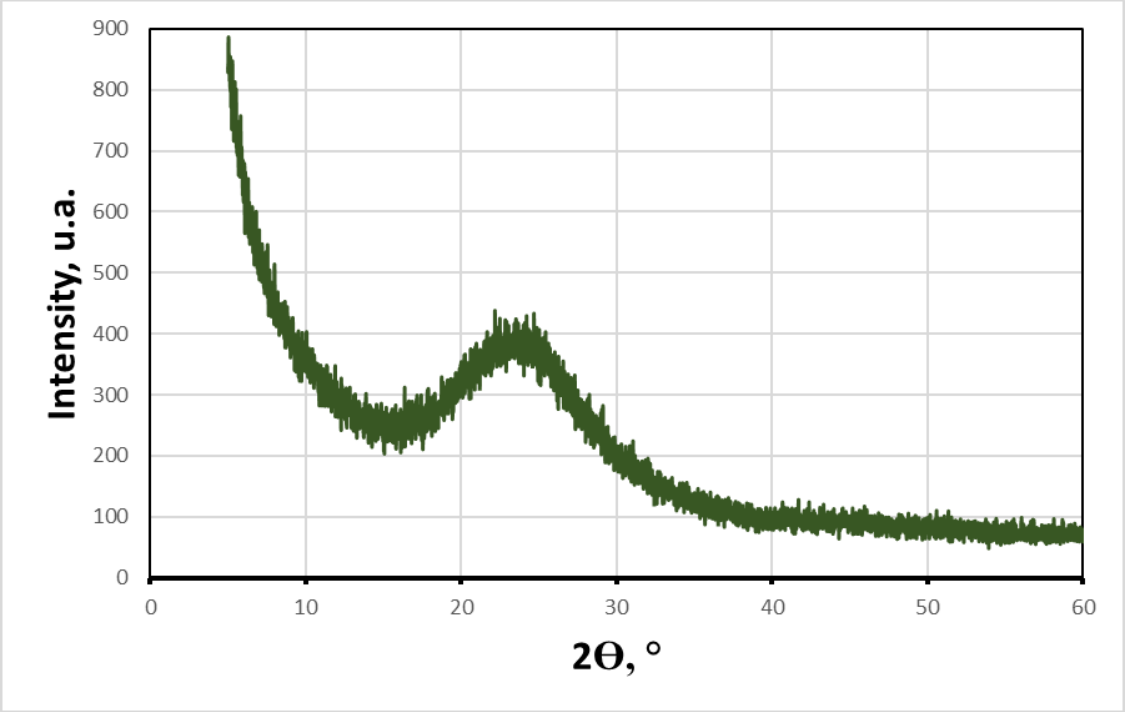

Figure 49: XRD at high angles of AlSi - APTES (2.5 mmol) aerogel.

AlSi – APTES (2.5 mmol) aerogels show no signs of ordered structures in the mesoporosity range (low angles) [31], [33], [48] (***Figure 50***).

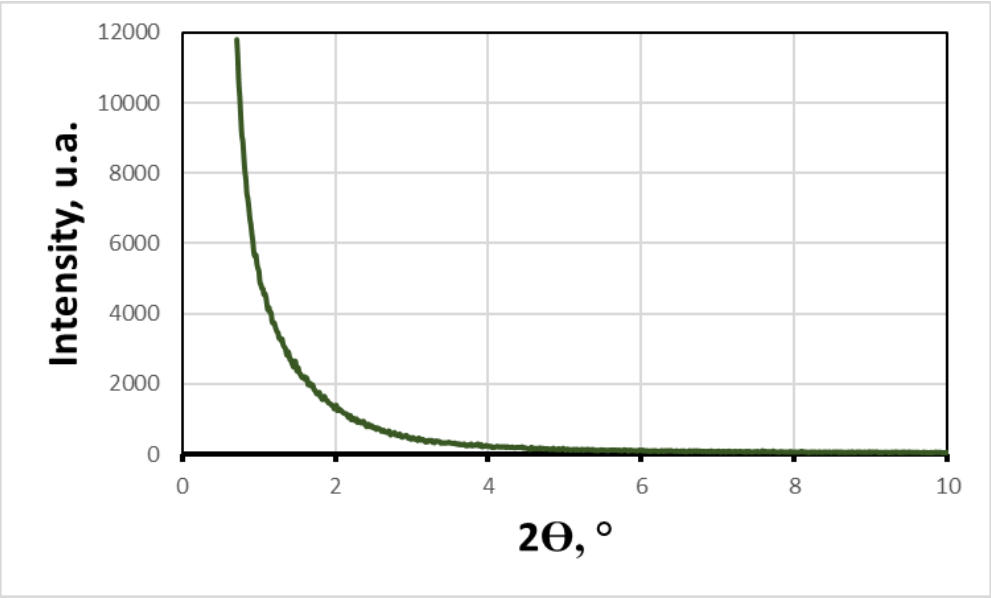

Figure 50: XRD at low angles of AlSi - APTES (2.5 mmol) aerogels.

4.4.4 N_2 adsorption

- Nitrogen adsorption isotherm

The determination of specific surface area follows the Brunauer–Emmett–Teller (BET) methodology. The classification assigned by IUPAC categorizes the curve as type IV, featuring a loop identified as H1. The specific surface area is 695 m^2/g. The porous value is 1.5 cm^3/g (***Figure 51***). These values are lower than those of the AlSi sample, but this is consistent with the fact that we add a species, APTES, which partly interferes with the formation of the siliceous network.

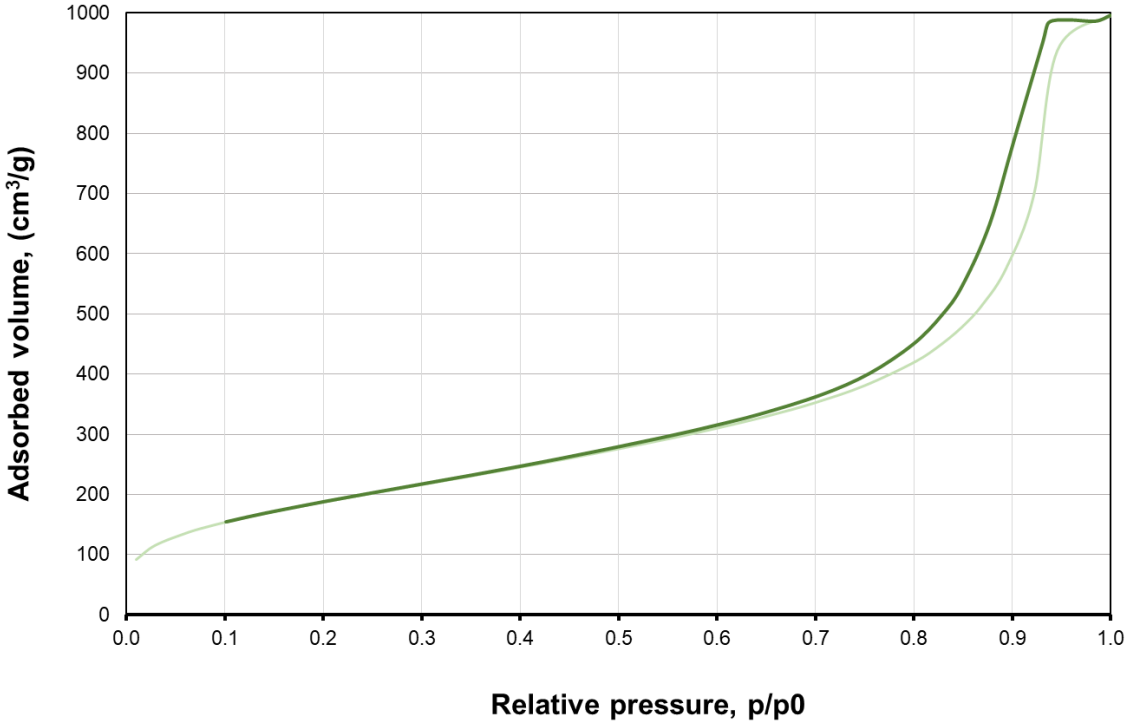

Figure 51: BET of AlSi - APTES (2.5 mmol) aerogel.

- BJH Graph

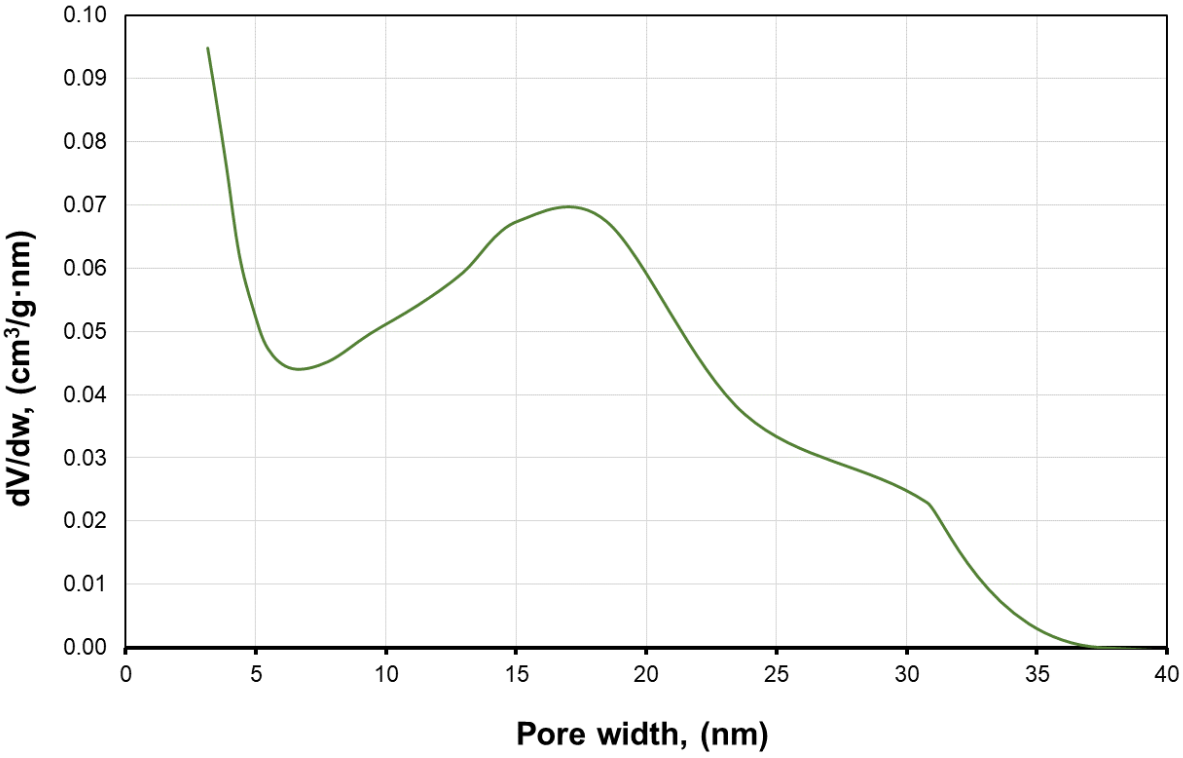

Figure 52: BJH of AlSi - APTES (2.5 mmol) aerogel.

Table 24 shows a sum of the textural properties of the AlSi – APTES (2.5 mmol) samples.

Table 24: Summary of the textural properties of the AlSi - APTES (2.5 mmol) aerogels

TEXTURAL PROPERTIES		
Specific surface area	Porous volume	Average pore diameter
695 m^2/g	1.5 cm^3/g	16 nm

Figure 53 and ***Figure 54*** show the BET and BJH of the AlSi-APTES (2.5 mmol)_R aerogels.

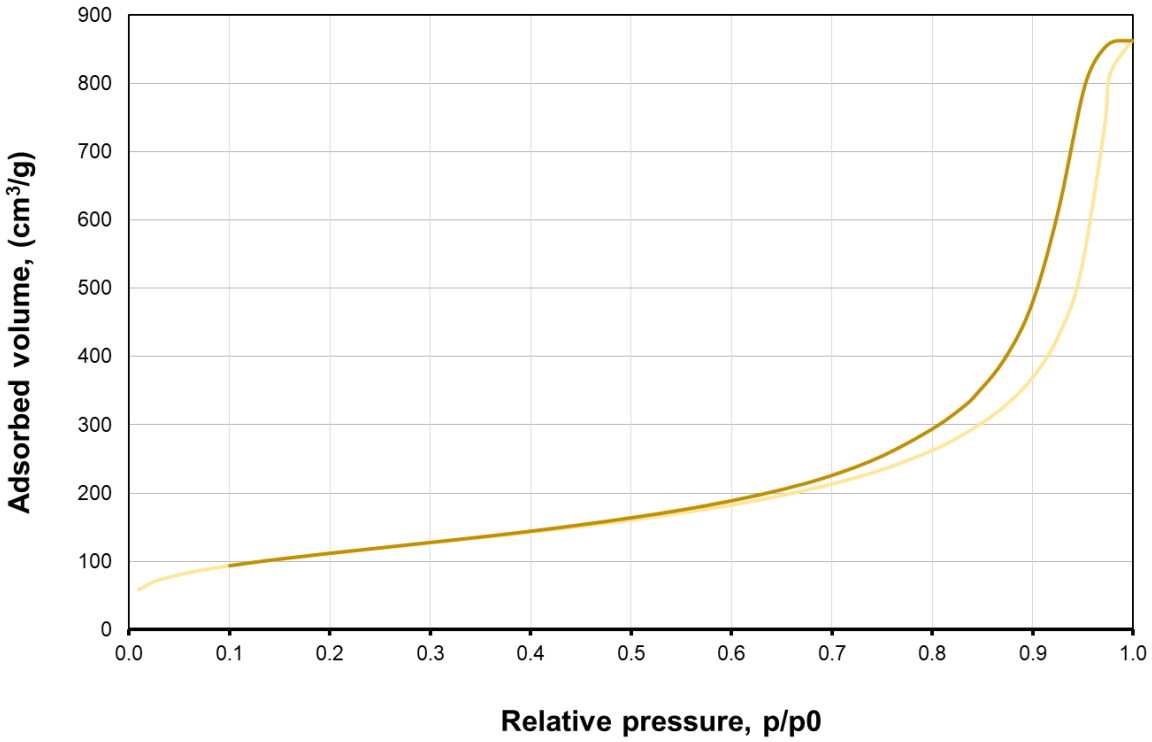

Figure 53: BET of AlSi-APTES (2.5 mmol)_R aerogels.

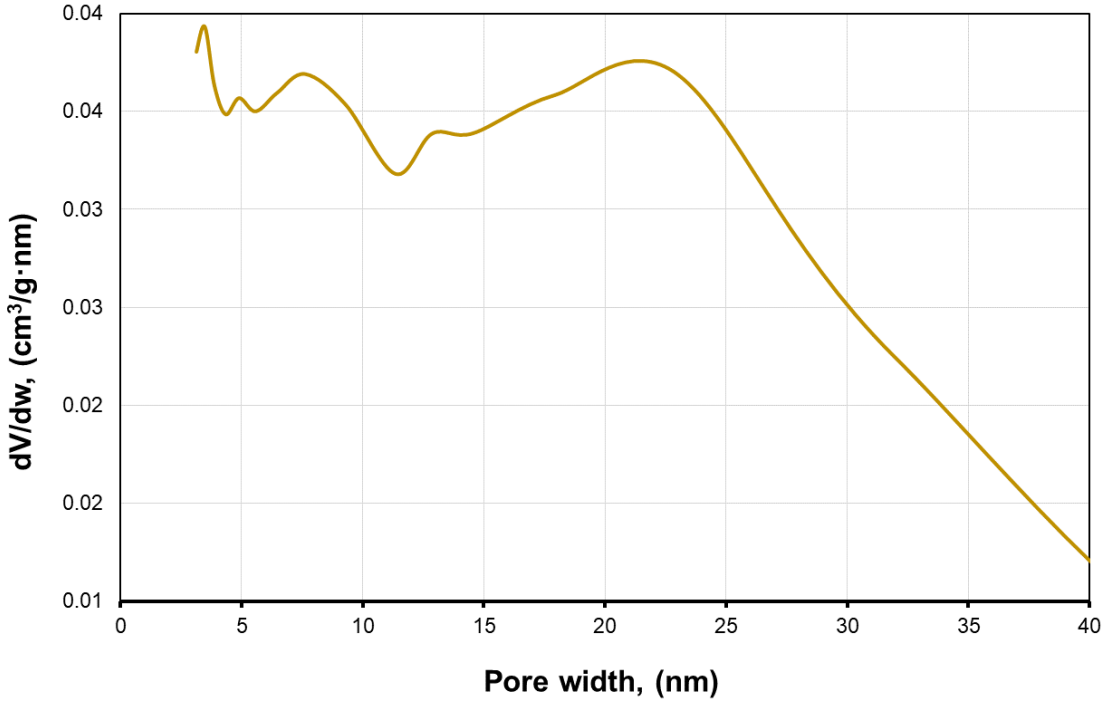

Figure 54: BJH of AlSi-APTES (2.5 mmol)_R aerogels.

Table 25 shows the textural properties of AlSi – APTES (2.5 mmol)_R aerogels.

Table 25: Textural properties of AlSi-APTES (2.5 mmol)_R aerogels.

TEXTURAL PROPERTIES		
Specific surface area	Porous volume	Average pore diameter
404 m^2/g	1.3 cm^3/g	21 nm

As it is possible to see, the results of nitrogen adsorption significantly differ from those of the first synthesis. It can be concluded that, although the sol-gel process allows the obtainment of samples comparable in terms of composition (FTIR, TGA) and crystalline structure (XRD), it cannot guarantee a significant reproducibility of the textural properties.

4.4.4.1 Xerogel analysis

The N_2 adsorption analysis has been carried out on the xerogel AlSi+APTES (2.5 mmol). The isotherms are type IV with H2b loop, i.e. they are mesoporous, but with a disordered porosity. The specific surface area is 830.3 m^2/g. The porous value is 1.05 cm^3/g (***Figure 55***). Surprisingly, the xerogels in this case have higher SSA and Vpor than the aerogel, perhaps because the volume shrinkage of the aerogels during the drying phase was significant. However, it is noted that the

average size of the pores is significantly higher in the aerogels, indicating that the porous structure of the gel is preserved more with the $scCO_2$ drying.

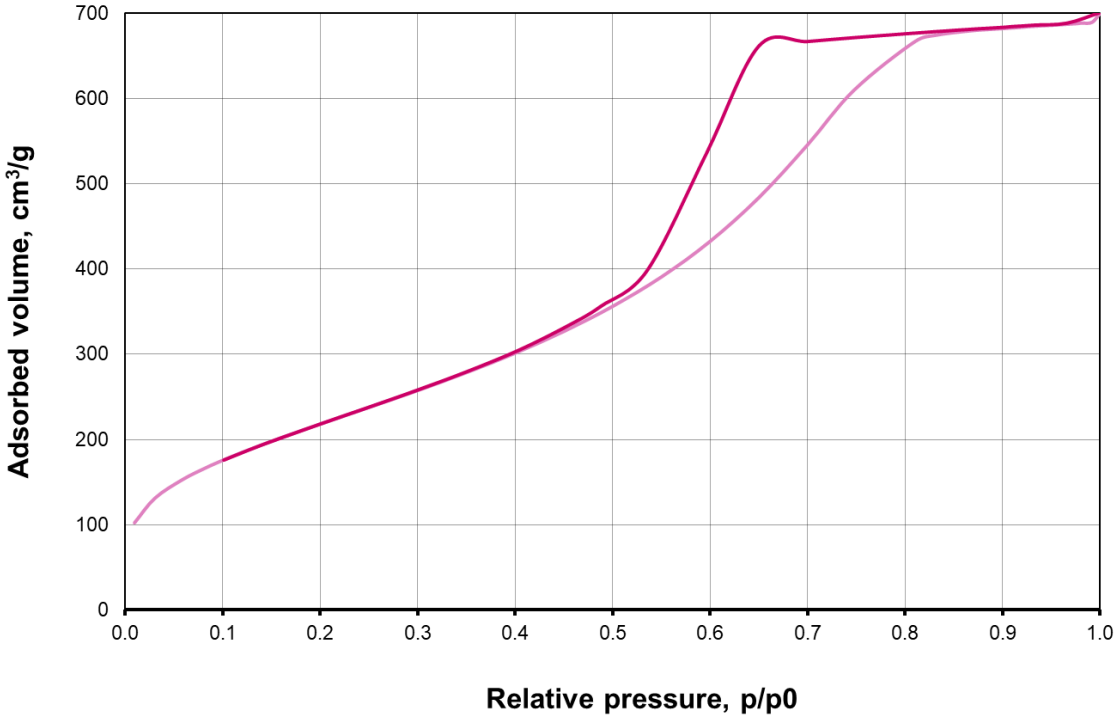

Figure 55: BET of xerogel AlSi+APTES (2.5 mmol)

According to ***Figure 56***, the distribution is single-mode, rather narrow, and with a maximum of approximately 5.6 nm.

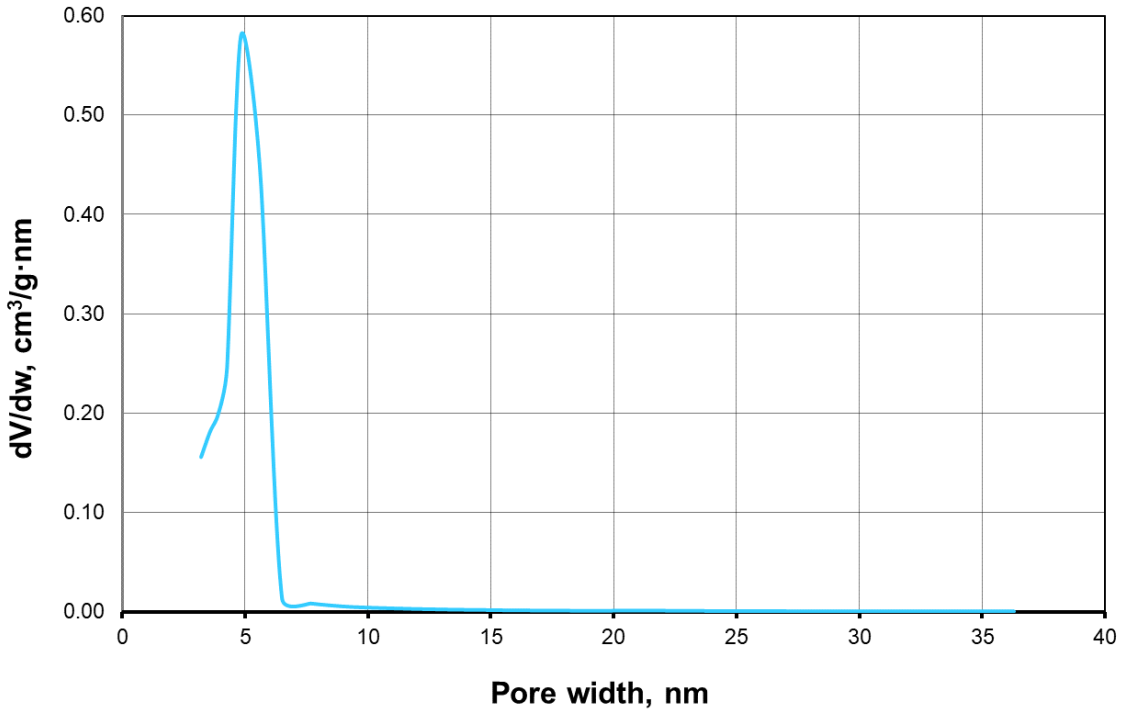

Figure 56: BJH of xerogel AlSi+APTES (2.5 mmol)

Table 26 shows a sum of the textural properties of the AlSi – APTES (2.5 mmol) xerogels.

Table 26: Summary of the textural properties of the AlSi - APTES (2.5 mmol) xerogels

TEXTURAL PROPERTIES		
Specific surface area	Porous volume	Average pore diameter
830.3 m^2/g	1.05 cm^3/g	5 nm

Nitrogen adsorption analysis on the xerogel was repeated and led to similar results (***Figure 57***, ***Figure 58***).

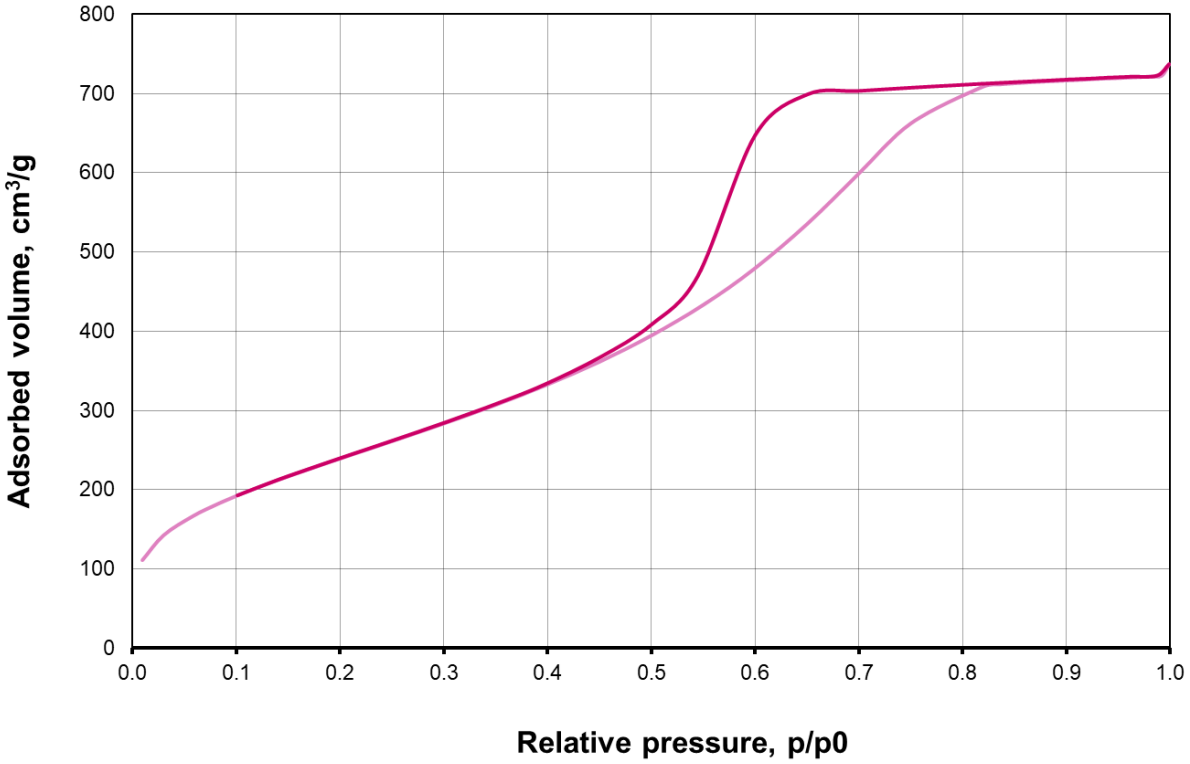

Figure 57: BET of AlSi-APTES (2.5 mmol)_R xerogels.

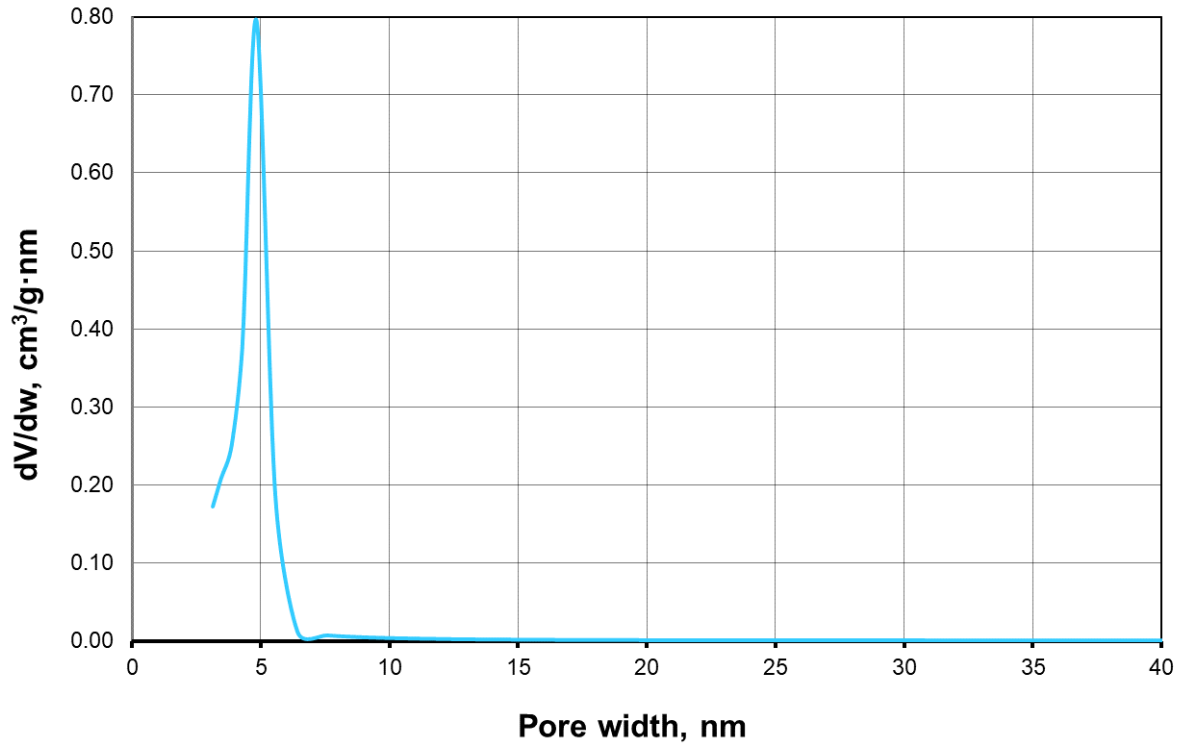

Figure 58: BJH of AlSi-APTES (2.5 mmol)_R xerogels.

Table 27 shows the textural properties of the AlSi-APTES (2.5 mmol)_R xerogels.

Table 27: Textural properties of AlSi-APTES (2.5 mmol)_R xerogels.

TEXTURAL PROPERTIES		
Specific surface area	Porous volume	Average pore diameter
916.7 m^2/g	1.12 cm^3/g	4 nm

4.4.5 XPS

In this section, a survey spectrum and high-resolution spectra focusing on individual elements are presented (***Figure 59, Figure 60, Figure 61, Figure 62, Figure 63***).

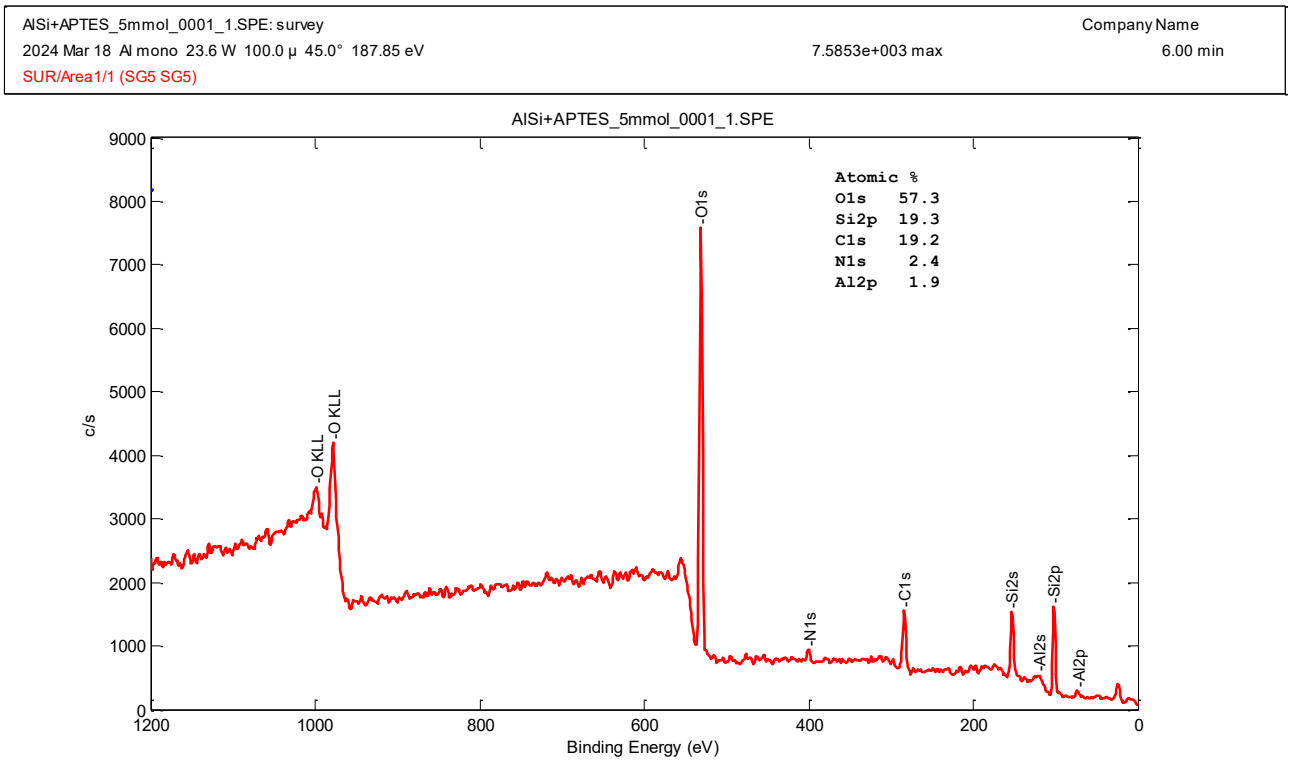

Figure 59: Survey spectrum of AlSi+APTES (2.5 mmol) sample*

In ***Figure 60***, the peak of Carbon is at 285 eV [53]

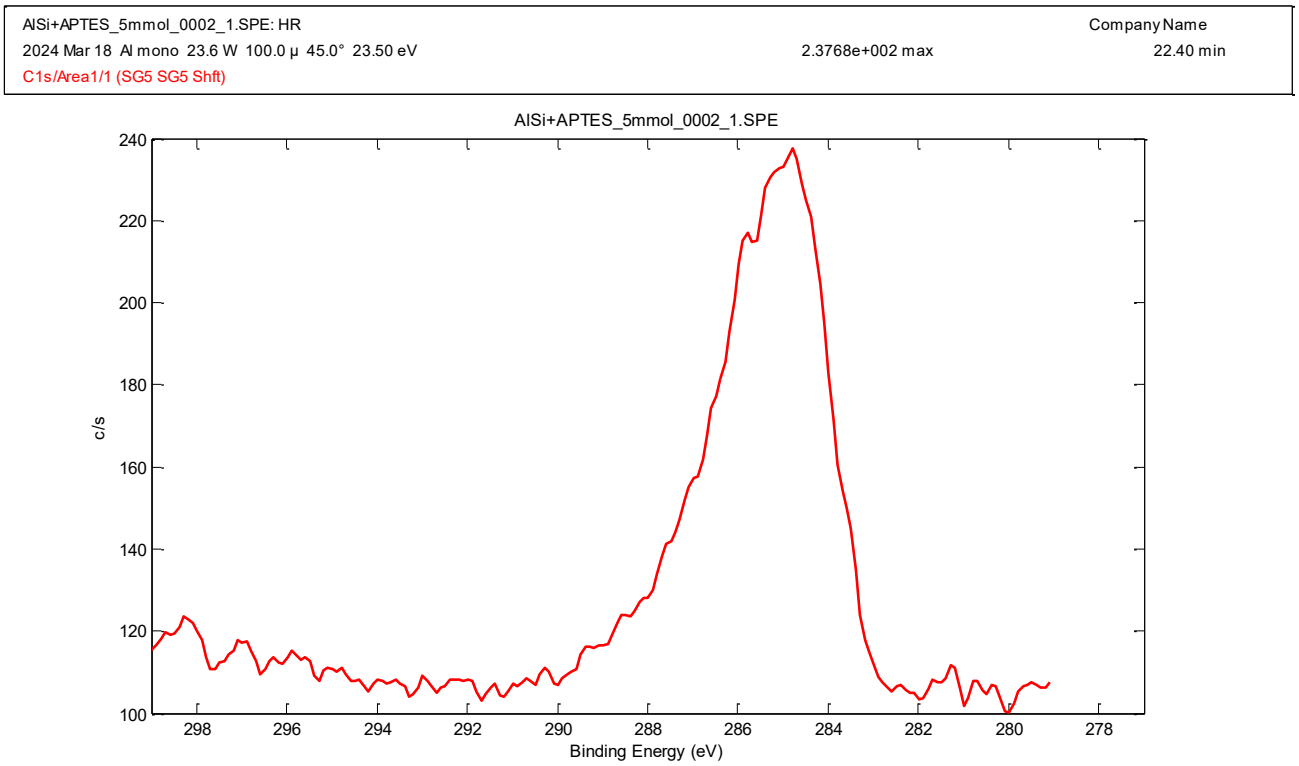

Figure 60: high-resolution spectra of C in AlSi+APTES (2.5 mmol) sample*

In ***Figure 61***, Oxygen is shown through the peak at 532 eV.

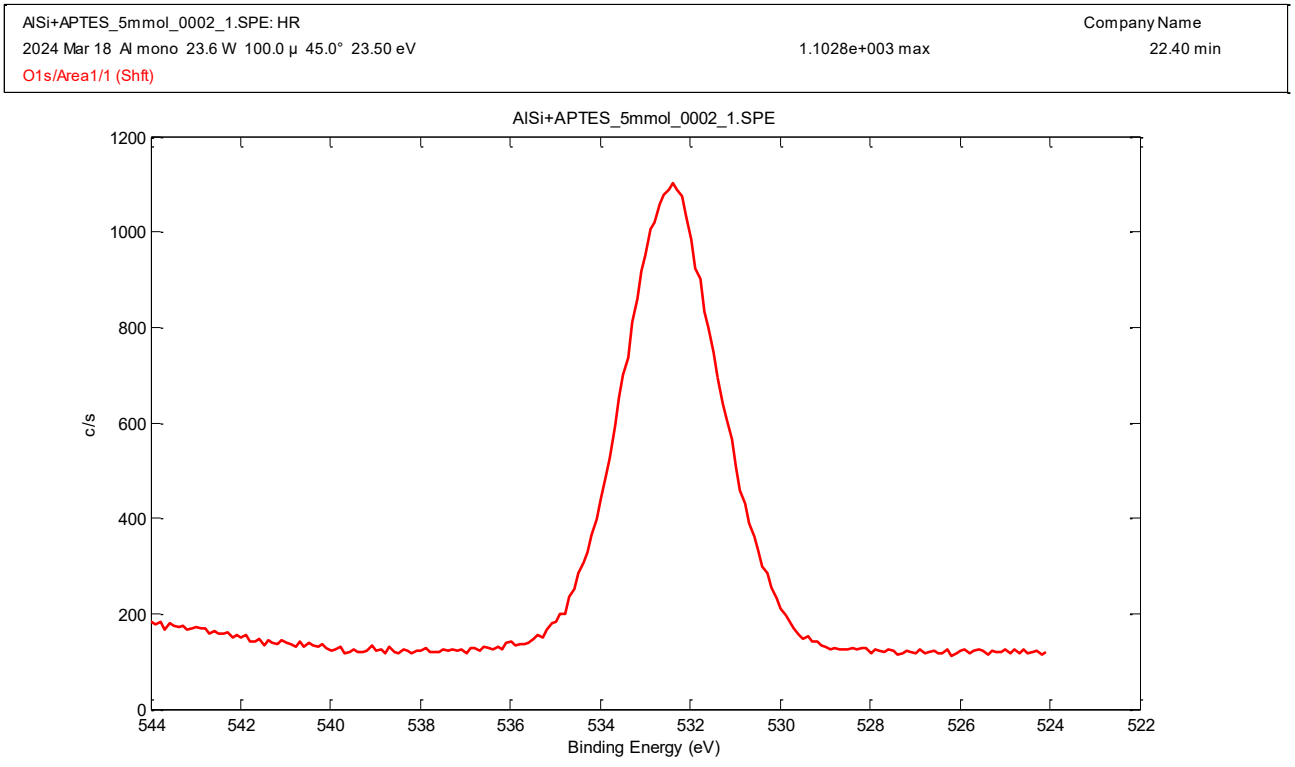

Figure 61: high-resolution spectra of O in AlSi+APTES (2.5 mmol) sample*

The peak of protonated nitrogen at 402 eV is present in ***Figure 62*** [54].

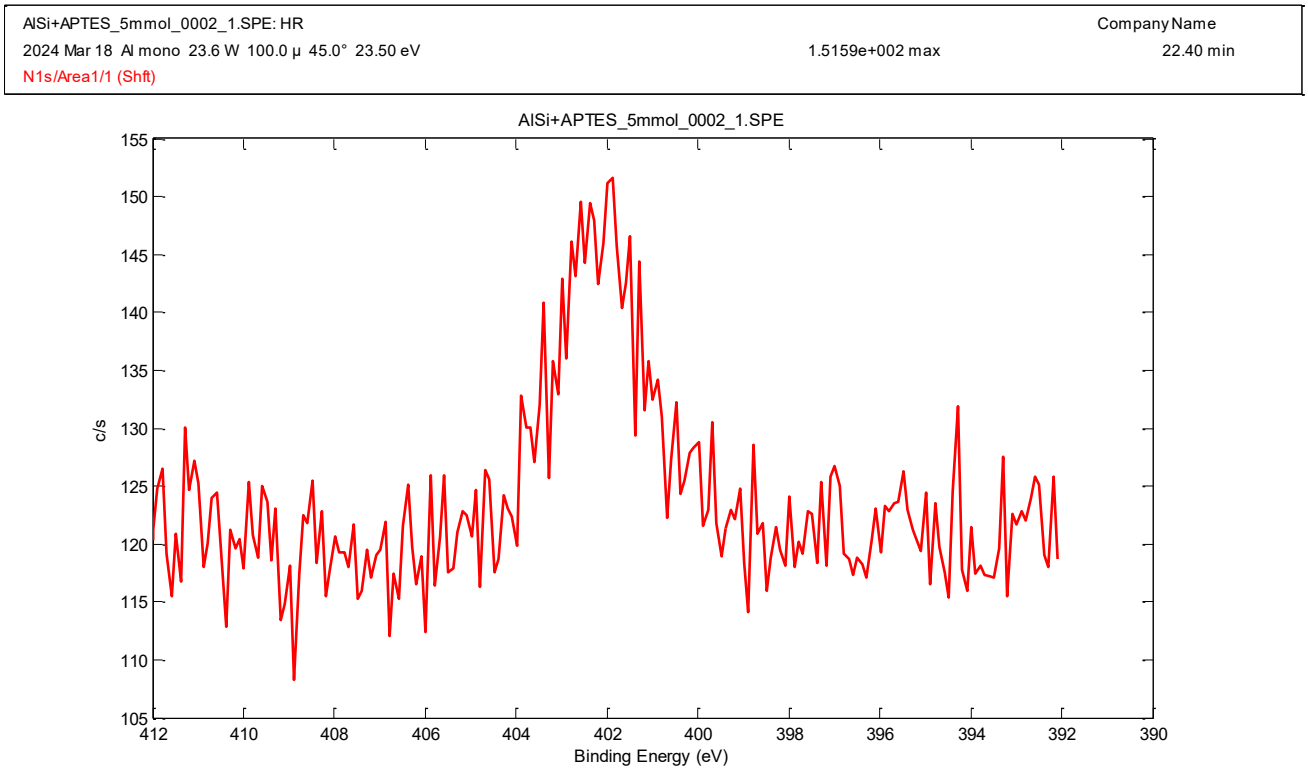

Figure 62: high-resolution spectra of N in AlSi+APTES (2.5 mmol) sample*

In ***Figure 63***, the peak at 74 eV indicates the presence of Aluminium [57].

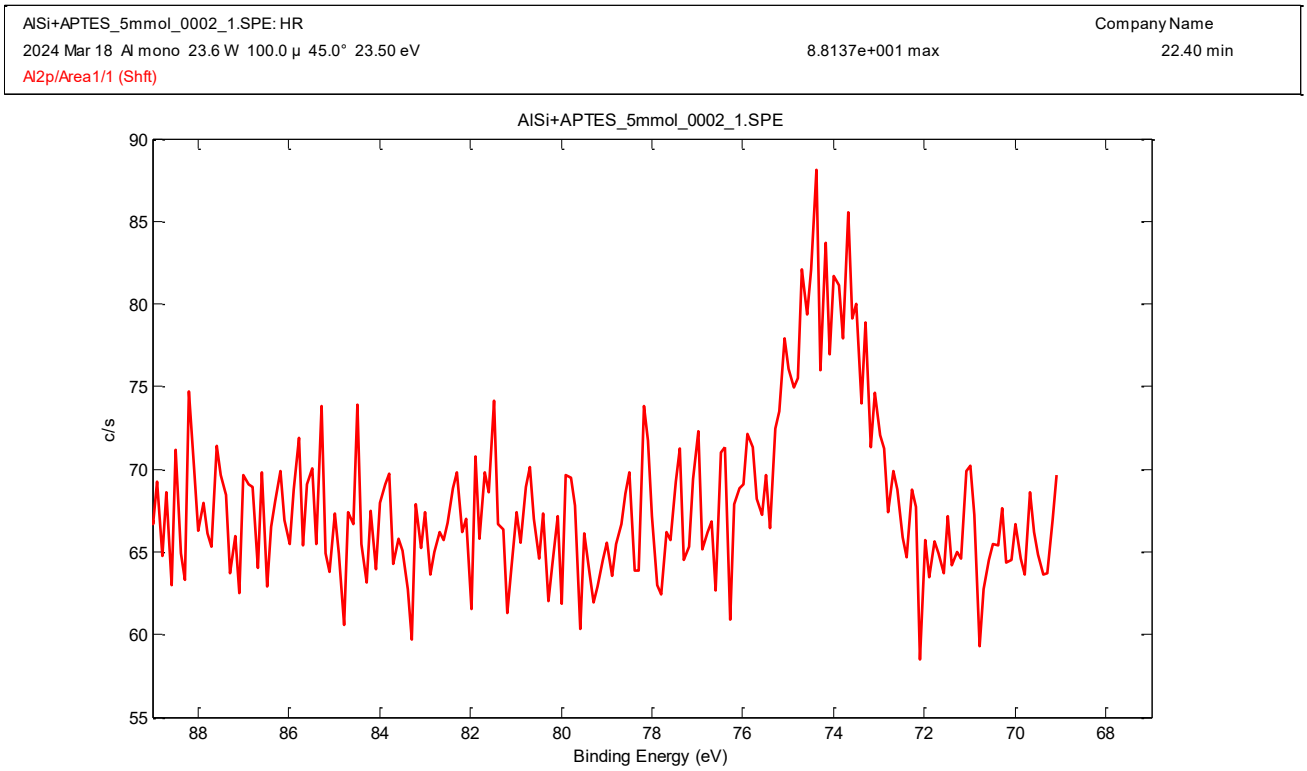

Figure 63: high-resolution spectra of Al in AlSi+APTES (2.5 mmol) sample*

*Please take into consideration that in graphs there is the indication "AlSi+APTES (5 mmol)" that is referred to the sample "AlSi+APTES (2.5 mmol)".

4.5 Preparation of AlSi – APTES (7.5 mmol)

4.5.1 Gel synthesis

Another attempt was made by tripling the number of APTES moles and, consequently, also by modifying the quantity of water.

Table 28: Mass quantities of the reagents of the solution A

Solution	2 – butanol	TMOS	HCl solution 0.01 M
Solution A	11.5368 g	4.5693 g	0.6152 g

Table 29: Mass reagents of the solution B

Solution	2 – butanol	ATSB
Solution B	3.2933 g	0.8483 g

Additional reagents:

- H_2O = 0.8535 g
- APTES = 1.6752 g
- Ammonia solution (1.0 M) = 4.8263 g

Table *30* shows the molar ratio of reagents of AlSi – APTES (7.5 mmol) in the function of TMOS + ATSB. It was chosen to work with an excess quantity of water to guarantee the hydrolysis of all the chemical species.

Table 30: Molar ratio of reagents of AlSi - APTES (7.5 mmol)

Sample	ATSB	TMOS	TMOS + ATSB	Ammonia Solution 1.0 M	HCl solution 0.01 M	2 – butanol	APTES	H_2O^*
AlSi – APTES (7.5 mmol)	0.1	0.9	1	8	0.9	6	0.23	10.5

*This value represents the sum of moles of the water in ammonia solution, HCl solution, and of the water added together with APTES.

The preparation procedure is the same as that of sample *AlSi – APTES (2.5 mmol)*, which is reported in *paragraph 4.3.1* (here only the quantity of APTES and water are changed) (***Figure 64***).

Figure 64: Gel of AlSi - APTES (7.5 mmol)

4.5.2 Supercritical drying

The gels underwent supercritical drying with carbon dioxide in an autoclave (40 mL stainless steel vessel with an internal diameter of 14 mm) for 90 minutes (105 bar and 40 °C), where samples were separated with Teflon spacers. The formed aerogels underwent a volume shrinkage (***Figure 65***).

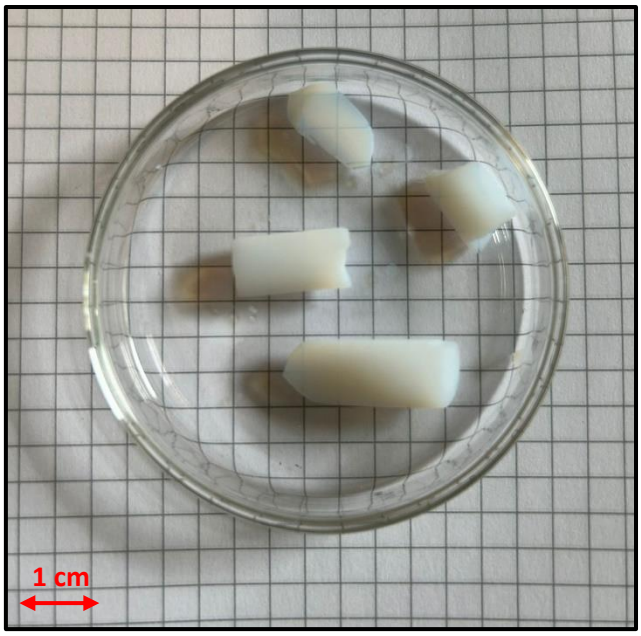

Figure 65: Samples of AlSi - APTES (7.5 mmol) aerogel.

A precision balance was employed for weighing with a single measurement (one measurement of diameter and one measurement of the length were conducted). It was assumed that the aerogel would retain a cylindrical shape corresponding to the geometry of the moulds.

Table *31* shows the dimensions, density, and volume shrinkage of the different samples. The diameters of the glass cylinders are 7 mm and 10.8 mm. The shrinkage of the diameter was calculated by measuring the initial and final diameter, while for the shrinkage of the length (since the initial length of the samples is unknown) it was assumed that it is equal in percentage to that of the diameter.

Table 31: Dimensions, density, and volume shrinkage of AlSi - APTES (7.5 mmol) aerogel

Diameter, cm	h, cm	Final volume, cm^3	Starting volume, cm^3	Volume shrinkage, cm^3	Weight, g	Apparent density, g/cm^3
0.57	0.65	0.166	0.307	0.141	0.0257	0.15
0.69	0.55	0.164	0.216	0.052	0.0268	0.13
0.57	0.66	0.168	0.312	0.144	0.0150	0.09

4.5.3 Reproduction

The production of AlSi-APTES aerogels (7.5 mmol) was conducted to ensure the consistency of our outcomes. Details regarding the quantities employed in the synthesis can be found in **Table *32*** and **Table *33***.

Table 32: Mass quantities of the reagents of the solution A

Solution	2 – butanol	TMOS	HCl solution 0.01 M
Solution A	5.7757 g	2.2866 g	0.3343 g

Table 33: Mass quantities of the reagents of the solution B

Solution	2 – butanol	ATSB
Solution B	1.6584 g	0.4310 g

Additional reagents:

- H_2O = 0.4316 g
- APTES = 0.8378 g
- Ammonia solution (1.0 M) = -

In this case, it was impossible to add the basic catalyst, because the solution gelled earlier (about fifty minutes after adding water and APTES). After the supercritical drying, the aerogels appear fragile and opaque (***Figure 66***).

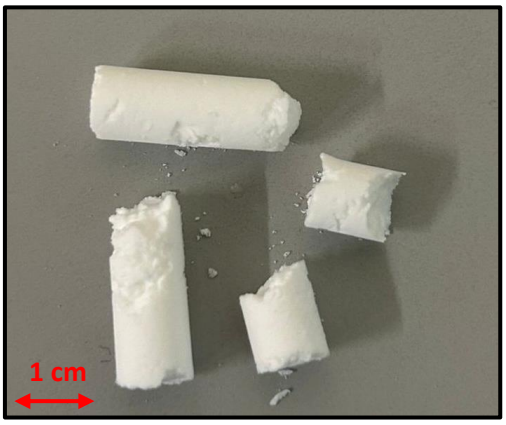

Figure 66: Supercritical drying of AlSi - APTES (7.5 mmol)_R aerogels.

A precision balance was employed for weighing with a single measurement (one measurement of diameter and one measurement of the length were conducted). It was assumed that the aerogel would retain a cylindrical shape corresponding to the geometry of the moulds.

Table *34* provides information regarding the dimensions, density, and volume reduction observed in different samples. The experimental setup employed glass cylinders with diameters measuring 7 mm and 10.8 mm. The diameters of the glass cylinders are 7 mm and 10.8 mm. The shrinkage of the diameter was calculated by measuring the initial and final diameter, while for the

shrinkage of the length (since the initial length of the samples is unknown) it was assumed that it is equal in percentage to that of the diameter.

Table 34: Dimensions, density, and volume shrinkage of the AlSi - APTES (7.5 mmol)_R aerogel

Internal diameter, cm	h, cm	Final volume, cm^3	Starting volume, cm^3	Volume shrinkage, cm^3	Weight, g	Apparent density, g/cm^3
0.65	1.89	0.627	1.378	0.751	0.0821	0.13
0.65	1.54	0.511	1.123	0.612	0.0598	0.12
0.67	0.81	0.286	0.609	0.323	0.0239	0.08
0.62	0.52	0.157	0.362	0.205	0.0238	0.15

4.6 Characterization of AlSi – APTES (7.5 mmol)

4.6.1 FTIR

The spectral range between 3200 and 3700 cm^{-1} is linked to the presence of –OH groups. Moreover, around 3300 cm^{-1} the (stretching) band of the amines is also seen. This last band was not visible in the 2.5 mmol sample probably because it was too weak and, therefore it was masked by the –OH band. Signals detected at approximately 2900 cm^{-1} can be attributed to -CH groups present in organic constituents. According to previous studies, a signal associated with the Al-OH group is identifiable at around 1640 cm^{-1} [42], [43]. Peaks centred at 1600 cm^{-1} suggest the presence of amino groups [27], [28]. Additionally, the various peaks observed near 1400 cm^{-1} are likely associated with organic components, as discussed in the literature [26] (***Figure 67***).

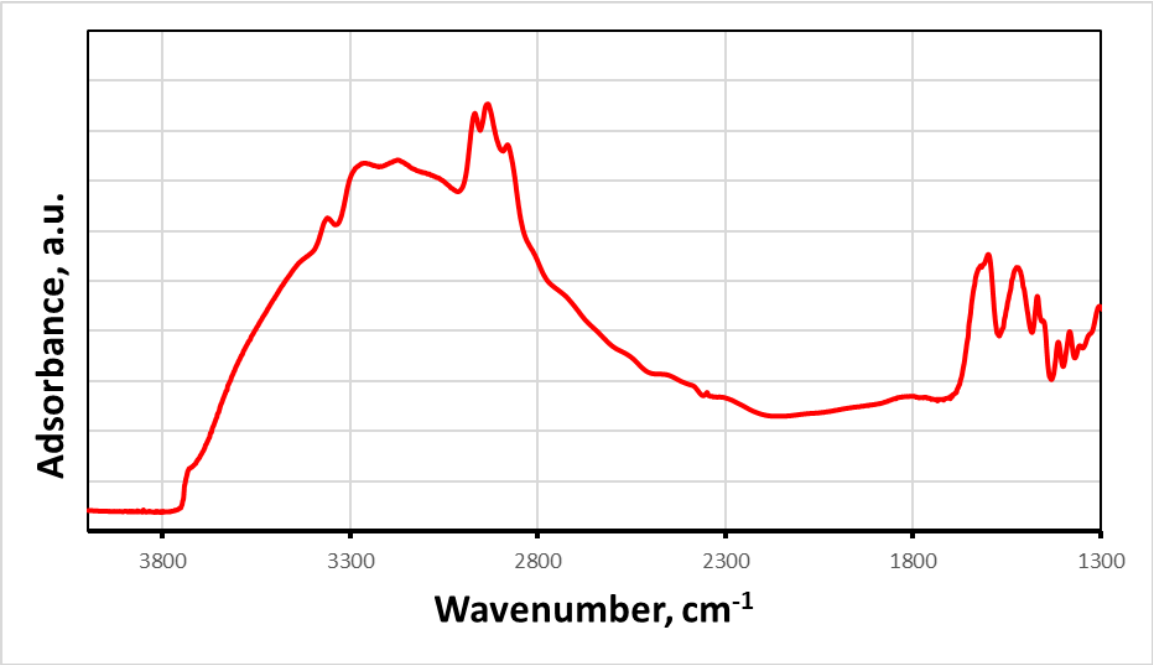

Figure 67: FTIR of AlSi - APTES (7.5 mmol) aerogel.

Figure 68 reports the FTIR of the reproduction of AlSi – APTES (7.5 mmol) aerogels. It shows the same trend as ***Figure 67***.

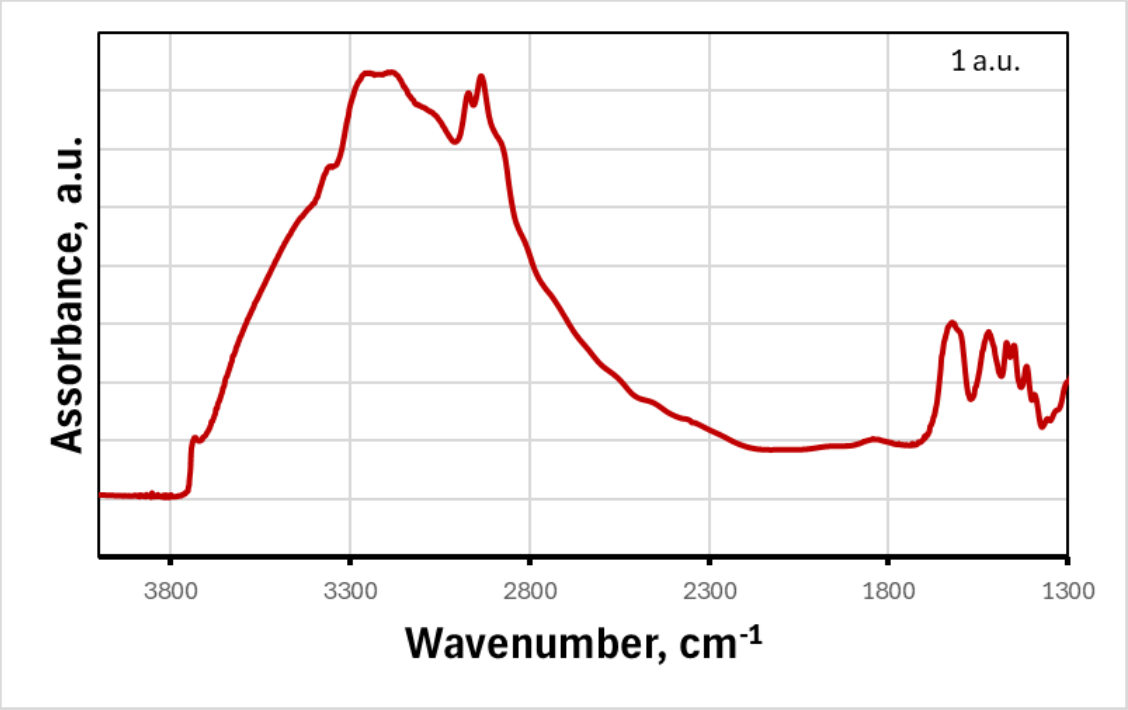

Figure 68: FTIR of AlSi - APTES (7.5 mmol)_R aerogels.

4.6.2 TGA

AlSi – APTES (7.5 mmol) aerogels exhibit weight losses with the temperature rise (***Figure 69***). Before reaching a temperature of 150 °C, the specimens underwent a weight reduction of 9.2%,

which is attributed to the removal of physically adsorbed water. Subsequently, within the temperature range of 150 °C to 800 °C, the degradation of organic constituents resulted in a mass loss of approximately 25.4%. The obtained value is not the triple that obtained with the *AlSi-APTES 2.5 mmol* sample, as would be expected, but is only a few percentage points higher. This result is probably due to the contribution of both the residual organic species of the precursors and the amine.

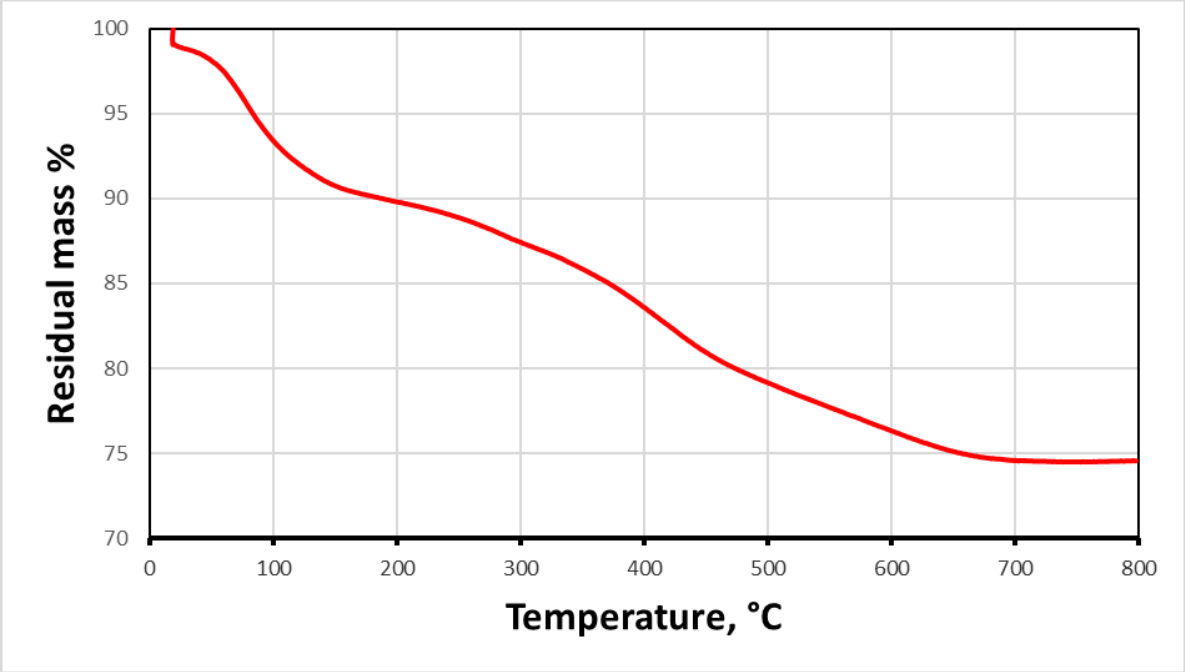

Figure 69: TGA of AlSi - APTES (7.5 mmol) aerogel.

The replication of AlSi – APTES (7.5 mmol) aerogels displays reductions in weight as the temperature increases. Before reaching 150°C, the samples experienced a weight decrease of 5.58%, primarily due to the elimination of physically adsorbed water. Following this, between 150°C and 800°C, the breakdown of organic components led to a mass loss of approximately 22.6% (***Figure 70***). The values obtained for the replicate are comparable to those of the 7.5 mmol sample.

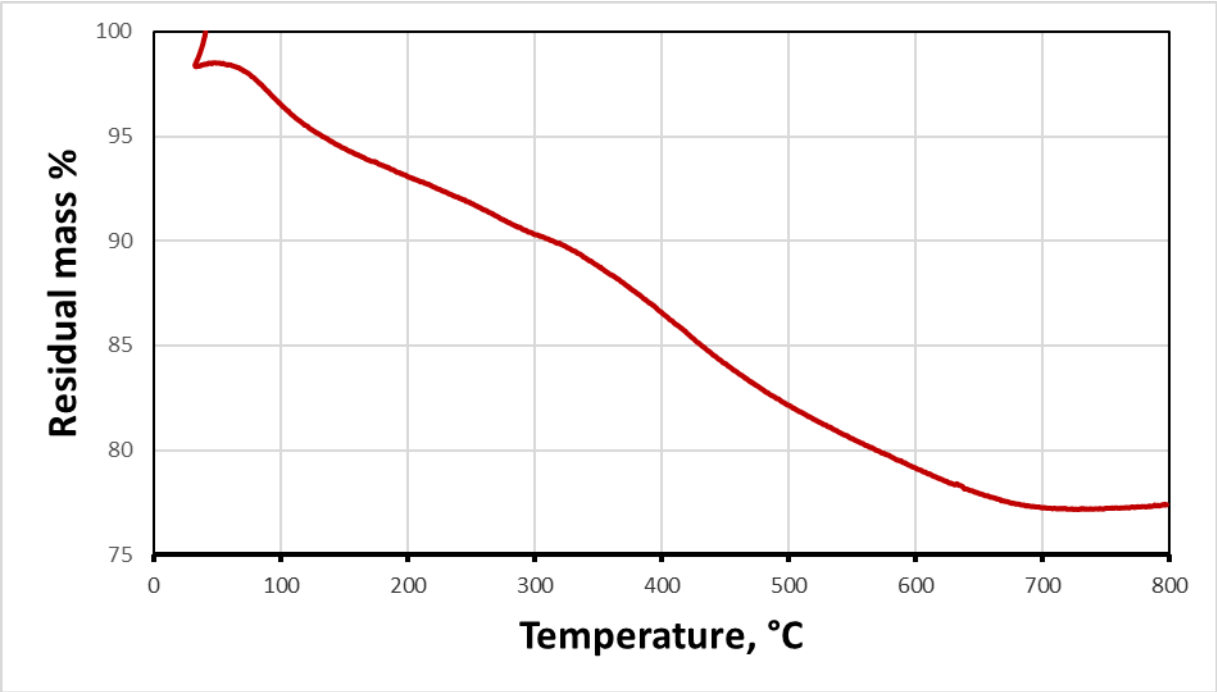

Figure 70: TGA of AlSi - APTES (7.5 mmol)_R aerogels.

It is interesting to observe that the mass rises at the end of the test. This is an artefact due to a buoyancy effect (artefact is observed for all samples).

4.6.3 X–ray diffraction

At high angles (***Figure 71***) the sample presents only an amorphous halo [32], [35], [36]

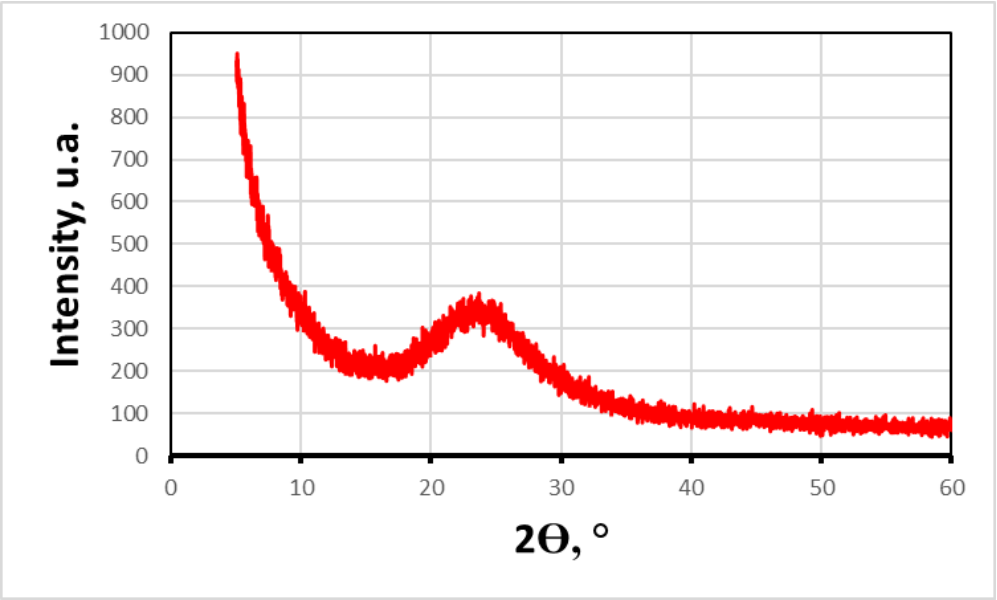

Figure 71: XRD at high angles of AlSi - APTES (7.5 mmol) aerogels.

AlSi – APTES (7.5 mmol) aerogels show no signs of ordered structures in the mesoporosity range (low angles) [31], [33], [48] (***Figure 72***).

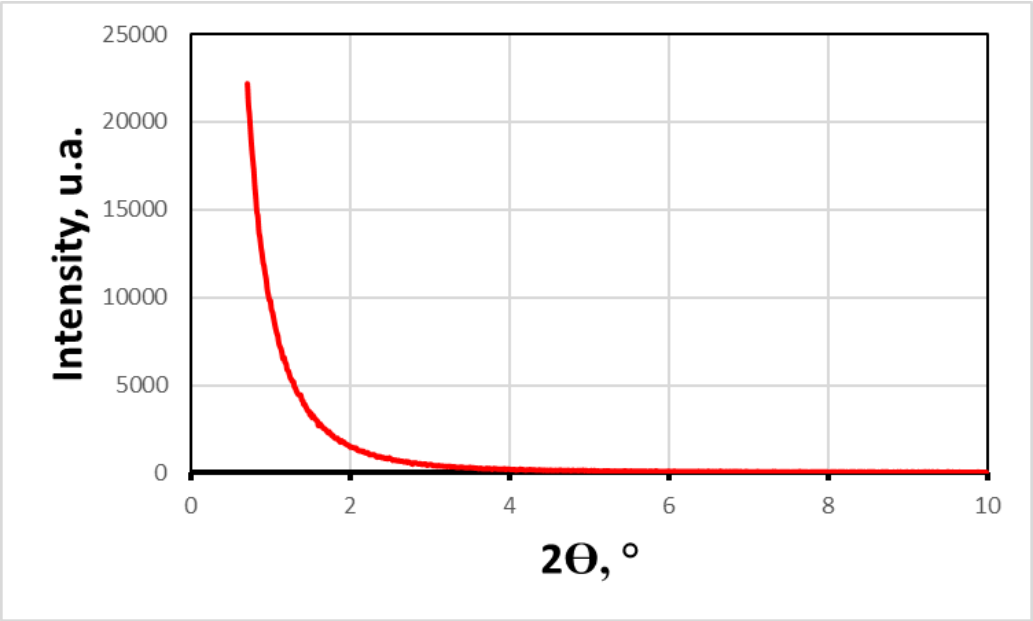

Figure 72: XRD at low angles of AlSi - APTES (7.5 mmol) aerogels.

4.6.4 N_2 adsorption

- Nitrogen adsorption isotherm

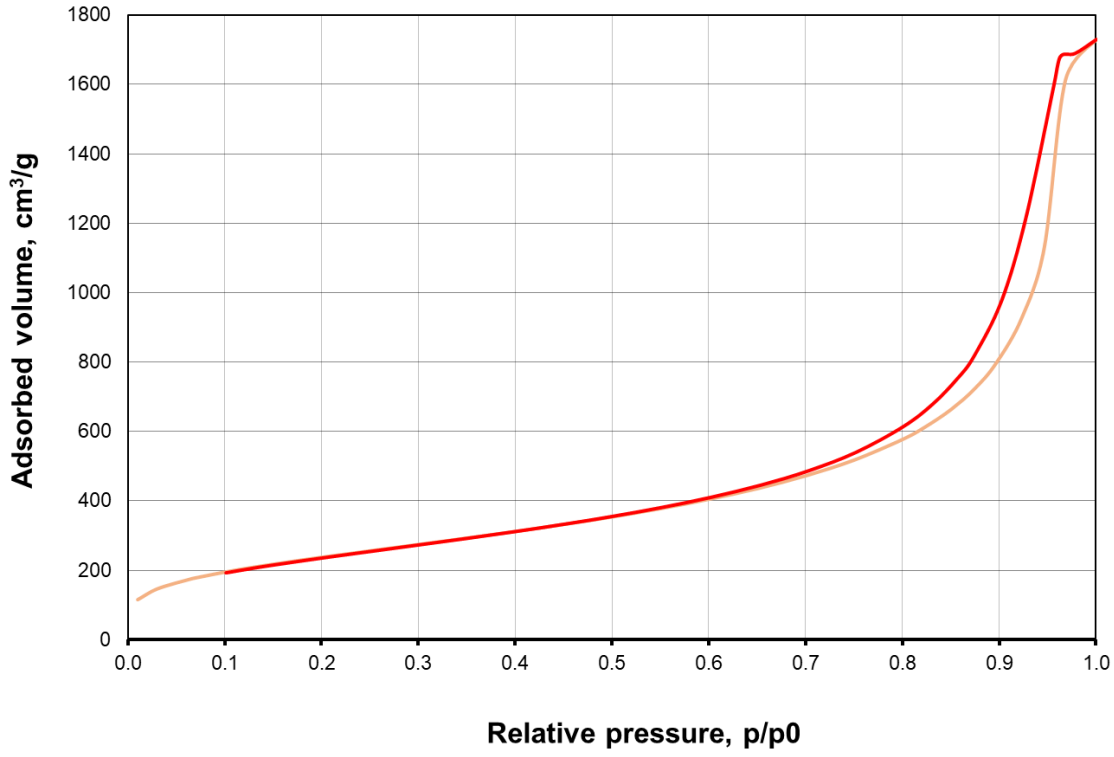

Figure 73: BET of AlSi - APTES (7.5 mmol) aerogel.

The assessment of specific surface area adheres to the Brunauer–Emmett–Teller (BET) approach. According to the classification provided by IUPAC, the curve is designated as type IV, characterized by the presence of a distinct H1 loop. The specific surface area is 878 m^2/g. The porous value is 2.5 cm^3/g (***Figure 74***).

- BJH

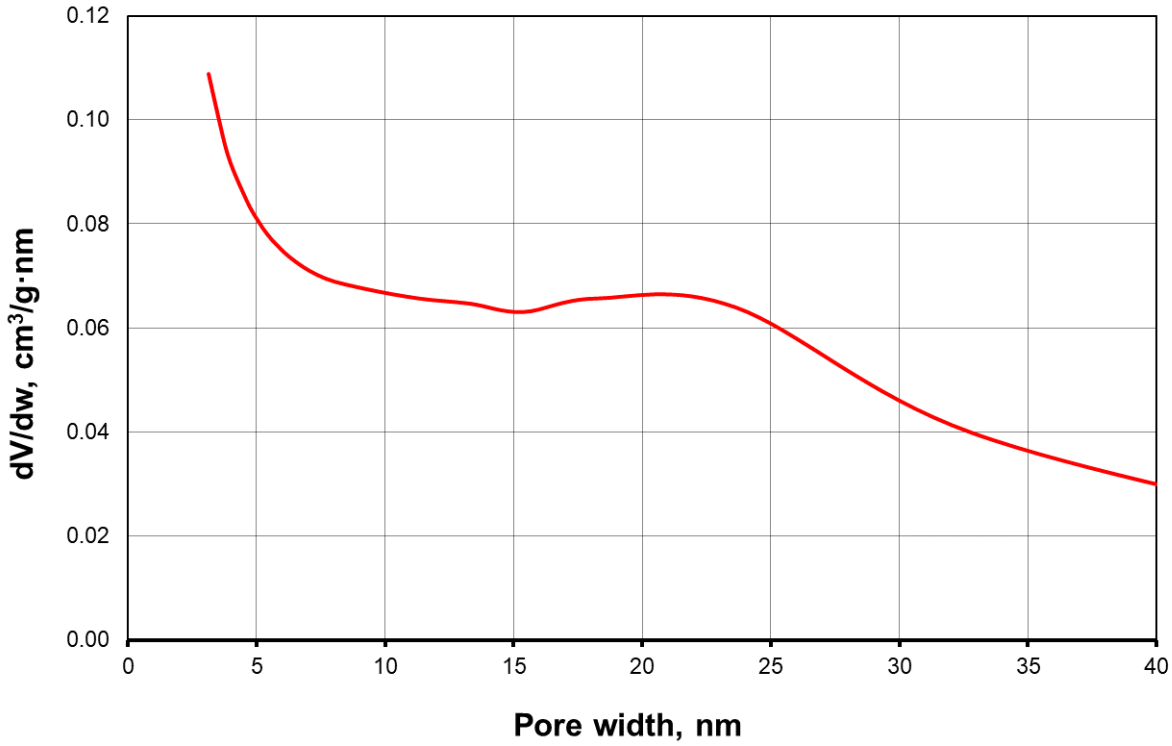

Figure 74: BJH of AlSi - APTES (7.5 mmol) aerogel.

Table 35 shows the textural properties of AlSi – APTES (7.5 mmol) aerogels.

Table 35: Summary of the textural properties of AlSi - APTES (7.5 mmol) aerogels

TEXTURAL PROPERTIES		
Specific surface area	Porous volume	Average pore diameter
878 m^2/g	2.5 cm^3/g	20.4 nm

The reproductions of BET and BJH of AlSi-APTES (7.5 mmol) aerogels are shown in ***Figure 75*** and ***Figure 76***.

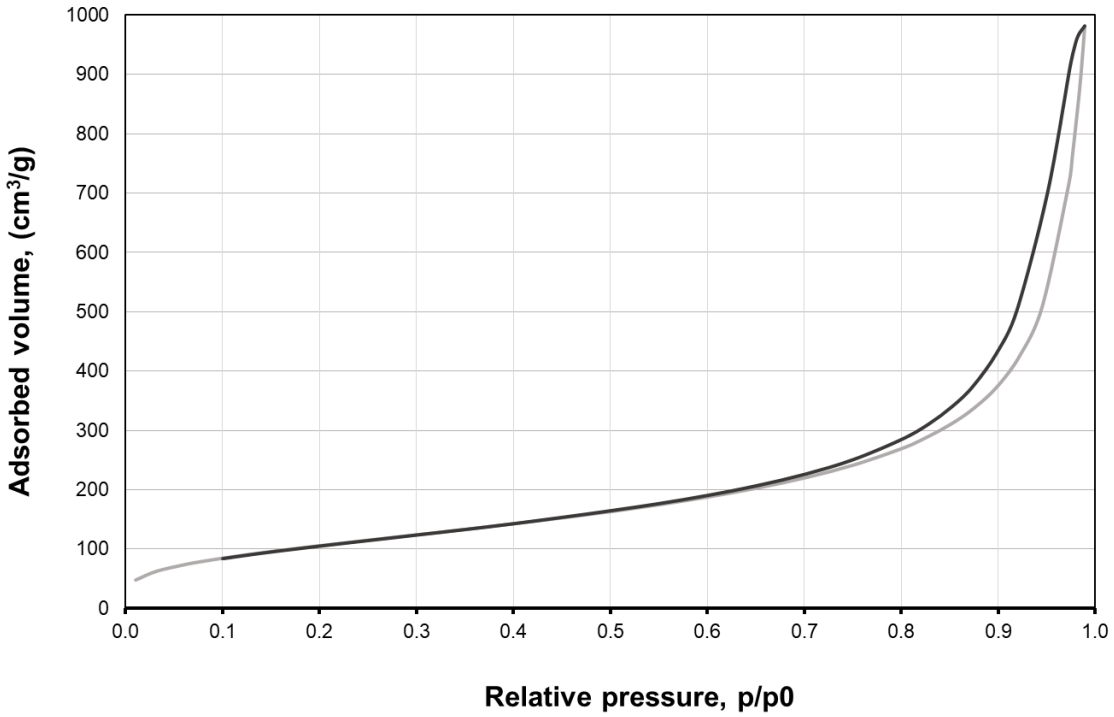

Figure 75: BET of AlSi - APTES (7.5 mmol)_R aerogels.

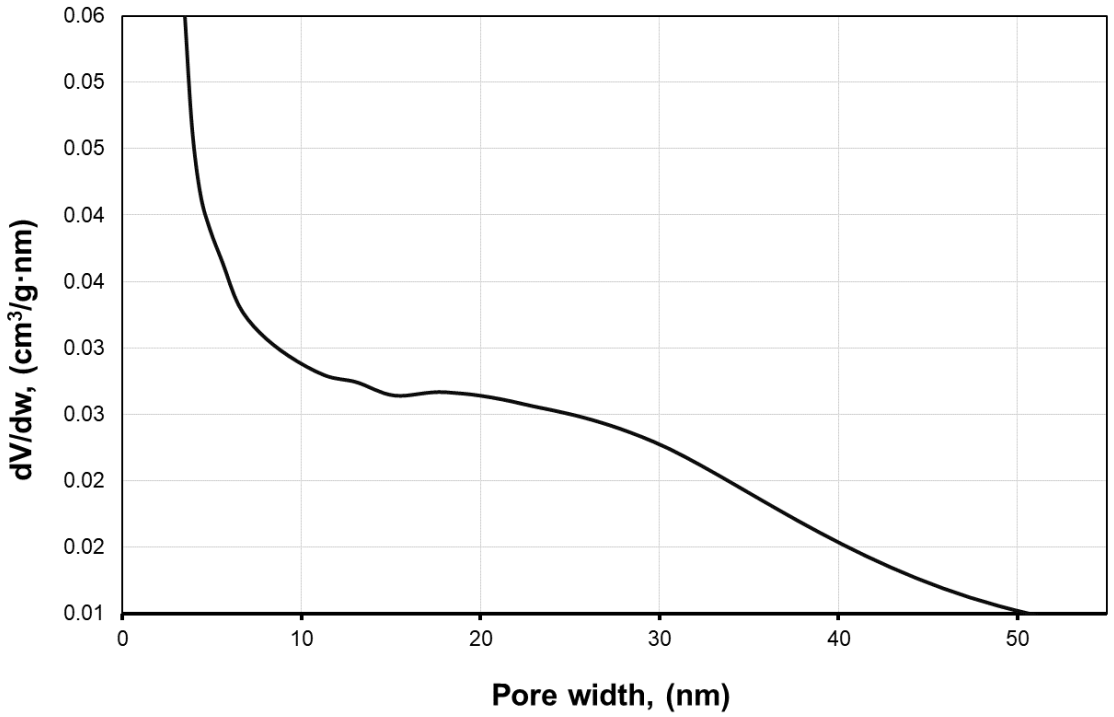

Figure 76: BJH of AlSi - APTES (7.5 mmol)_R aerogels.

The replica shows good reproducibility in terms of composition and crystalline structure, but not textural properties.

4.6.4.1 Xerogel analysis

In this section, the BET and BJH of xerogel AlSi+APTES (7.5 mmol) are presented. The specific surface area is 690.2 m^2/g. The porous value is 0.7 cm^3/g (***Figure 77***).

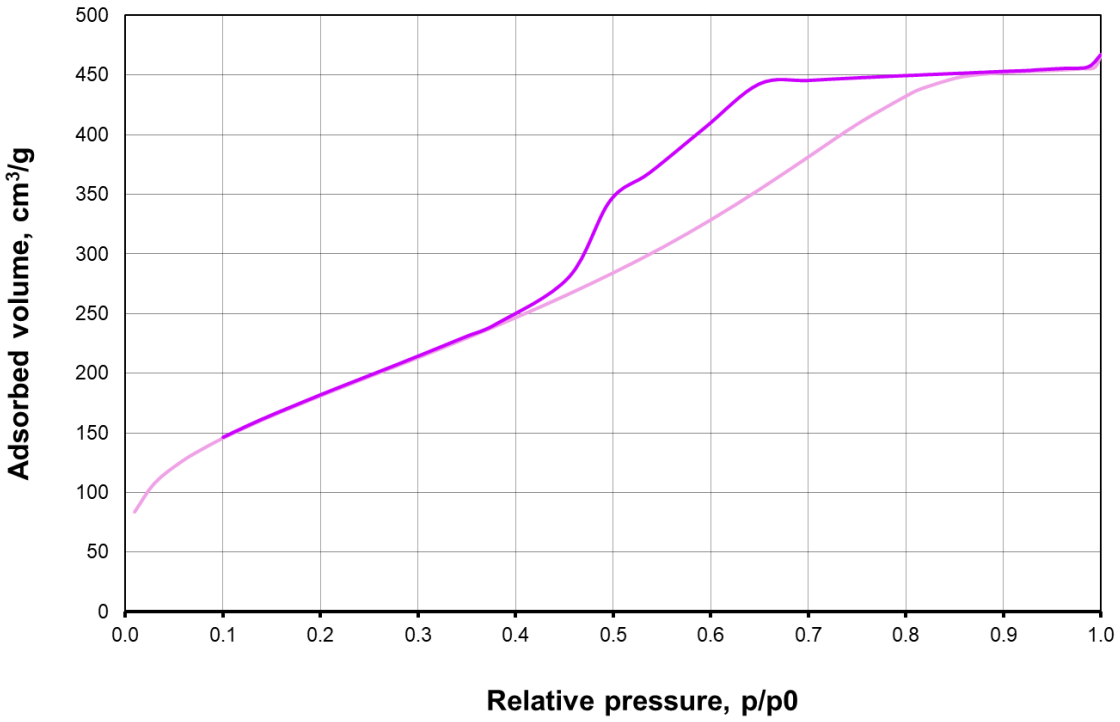

Figure 77: BET of AlSi+APTES (7.5 mmol)

According to ***Figure 78***, the distribution is single-mode, rather narrow, with a maximum of approximately 4 nm.

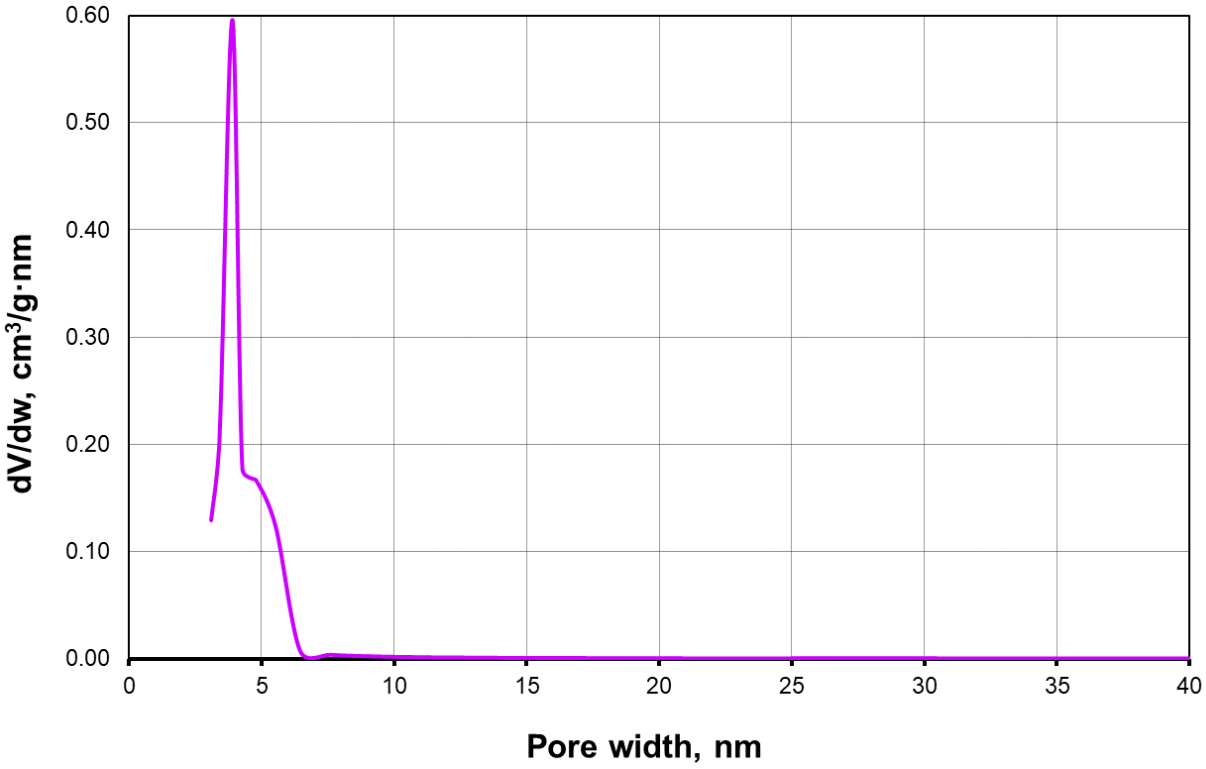

Figure 78: BJH of AlSi+APTES (7.5 mmol)

From these results, it can be confirmed the importance of supercritical drying to preserve the largest porosities and obtain a sample with high specific surface area and porous volume.

4.6.5 XPS

The survey spectrum and high-resolution spectra of C, O, N, and Al are shown in this section (***Figure 79***, ***Figure 80***, ***Figure 81***, ***Figure 82***, ***Figure 83***).

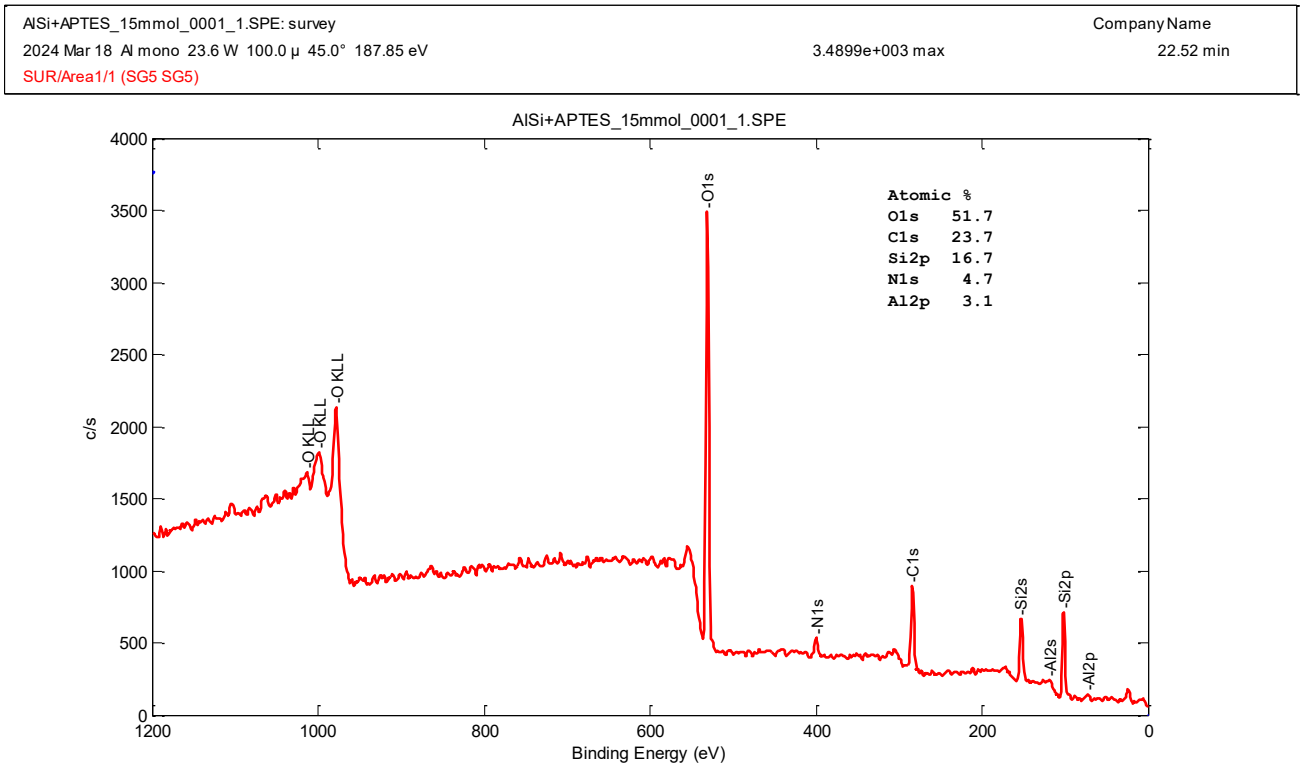

Figure 79: Survey of AlSi+APTES (7.5 mmol) sample*.

In ***Figure 80***, the peak at 284 eV confirms the presence of Carbon [53].

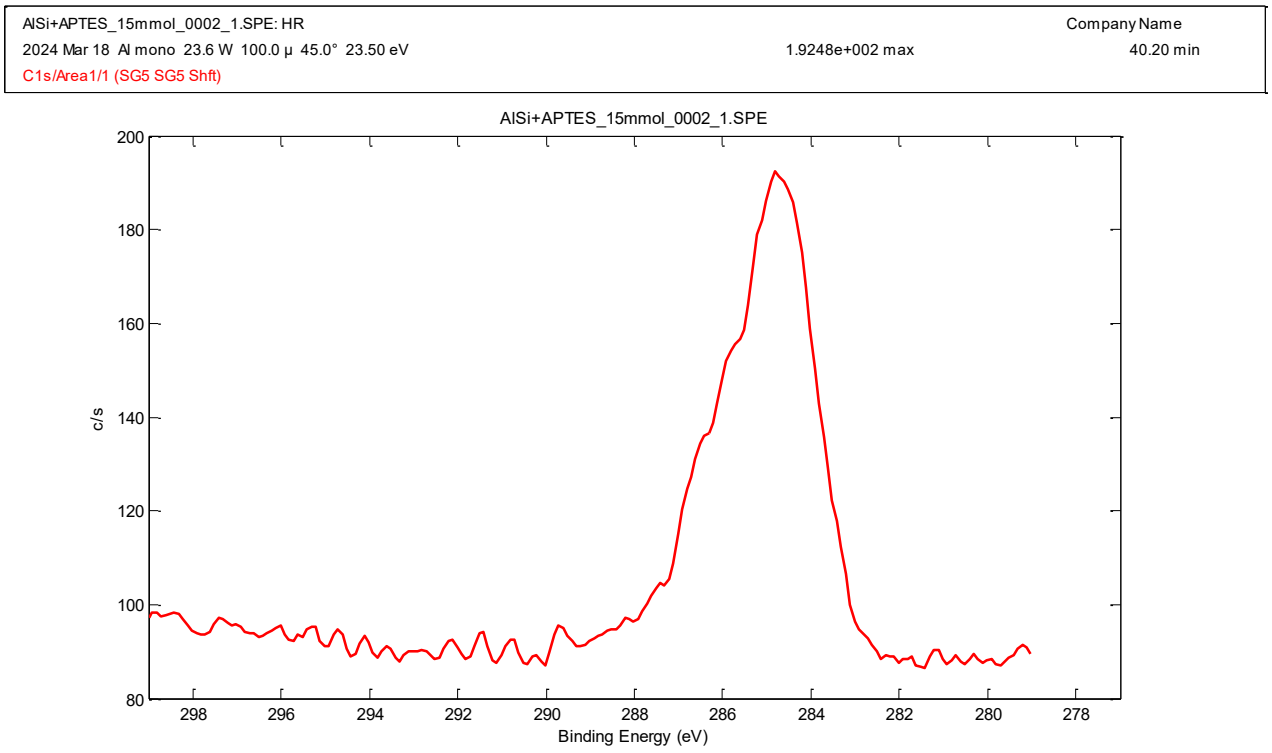

Figure 80: high-resolution spectra of C in AlSi+APTES (7.5 mmol) sample*.

In ***Figure 81***, the peak at 534 eV indicates the presence of Oxygen [38].

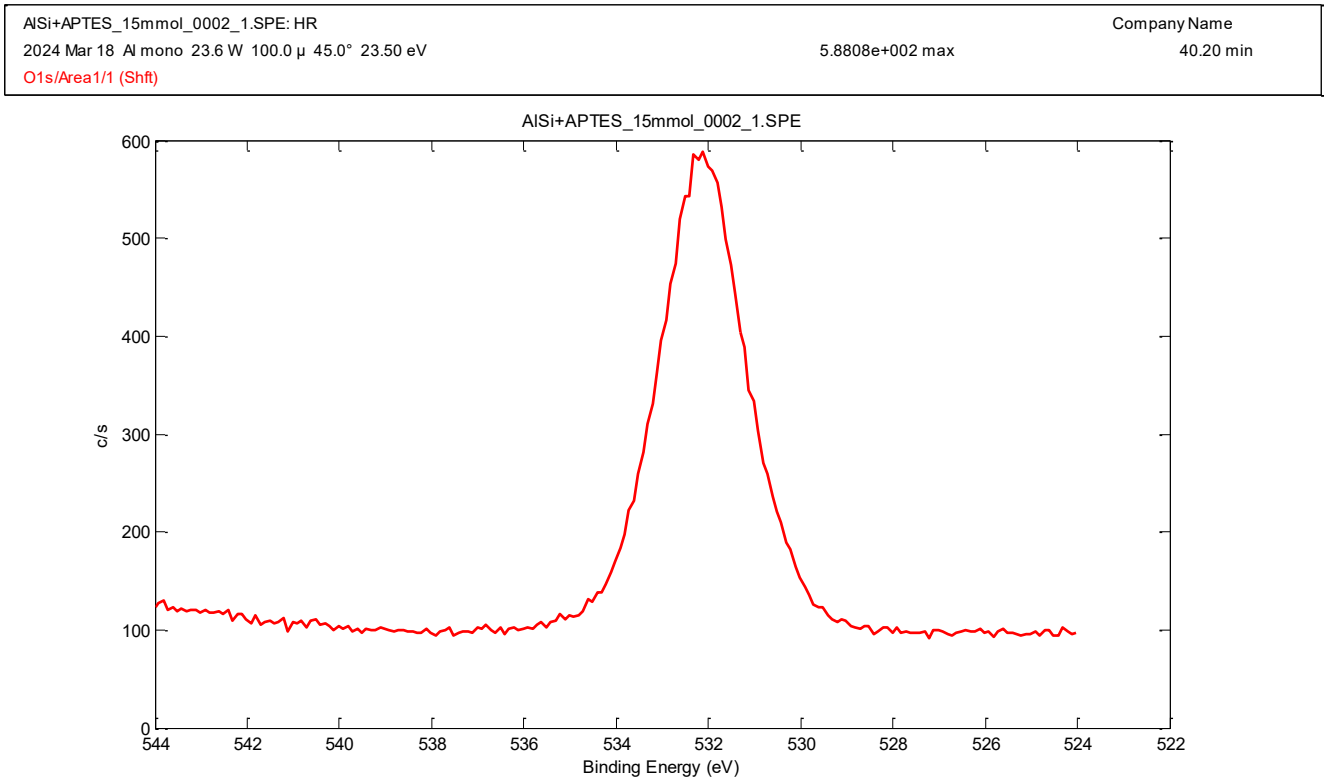

Figure 81: high-resolution spectra of O in AlSi+APTES (7.5 mmol) sample*.

In ***Figure 82***, the highest peak at 402 eV shows protonated Nitrogen [54] and at 398 eV the deprotonated Nitrogen.

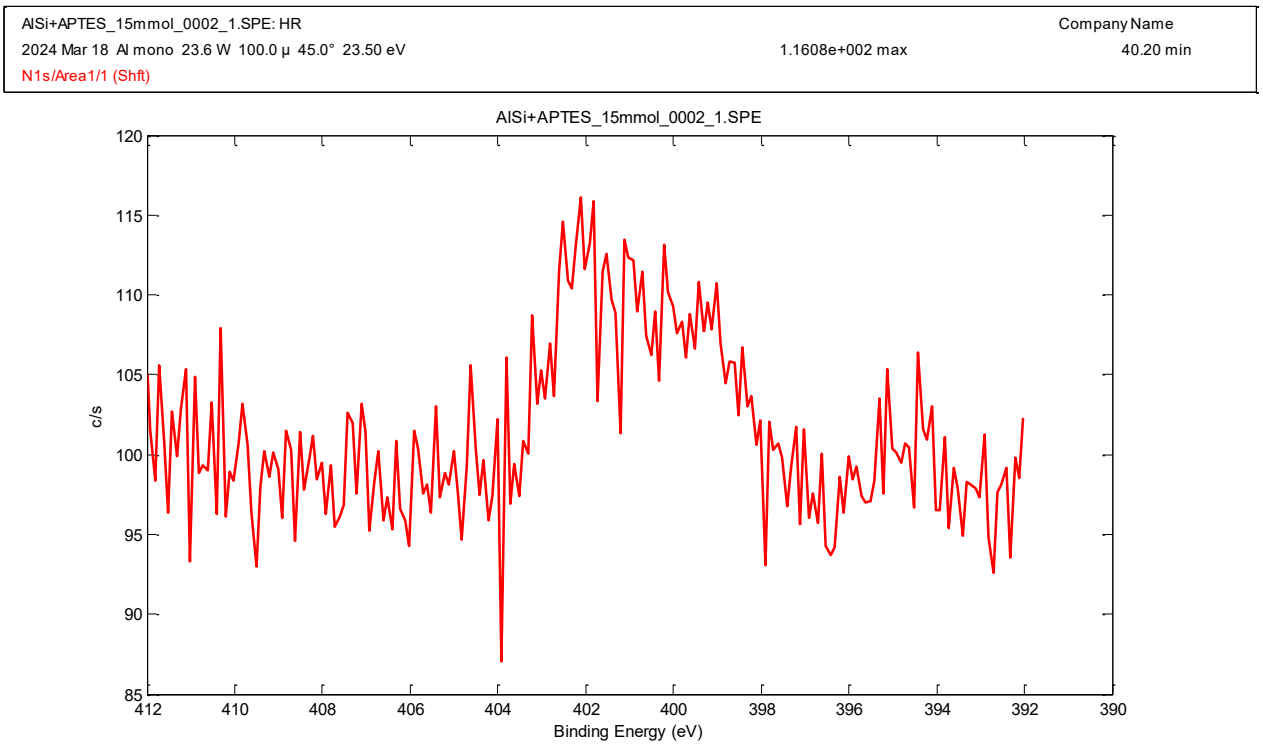

Figure 82: high-resolution spectra of N in AlSi+APTES (7.5 mmol) sample*.

In ***Figure 83***, the highest peak at 73 eV shows Al [52], [57].

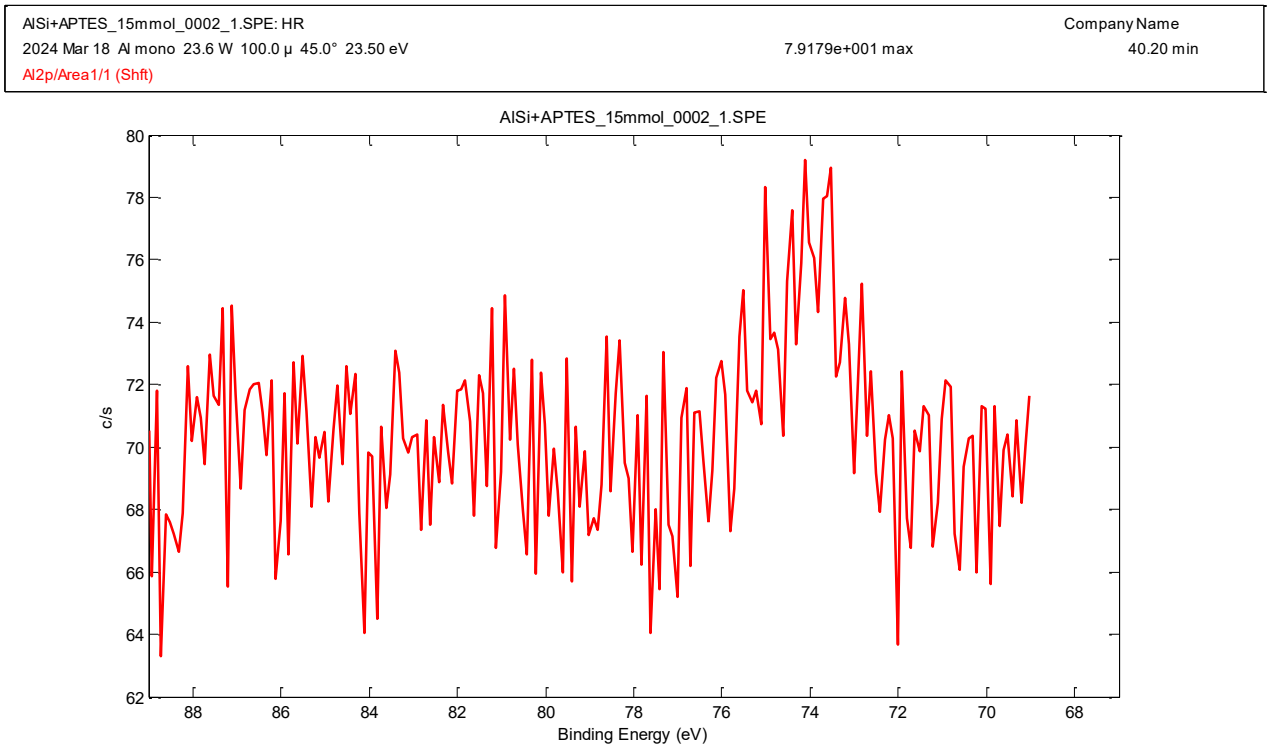

Figure 83: high-resolution spectra of Al in AlSi+APTES (7.5 mmol) sample*.

*Please take into consideration that in graphs there is the indication “AlSi+APTES (15 mmol)” that is referred to the sample “AlSi+APTES (7.5 mmol)”.

4.7 Preparation of AlSi – APTES (22.5 mmol)

4.7.1 Gel synthesis

In this experiment, the quantity of APTES has been augmented to three times the number of AlSi-APTES (7.5 mol) (**Table 36**, **Table 37**). This adjustment aims to investigate the adsorption behaviour of carbon dioxide under these specific conditions. Increasing the APTES concentration relative to AlSi-APTES could amplify the adsorption capacity for CO_2, allowing for a more comprehensive examination of the adsorption process. This strategic adjustment offers insights into how variations in APTES concentration influence the interaction between the material and CO_2.

Table 36: Mass quantities of the reagents of the solution A

Solution	2 – butanol	TMOS	HCl solution 0.01 M
Solution A	11.5307 g	4.5713 g	0.6207 g

Table 37: Mass quantities of the reagents of the solution B

Solution	2 – butanol	ATSB
Solution B	3.2873 g	0.9134 g

Additional reagents:

- APTES = 4.9989g
- H_2O = 1.6950 g
- Ammonia solution (1.0 M) = -

A gelation occurred before the addition of the basic catalyst (after about 10 minutes from the addition of water and APTES). The gel was covered with EtOH and left to age for a week.

Table *38* shows the molar ratio of reagents of AlSi – APTES (22.5 mmol) in the function of TMOS + ATSB. It was chosen to work with an excess quantity of water to guarantee the hydrolysis of all the chemical species.

Table 38: Molar ratio of reagents of AlSi - APTES (22.5 mmol)

Sample	ATSB	TMOS	TMOS + ATSB	Ammonia Solution 1.0 M	HCl solution 0.01 M	2 – butanol	APTES	H_2O^*
AlSi – APTES (22.5 mmol)	0.1	0.9	1	8	0.9	6	0.23	10.5

4.7.2 Supercritical drying process

The gels underwent supercritical drying with carbon dioxide in an autoclave (40 mL stainless steel vessel with an internal diameter of 14 mm) for 90 minutes (105 bar and 40 °C), where samples were separated with Teflon spacers. ***Figure 84*** shows the aerogels of 22.5 mmol after the supercritical drying process.

Figure 84: Supercritical drying of the AlSi - APTES (22.5 mmol) aerogels.

A precision balance was employed for weighing with a single measurement (one measurement of diameter and one measurement of the length were conducted). It was assumed that the aerogel would retain a cylindrical shape corresponding to the geometry of the moulds.

Table *39* presents data on dimensions, density, and volume reduction recorded across various specimens. In the conducted experiments, glass cylinders of 7 mm internal diameter were utilized. The shrinkage of the diameter was calculated by measuring the initial and final diameter, while for the shrinkage of the length (since the initial length of the samples is unknown) it was assumed that it is equal in percentage to that of the diameter.

Table 39: Dimensions, density, and volume shrinkage of the production of AlSi - APTES (22.5 mmol) aerogel

Internal diameter, cm	h, cm	Starting volume, cm^3	Final volume, cm^3	Volume shrinkage, cm^3	Weight, g	Apparent density, g/cm^3
0.68	1.43	0.52	0.27	0.25	0.0860	0.17
0.67	1.64	0.58	0.31	0.27	0.1085	0.19
0.61	1.84	0.54	0.31	0.22	0.1263	0.23
0.61	1.75	0.51	0.20	0.21	0.1142	0.22
0.67	1.77	0.62	0.33	0.29	0.0963	0.15
0.61	1.34	0.39	0.23	0.16	0.0815	0.21
0.67	1.02	0.36	0.19	0.17	0.0576	0.16
0.55	1.23	0.29	0.19	0.10	0.0551	0.19

4.8 Characterisation of AlSi – APTES (22.5 mmol)

4.8.1 FTIR

The spectral range of 3200 to 3700 cm^{-1} indicates the presence of –OH groups. Additionally, a stretching band of amines appears around 3300 cm^{-1}. Signals around 2900 cm^{-1} are attributed to -CH groups found in organic constituents. Previous research identifies a signal corresponding to the Al-OH group near 1640 cm^{-1}. Peaks around 1600 cm^{-1} suggest amino groups. Moreover, various peaks near 1400 cm^{-1} are probably associated with organic components, as noted in the literature (***Figure 85***) [40], [43], [46], [54].

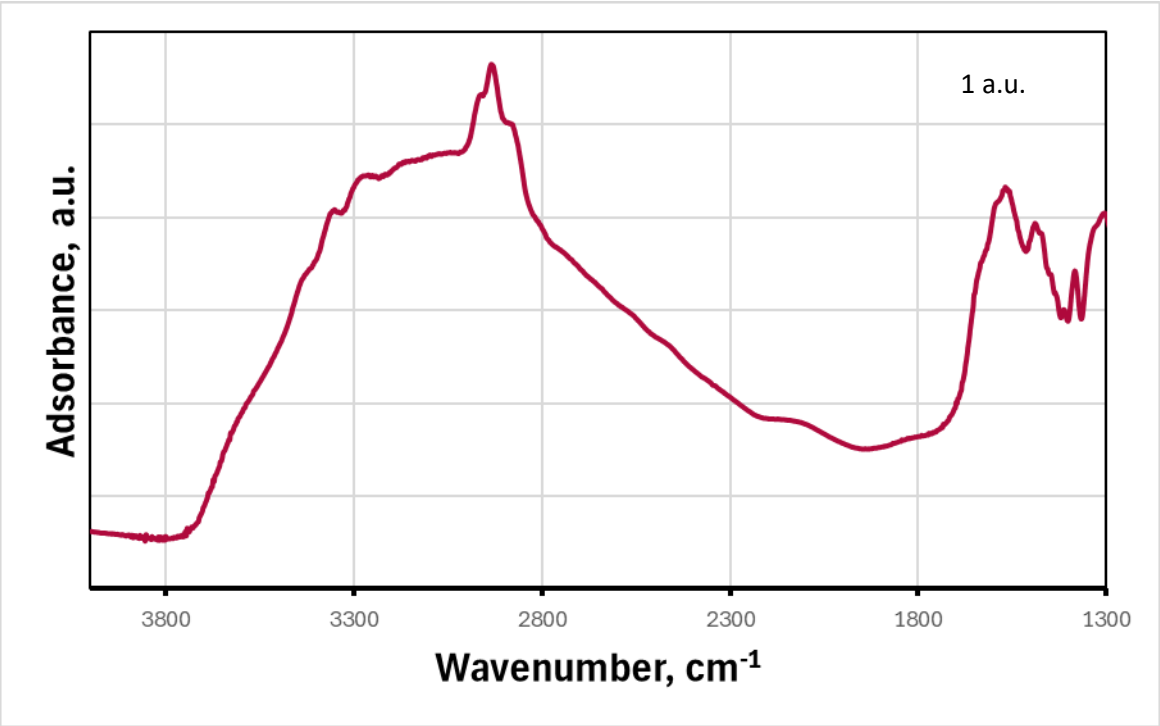

Figure 85: FTIR of AlSi-APTES (22.5 mmol) aerogels.

4.8.2 TGA

AlSi – APTES (22.5 mmol) aerogels display weight loss as the temperature increases. Before reaching 150 °C, the specimens experienced an 8.5% weight reduction, attributed to the evaporation of physically adsorbed water. Between 150 °C and 800 °C, the degradation of organic constituents caused an additional mass loss of about 32.8 %, a value higher than the ones found in 2.5 mmol and 7.5 mmol aerogels. This difference is coherent with a higher amine content as well as, probably, a higher residue of organic species from the precursors (**Figure *86*Figure *86***).

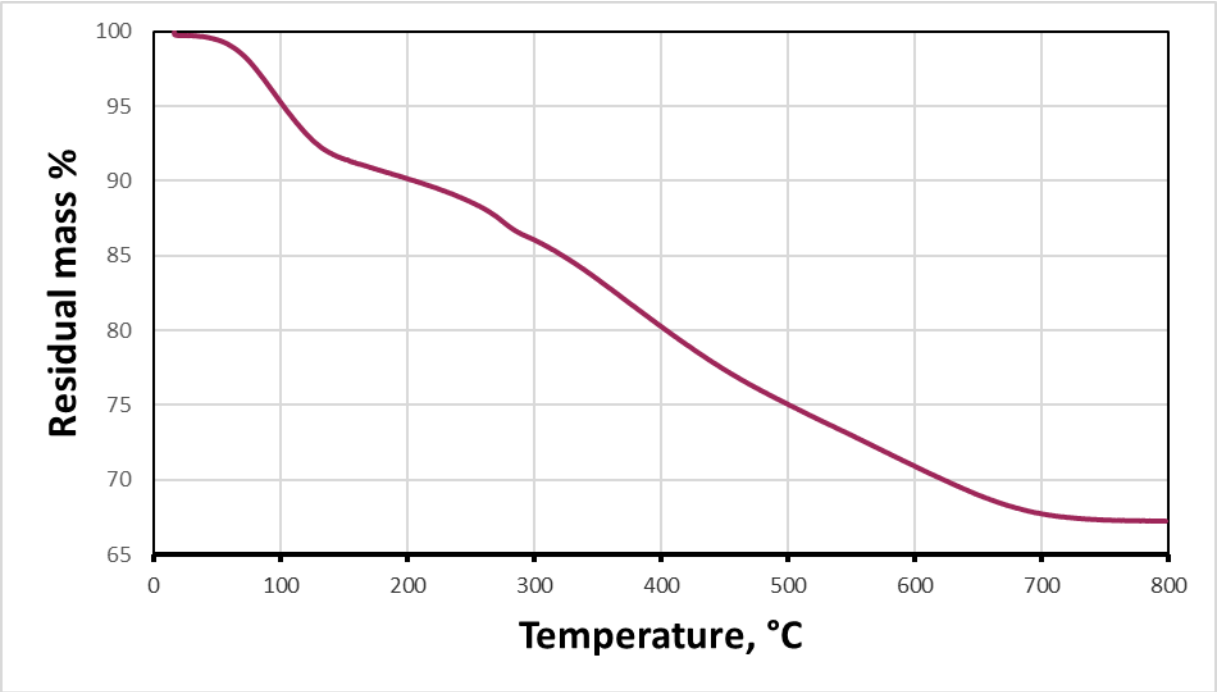

Figure 86: TGA of AlSi-APTES (22.5 mmol) aerogels.

4.8.3 N_2 Adsorption

- Nitrogen adsorption isotherm

The specific surface area was assessed using the Brunauer–Emmett–Teller (BET) method. According to IUPAC classification, the curve corresponds to a type IV isotherm, characterized by a distinct H1 hysteresis loop. The specific surface area measured is 527 m^2/g, and the pore volume is 1.2 cm^3/g (***Figure 87***).

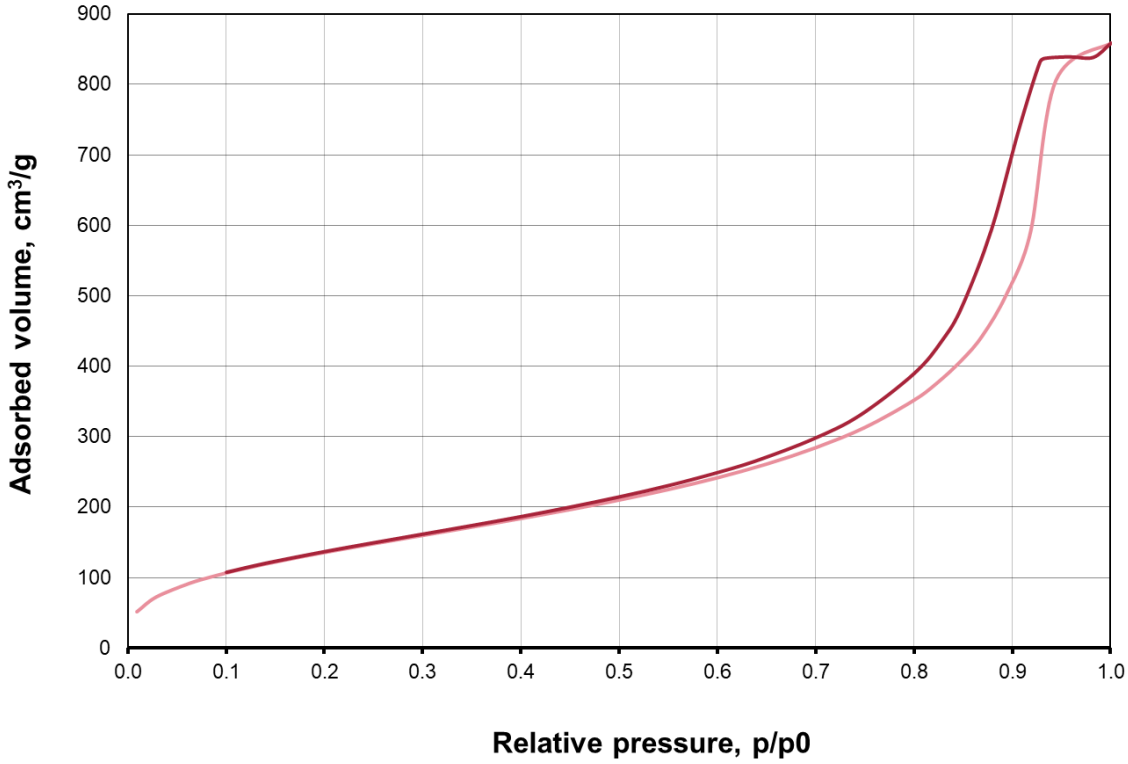

Figure 87: BET of AlSi-APTES (22.5 mmol) aerogels.

- BJH

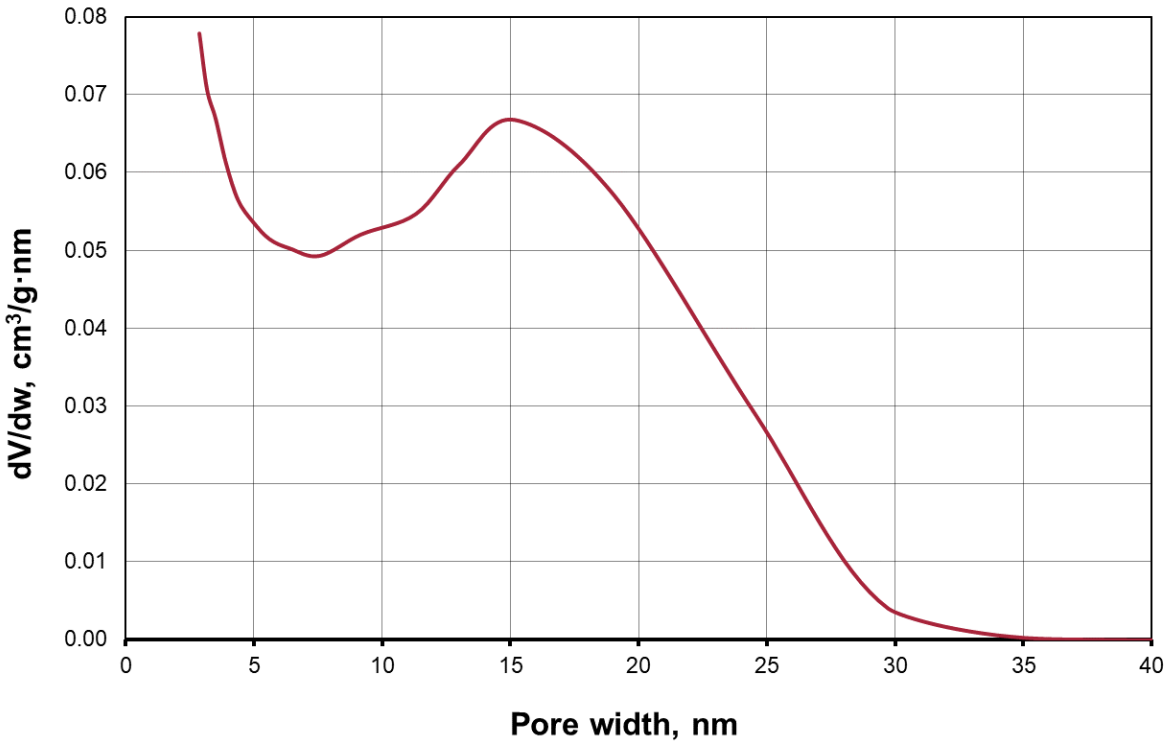

Figure 88: BJH of AlSi-APTES (22.5 mmol) aerogels.

Table 40 shows the textural properties of AlSi – APTES (22.5 mmol) aerogels.

Table 40: Textural properties of AlSi-APTES (22.5 mmol) aerogels.

TEXTURAL PROPERTIES		
Specific surface area	Porous volume	Average pore diameter
527 m^2/g	1.2 cm^3/g	15 nm

4.8.4 XPS

This section presents the survey spectrum along with the high-resolution spectra for carbon (C), oxygen (O), nitrogen (N), and aluminium (Al).

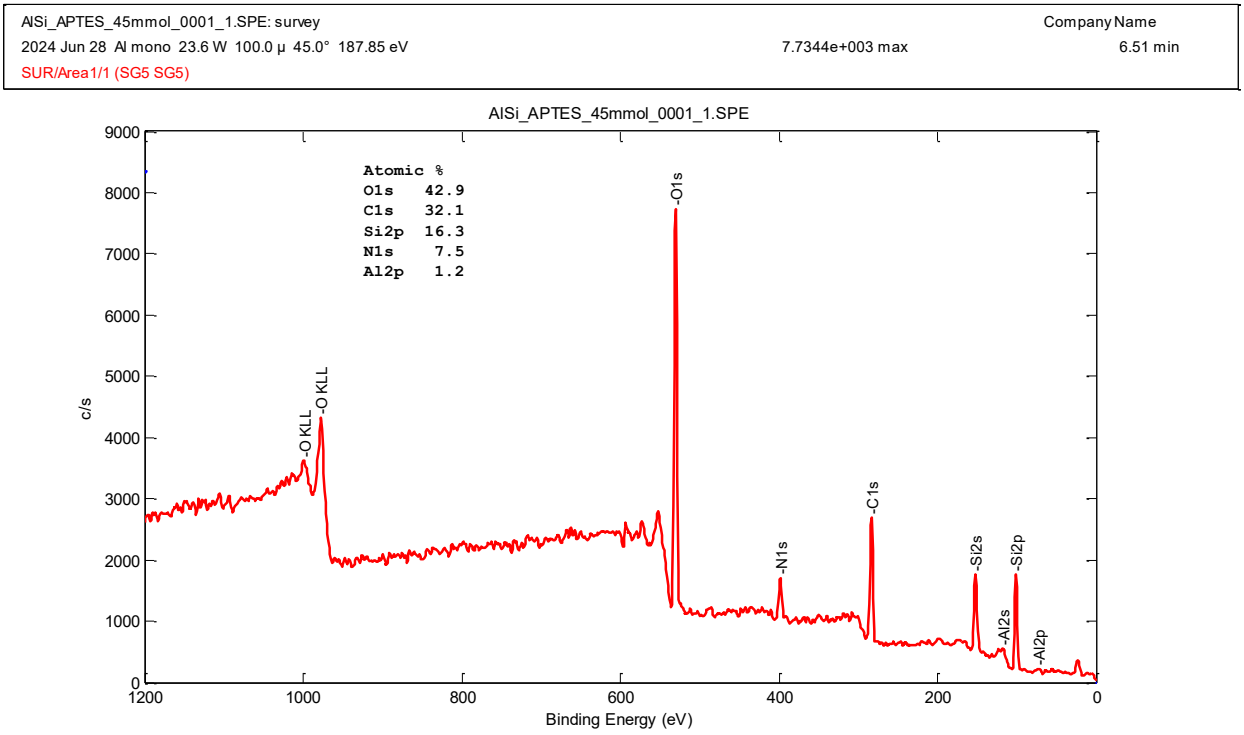

Figure 89: Survey of AlSi+APTES (22.5 mmol) sample*.

In ***Figure 90***, the peak at 285 eV confirms the presence of Carbon [53].

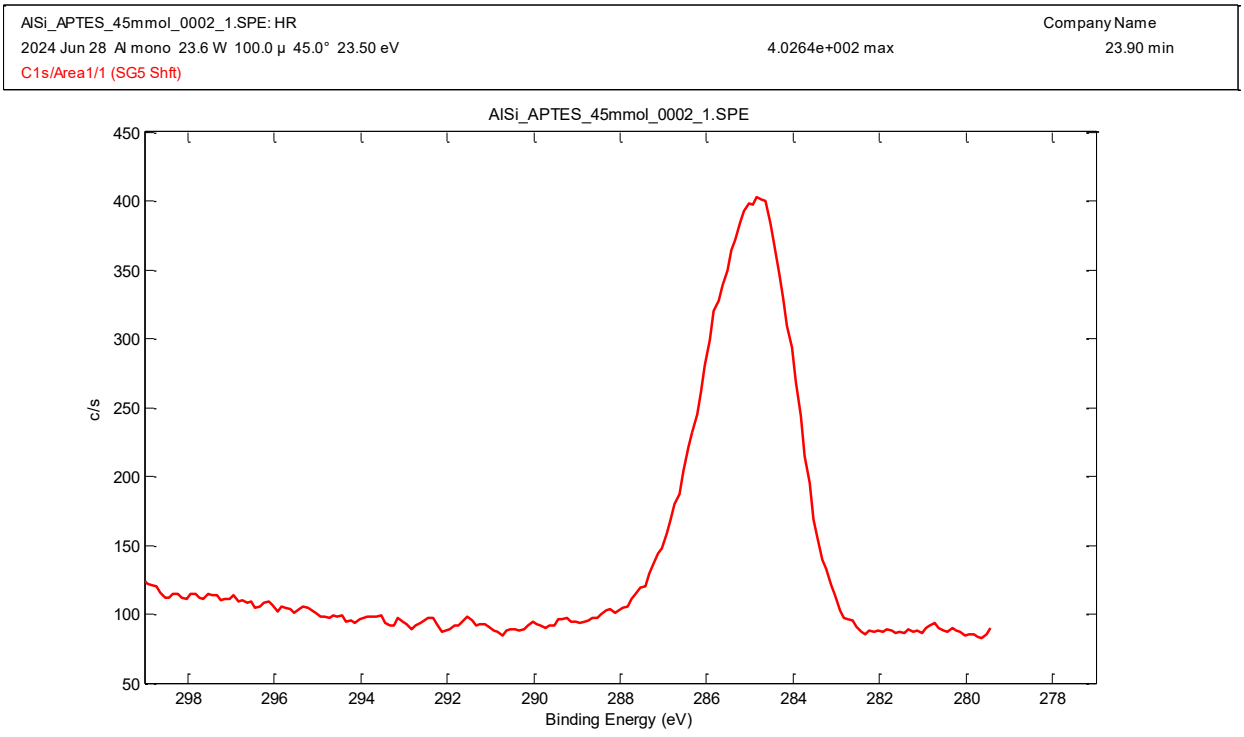

Figure 90: high-resolution spectra of C in AlSi+APTES (22.5 mmol) sample*.

In **Figure 91**, the peak at 532 eV indicates the presence of Oxygen [38].

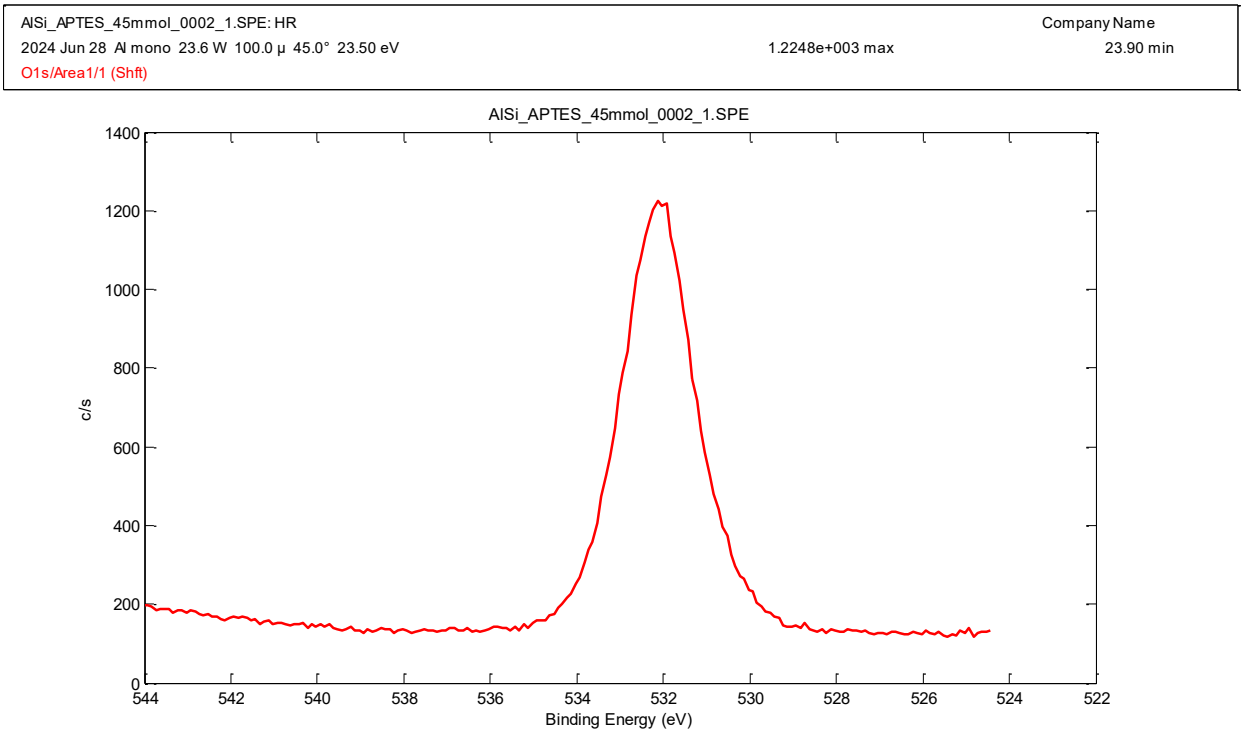

Figure 91: high-resolution spectra of O in AlSi+APTES (22.5 mmol) sample*.

In ***Figure 92***, the highest peak at 402 eV shows protonated Nitrogen [54] and at 399 eV the deprotonated Nitrogen.

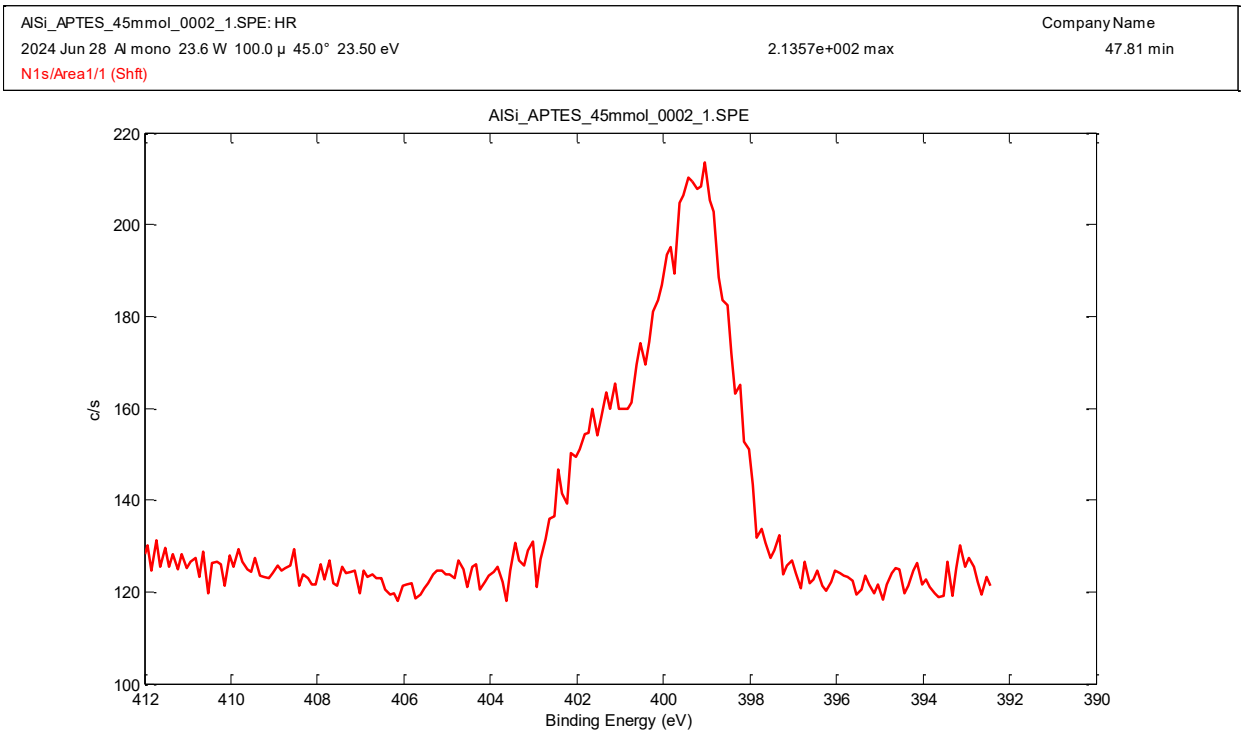

Figure 92: high-resolution spectra of N in AlSi+APTES (22.5 mmol) sample*.

In ***Figure 93***, the highest peak at 73 eV shows Al [52], [57].

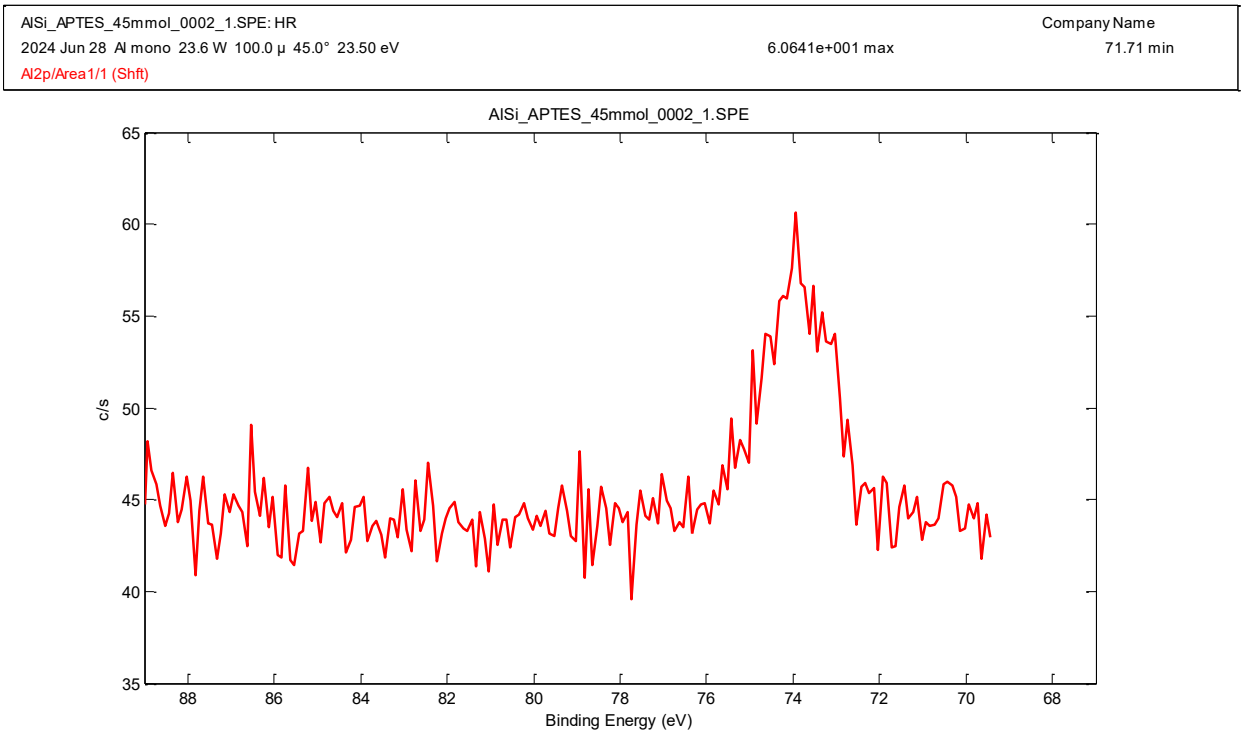

Figure 93: high-resolution spectra of Al in AlSi+APTES (22.5 mmol) sample*.

*Please take into consideration that in graphs there is the indication "AlSi+APTES (45 mmol)" that is referred to the sample "AlSi+APTES (22.5 mmol)".

Chapter 5

CO_2 adsorption performance

5.1 Volumetric tests

5.1.1 Silica – alumina aerogels

The volumetric experiments conducted to examine the CO_2 absorption on the aerogels consist of two subsequent runs, spaced out by a degas at room temperature. The first run aims to measure the amount of CO_2 adsorbed onto the samples while the second suggests the presence of potentially irreversible phenomena. Regarding the reference sample, AlSi, the maximum quantity of CO_2 adsorbed is approximately 1 mmol/g (see **Figure *94***) at about 1 bar. Since the two runs are superimposable, no irreversible adsorption phenomena are observed.

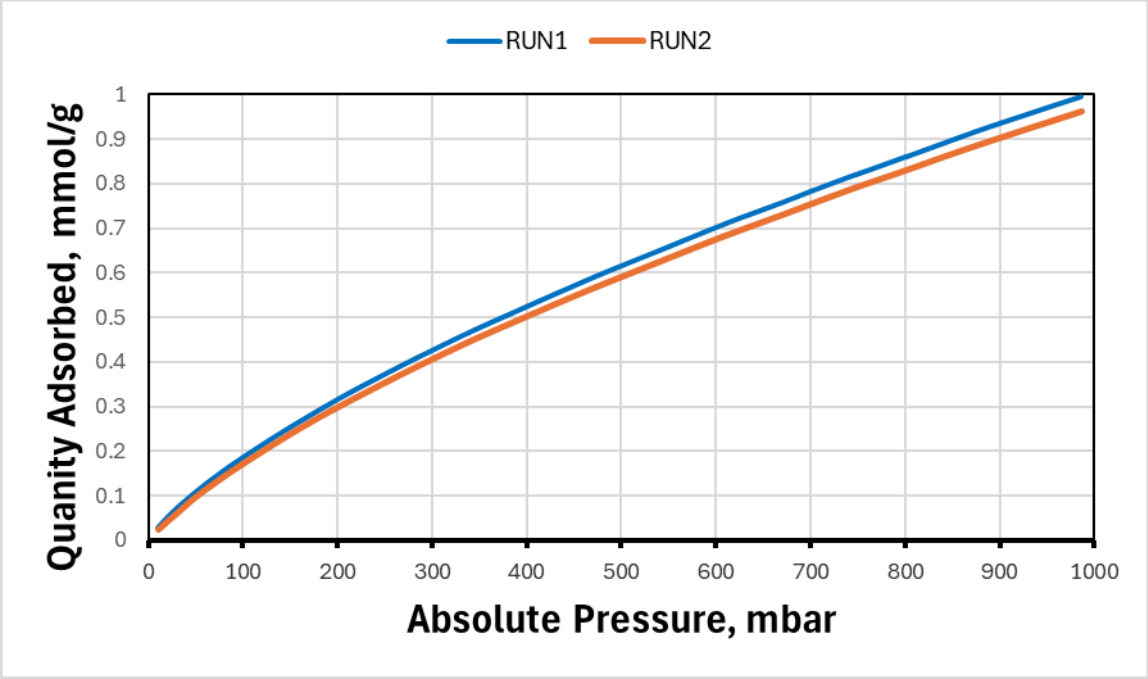

Figure 94: Run1 and Run2 of silica alumina aerogels.

5.1.2 AlSi – APTES (2.5 mmol, 7.5 mmol, and 22.5 mmol)

Figure 95 and ***Figure 96*** show the volumetric curves of the 2.5 and 7.5 mmol samples, respectively. In both cases, the maximum adsorbed value is around 0.90 mmol/g (more precisely 0.89 mmol/g for 2.5 mmol and 0.90 mml/g for 7.5 mmol).

The 2.5 mmol sample does not present any irreversible phenomenon, while for the 7.5 mmol, it seems that a minority part of the adsorption phenomena is irreversible (at room temperature) as RUN2 does not overlap with RUN1 but shows slightly lower values. For AlSi-APTES (2.5 mmol) and AlSi-APTES (7.5 mmol), the maximum quantity of CO_2 adsorbed is approximately 0.9 mmol/g. For AlSi-APTES (22.5 mmol), shown in ***Figure 97***, the maximum quantity of CO_2 adsorbed is approximately 2 mmol/g (1.94 mmol/g). In this last case, it is important to underline that there is a certain irreversibility.

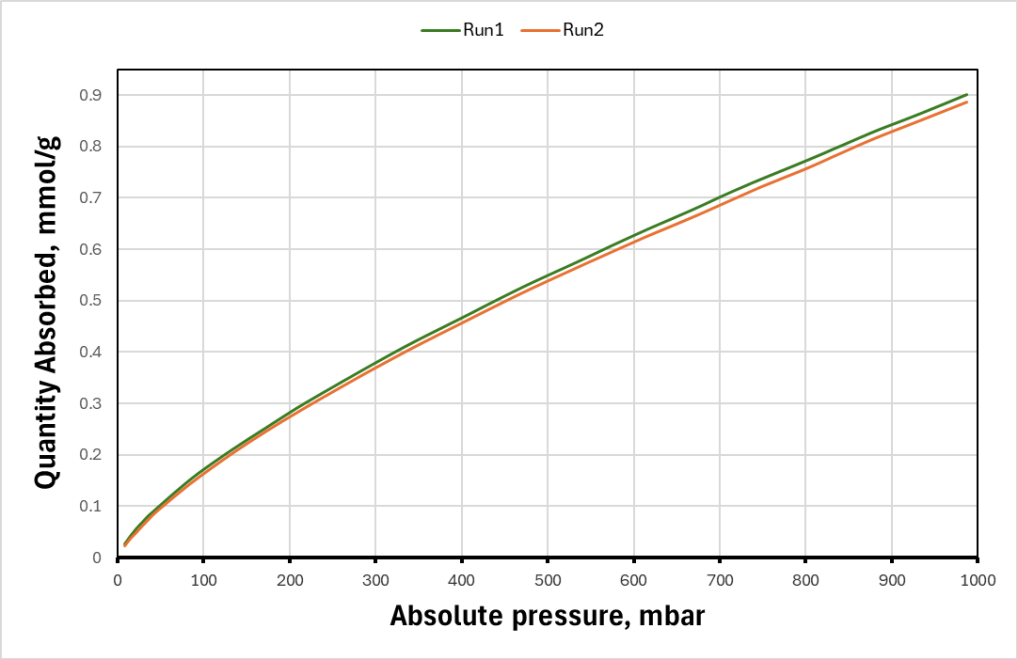

Figure 95: Run1 and Run2 of AlSi+APTES (2.5 mmol) sample.

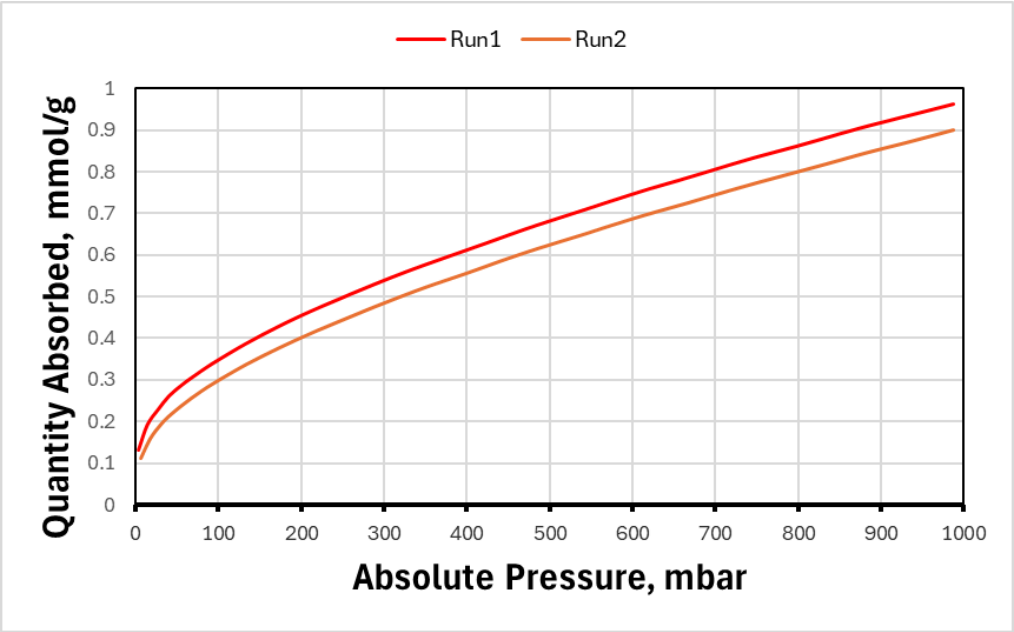

Figure 96: Run1 and Run2 of AlSi+APTES (7.5 mmol) sample.

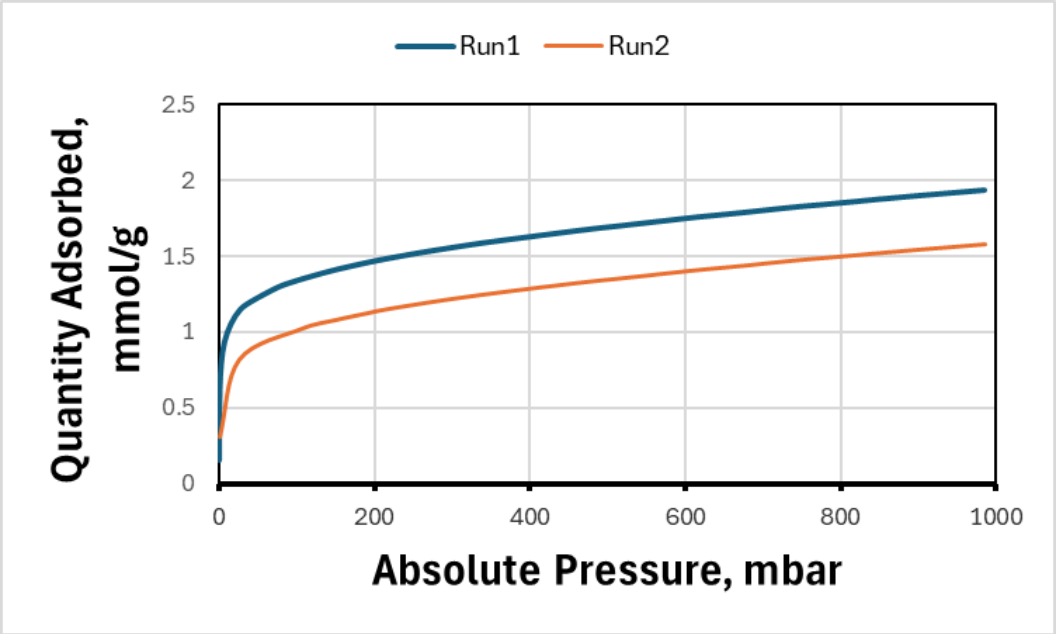

Figure 97: Run1 and Run2 of the AlSi-APTES (22.5 mmol) sample.

Figure 98 shows a comparison between the Run1 of *AlSi*, *AlSi+APTES (2.5 mmol)*, *AlSi+APTES (7.5 mmol)* and *AlSi-APTES (22.5 mmol)*. Negligible variances are observed in the total CO_2 adsorption between the samples *AlSi+APTES (2.5 mmol)* and *AlSi+APTES (7.5 mmol)*, suggesting that functionalisation with a low number of amino groups does not confer a discernible advantage at elevated partial pressures. However, at lower pressures, it is noteworthy that the initial trend of the 7.5 mmol sample diverges from that of the other samples: it exhibits a downward concavity, whereas the curves of the other two samples follow a more linear trajectory. The concavity in the 7.5 mmol sample reveals some affinity between the adsorbate and the surface and measured

values show that this sample adsorbs more CO_2 compared to the other samples at equivalent partial pressures.

The sample with the lowest amine content at low pressures does not show a higher absorption than that of the sample AlSi, while the 7.5 mmol (and 22.5 mmol) show a preferential absorption at low pressures. It can be hypothesized that this difference is because part of the amino groups in the functionalized samples is in protonated form and, therefore, not active for CO_2 capture (shown by XPS analyses, ***Figure 62***). By increasing the amino content of the samples, in addition to the protonated part, a part of non-protonated groups also appears (***Figure 82***). Precisely these groups are responsible for the preferential adsorption of CO_2.

Given that the 7.5 mmol sample exhibits greater adsorption than the AlSi reference at low pressures, this type of sample could be interesting for applications with gas flows in which the CO_2 concentration is low (perhaps also for DAC, Direct Ambient Capture). It is possible to say that 22.5 mmol is advantageous at both low and high pressures. The adsorption of *AlSi-APTES (22.5 mmol) samples* is higher than the other samples, indicating that the functionalisation can bring incredibly high adsorption of CO_2 if the number of APTES is sufficiently high (***Figure 98***).

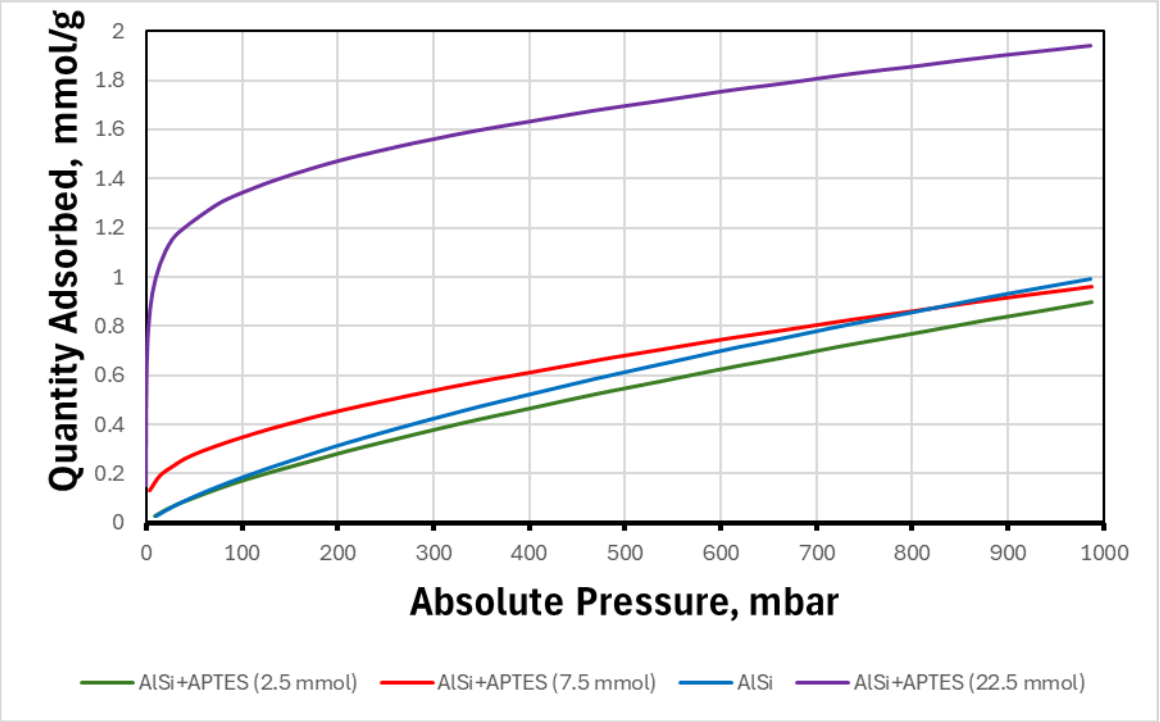

Figure 98: Comparison between Run1 of AlSi_APTES (2.5 mmol), AlSi_APTES (7.5 mmol), AlSi_APTES (22.5 mmol) and AlSi.

5.2 In-situ IR measurements

To assess the characteristics and reversibility of the compounds resulting from the interaction between primary amines distributed on the surface of the aerogels and carbon dioxide, in-situ infrared spectroscopy was employed. This methodology allowed for the identification of infrared absorption peaks corresponding to the species which appear during the interaction between the sample and CO_2, serving as indicators for chemisorbed species such as carbamic acid, ammonium carbamate, and carbonates.

5.2.1 Interaction with CO_2

Possible variations in the absorption spectrum associated with surface compounds present in the samples, such as primary amines and silanols, were observed during the adsorption process. If these species are involved in chemisorption phenomena, new bands of adsorption (such as those of carbamates) appear. Otherwise, in the case of physisorption, the original adsorption bands of the spectrum remained unchanged for each level of carbon dioxide pressure tested.

Given the intricacy of interpreting such analyses, wherein spectral variations are often subtle, it is advisable to subtract the spectrum of the original sample from each curve to emphasize differences in peak intensities or absorption bands relative to the baseline. In the case of primary amine and carbon dioxide interactions, the focus was directed towards spectral regions associated with amino group stretching and bending vibrations, typically around 3300 and 1600 cm^{-1} respectively.

For AlSi, only the appearance of the peak at 2340 cm^{-1} of molecular CO_2 is seen, indicating that only physisorption occurs (**Figure *99***) [42]. In the 2.5 mmol samples no signs of chemisorption are seen and this is consistent with what was observed with the volumetrics, where the AlSi-APTES (2.5 mmol) aerogels do not present preferential adsorption at low pressures (***Figure 100***). In the 7.5 mmol samples, in addition to the band at 2340 cm^{-1}, new bands also appear (around 3400 cm^{-1} and, above all, 1600 cm^{-1}) due to the formation of new species, such as carbamates, to indicate that in this case, both chemisorption and physisorption occur (***Figure 101***). Notably, distinct absorption peaks emerged in the lower wavenumber region (around 1600 cm^{-1}), indicating the formation of chemisorbed species like ammonium carbamate and carbamic acid, characterized by specific stretching and bending vibrations [42], [43], [44].

Figure *99*, **Figure *100***, and **Figure *101*** show also the difference curve for the aerogel samples and CO_2. The difference curves were calculated by subtracting from each spectrum collected the one

recorded for the aerogels at a partial pressure of anhydride carbon equal to zero. In the AlSi and 2.5 mmol samples only the peak of molecular CO_2 is highlighted, while in the 7.5 mmol sample, the appearance of new bands around 1600 cm^{-1} due to chemisorption is evident. As regards the curves obtained after degassing at room temperature, the AlSi sample and the 2.5 mmol sample immediately return to the starting conditions confirming that there are no irreversible phenomena (as seen with the volumetric adsorption tests).

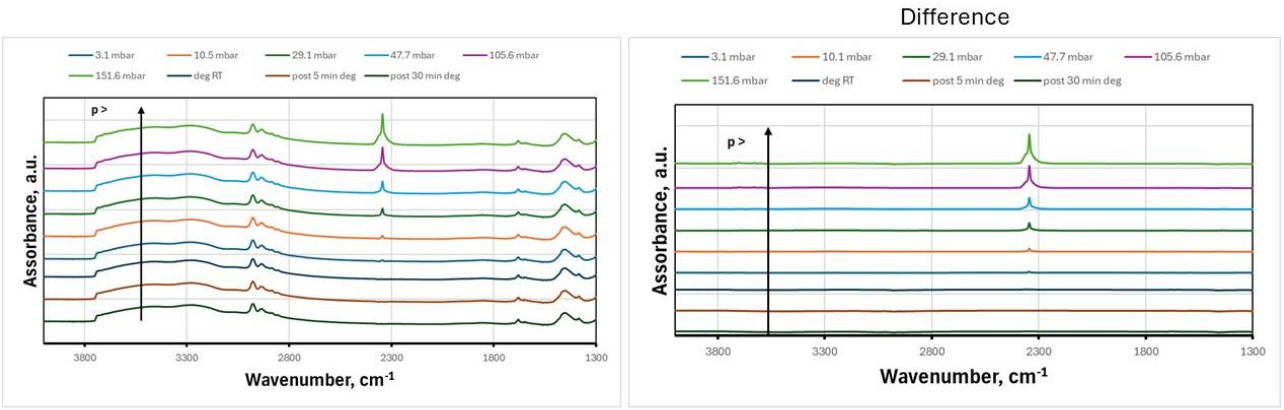

Figure 99: FTIR analysis and differences for the AlSi and CO_2 system at increasing equilibrium pressures.

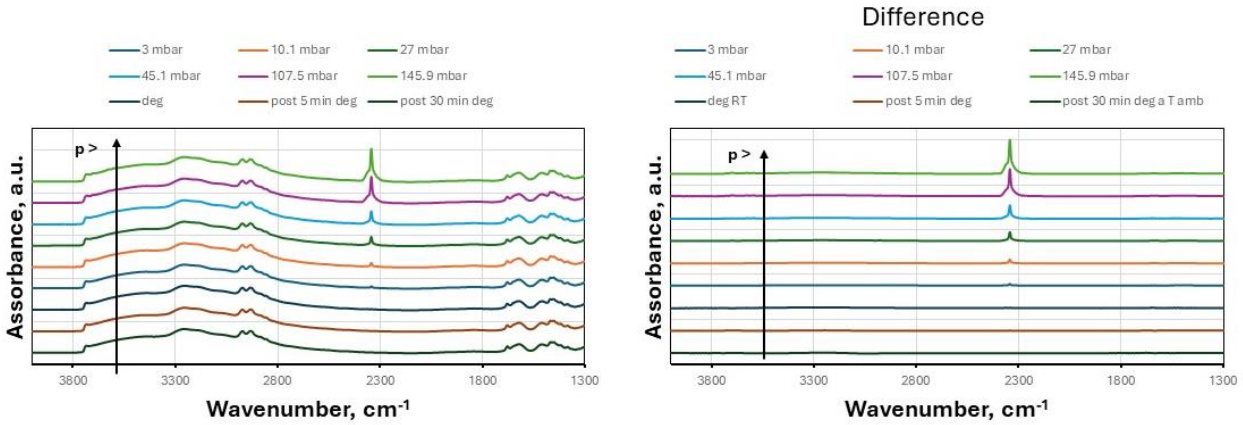

Figure 100: FTIR analysis and differences for the AlSi – APTES (2.5 mmol) and CO_2 system at increasing equilibrium pressures.

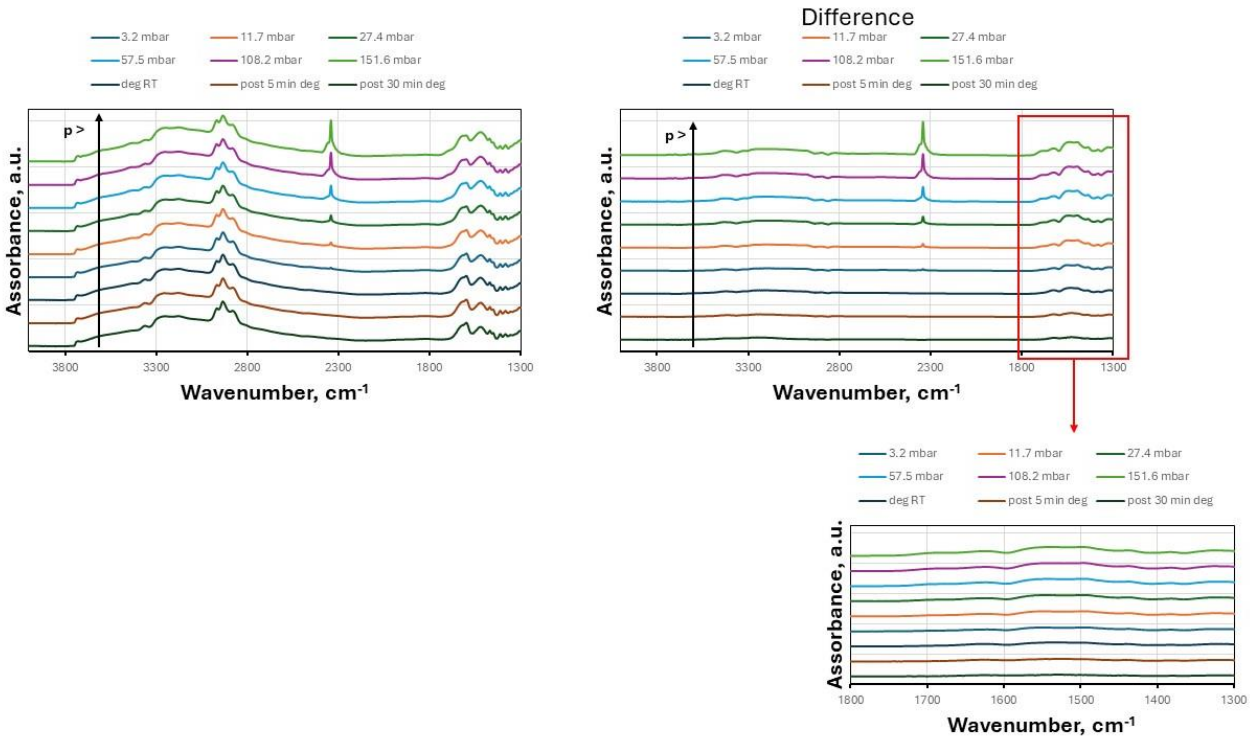

Figure 101: FTIR analysis and differences for the AlSi – APTES (7.5 mmol) and CO_2 system at increasing equilibrium pressures.

Conclusion

In conclusion, the urgent need for innovative and efficient technologies to mitigate the adverse effects of carbon dioxide emissions has led to the development of emerging CO_2 capture technologies. These technologies focus on solid and chemical adsorbents. Aerogels have emerged as exceptional materials with unique properties, including high surface area, low density, excellent thermal insulation, and adjustable porosity and surface chemistry, making them ideal candidates for developing next-generation adsorbents.

The versatility and controllability inherent in the sol-gel synthesis procedure have enabled the synthesis of aerogels from various precursors, including silica, metal oxides, and organic polymers. Supercritical drying, a controlled process, is widely employed for converting gels into aerogels, offering distinct advantages in aerogel production. This method minimizes the shrinkage of pore structure, preserving the high surface area and pore volumes essential for various applications.

The development of aerogels with tailored properties is critical for their effective application in CO_2 capture. For instance, functionalizing the silica matrix with metal oxides can significantly enhance the adsorption capacity and selectivity of aerogels. Additionally, the incorporation of organic components can improve the thermal insulation and mechanical properties of aerogels.

In this thesis, it was decided to study alumina-silica aerogels, as alumina can help the adsorption of CO_2 thanks to its basic character, and it can mechanically strengthen the aerogel. Furthermore, these aerogels were functionalised, via a one-pot procedure, with amino groups to further increase their effectiveness in capturing CO_2. The study delved into the adsorption of carbon dioxide on these novel alumina-silica aerogels functionalised with amino groups. The desired aerogels with increasing amine content have been successfully synthesised. These samples were characterized from a chemical-physical point of view to confirm their composition and textural properties. Two distinct steps were undertaken to investigate CO_2 adsorption on the aerogels, each designed to achieve specific research objectives. The first test aimed to quantify the amount of CO_2 adsorbed onto the samples by volumetric adsorption at room temperature, while the second test focused on examining the potential formation of new species when the sample interacts with CO_2. In both cases, a desorption step allowed the determination of possible species that remained permanently attached to the aerogel surface.

The volumetric results indicated that the maximum quantity of CO_2 adsorbed was approximately 1 mmol/g for the alumina-silica aerogels. Importantly, the study found that the two runs were superimposable, suggesting no irreversible adsorption phenomena were observed.

Additionally, the study compared the CO_2 adsorption performance of aerogels functionalized with different amounts of APTES (2.5 mol and 7.5 mol). The results showed that there were negligible variances in the total CO_2 adsorption between the samples, indicating that functionalization did not confer a discernible advantage at elevated partial pressures. However, at lower pressures, the aerogel sample with 7.5 mmol of APTES exhibited a downward concavity in its adsorption curve, suggesting preferential adsorption compared to the other samples at equivalent partial pressures. Furthermore, the study delved into the interaction between primary amines distributed on the surface of the aerogels and carbon dioxide. In-situ infrared spectroscopy was employed to assess the characteristics and reversibility of the chemisorbed compounds resulting from this interaction.

The analysis revealed the formation of chemisorbed species like carbamic acid, ammonium carbamate, and carbonates on functionalised samples with a high content of ammines (7.5 mmol and 22.5 mmol). Spectral variations were observed during the chemisorption process, emphasizing the active involvement of surface compounds like primary amines and silanols. On the opposite, pure physisorption was observed for the alumina-silica aerogel. In all cases, the adsorption phenomena were almost completely reversible in a few minutes of degassing at room temperature.

Overall, the detailed examination of the results of CO_2 adsorption on amino-functionalised alumina-silica aerogels provides valuable insights into the adsorption capacity, reversibility, and chemical interactions involved in the process, contributing to the understanding of the effectiveness of these materials for CO_2 capture applications. Regarding future prospects, it would be worth thinking about tests for evaluation of:

1. the selectivity of the synthesised samples. In this case, a mixture of different gases (for example CO_2 and N_2) is sent onto the samples and it is seen whether the samples selectively adsorb the CO_2 or both gases indiscriminately. For this purpose, it is possible to exploit the Ideal Adsorbed Solution Theory (IAST), a widely used predictive model for estimating multicomponent adsorption equilibrium and selectivity based solely on experimental single-component adsorption isotherms (N_2).

2. the effect of humidity on the effectiveness of the samples, given that some humidity is always present in exhaust gases. These tests could be done, in an exploratory manner, with in-situ FTIR.

3. the thermal stability of the samples, given that the regeneration processes of adsorbents are usually carried out at a temperature higher than the ambient temperature. It would be enough to do a

TGA with an isotherm at a pre-established T (for example 120-150°C) and see if the mass of the sample is stable or not.

Ringraziamenti

A **mamma e papà**, che hanno sempre fissato il loro sguardo su ogni mio traguardo, ancora prima che lo raggiungessi. Siete la gioia della mia vita. Mi sento ricca e completa perché ho voi.

A **mia sorella Paola**, mia fonte di vita e amica preziosa, che questo giorno possa essere per te di grande motivazione per il tuo futuro. Sei la migliore amica che ho sempre desiderato. Sei estremamente intelligente (e bella!) ed ogni tuo sogno si realizzerà proprio come vuoi tu.

Al **mio fidanzato Michele**, mio amore e sostenitore di vita e di questo meraviglioso percorso. La tua presenza costante è e sarà sempre indispensabile. Sei la persona più incredibile e meravigliosamente bella che io conosca, sia dentro che fuori. Lotterò insieme a te affinché il tuo sogno diventi il tuo lavoro. Non mi fermerò fino a quando tu non otterrai quello che vorrai.

A **Roberta**, amica preziosissima e rarissima. Sei la motivazione per cui riscelgierei il mio percorso di studi se dovessi tornare indietro. Il tuo sostegno è stato eccezionale e fondamentale. Mi hai sempre dato tanto senza pretendere niente in cambio. Grazie.

A voi dedico la mia vittoria e tutti i miei successi.

E a chi come me, nonostante ogni nonostante, ha dimostrato coraggio e costanza nell'inseguire i propri sogni.

L'obiettivo è raggiungerli, conquistarli e farli proprio ed io **ci sono riuscita ancora una volta**.

Un grazie particolare all'incredibile Marta e ai miei relatori: tutto questo non sarebbe mai stato possibile senza il vostro sostegno ed aiuto. Grazie.

References

[1] M. Meinshausen *et al.*, “Greenhouse-gas emission targets for limiting global warming to 2°C,” *Nature*, vol. 458, no. 7242, pp. 1158–1162, Apr. 2009, doi: 10.1038/nature08017.

[2] L. Keshavarz, M. R. Ghaani, J. M. D. MacElroy, and N. J. English, “A comprehensive review on the application of aerogels in CO2-adsorption: Materials and characterisation,” *Chemical Engineering Journal*, vol. 412. Elsevier B.V., May 15, 2021. doi: 10.1016/j.cej.2021.128604.

[3] L. Du, T. Lu, and B. Li, “CO2 capture and sequestration in porous media with SiO2 aerogel nanoparticle-stabilized foams,” *Fuel*, vol. 324, Sep. 2022, doi: 10.1016/j.fuel.2022.124661.

[4] J. Feng, L. Fan, M. Zhang, and M. Guo, “An efficient amine-modified silica aerogel sorbent for CO2 capture enhancement: Facile synthesis, adsorption mechanism and kinetics,” *Colloids Surf A Physicochem Eng Asp*, vol. 656, Jan. 2023, doi: 10.1016/j.colsurfa.2022.130510.

[5] B. Yay and N. Gizli, “A review on silica aerogels for CO2 capture applications,” *Pamukkale University Journal of Engineering Sciences*, vol. 25, no. 7, pp. 907–913, 2019, doi: 10.5505/pajes.2018.35651.

[6] Z. D. Shao, X. Cheng, and Y. M. Zheng, “Facile co-precursor sol-gel synthesis of a novel amine-modified silica aerogel for high efficiency carbon dioxide capture,” *J Colloid Interface Sci*, vol. 530, pp. 412–423, Nov. 2018, doi: 10.1016/j.jcis.2018.06.094.

[7] A. Soleimani Dorcheh and M. H. Abbasi, “Silica aerogel; synthesis, properties and characterization,” *Journal of Materials Processing Technology*, vol. 199, no. 1. pp. 10–26, Apr. 01, 2008. doi: 10.1016/j.jmatprotec.2007.10.060.

[8] C. M. R. Almeida, M. E. Ghica, and L. Durães, “An overview on alumina-silica-based aerogels,” *Advances in Colloid and Interface Science*, vol. 282. Elsevier B.V., Aug. 01, 2020. doi: 10.1016/j.cis.2020.102189.

[9] G. Guzel Kaya and H. Deveci, “Synergistic effects of silica aerogels/xerogels on properties of polymer composites: A review,” *Journal of Industrial and Engineering Chemistry*, vol. 89. Korean Society of Industrial Engineering Chemistry, pp. 13–27, Sep. 25, 2020. doi: 10.1016/j.jiec.2020.05.019.

[10] V. Yashvanth and S. Chowdhury, “An investigation of silica aerogel to reduce acoustic crosstalk in cmut arrays,” *Sensors*, vol. 21, no. 4, pp. 1–16, Feb. 2021, doi: 10.3390/s21041459.

[11] J. Yang, Q. Wang, T. Wang, and Y. Liang, “Facile one-step precursor-to-aerogel synthesis of silica-doped alumina aerogels with high specific surface area at elevated temperatures,” *Journal of Porous Materials*, vol. 24, no. 4, pp. 889–897, Aug. 2017, doi: 10.1007/s10934-016-0328-3.

[12] R. Saliger, T. Heinrich, T. Gleissner, and J. Fricke, “Sintering behaviour of alumina-modified silica aerogels,” 1995.

[13] H. Fan, Z. Wu, Q. Xu, and T. Sun, “Flexible, amine-modified silica aerogel with enhanced carbon dioxide capture performance,” *Journal of Porous Materials*, vol. 23, no. 1, pp. 131–137, Feb. 2016, doi: 10.1007/s10934-015-0062-2.

[14] L. Pires da Mata Costa *et al.*, “Capture and reuse of carbon dioxide (Co2) for a plastics circular economy: A review,” *Processes*, vol. 9, no. 5. MDPI AG, 2021. doi: 10.3390/pr9050759.

[15] N. Hedin and Z. Bacsik, “Perspectives on the adsorption of CO2 on amine-modified silica studied by infrared spectroscopy,” *Current Opinion in Green and Sustainable Chemistry*, vol. 16. Elsevier B.V., pp. 13–19, Apr. 01, 2019. doi: 10.1016/j.cogsc.2018.11.010.

[16] M. Shen, X. Jiang, M. Zhang, and M. Guo, “Synthesis of SiO2–Al2O3 composite aerogel from fly ash: a low-cost and facile approach,” *J Solgel Sci Technol*, vol. 93, no. 2, pp. 281–290, Feb. 2020, doi: 10.1007/s10971-019-05204-y.

[17] C. Chen *et al.*, “Template-directed fabrication of MIL-101(Cr)/mesoporous silica composite: Layer-packed structure and enhanced performance for CO2 capture,” *J Colloid Interface Sci*, vol. 513, pp. 891–902, Mar. 2018, doi: 10.1016/j.jcis.2017.12.014.

[18] R. Serna-Guerrero and A. Sayari, “Modeling adsorption of CO2 on amine-functionalized mesoporous silica. 2: Kinetics and breakthrough curves,” *Chemical Engineering Journal*, vol. 161, no. 1–2, pp. 182–190, 2010, doi: 10.1016/j.cej.2010.04.042.

[19] S. N. Kim, W. J. Son, J. S. Choi, and W. S. Ahn, “CO2 adsorption using amine-functionalized mesoporous silica prepared via anionic surfactant-mediated synthesis,” *Microporous and Mesoporous Materials*, vol. 115, no. 3, pp. 497–503, Nov. 2008, doi: 10.1016/j.micromeso.2008.02.025.

[20] G. P. Knowles, J. V. Graham, S. W. Delaney, and A. L. Chaffee, “Aminopropyl-functionalized mesoporous silicas as CO2 adsorbents,” in *Fuel Processing Technology*, Oct. 2005, pp. 1435–1448. doi: 10.1016/j.fuproc.2005.01.014.

[21] L. Li, B. Yalcin, B. N. Nguyen, M. A. B. Meador, and M. Cakmak, “Flexible nanofiber-reinforced aerogel (Xerogel) synthesis, manufacture, and characterization,” *ACS Appl Mater Interfaces*, vol. 1, no. 11, pp. 2491–2501, Nov. 2009, doi: 10.1021/am900451x.

[22] L. Li, B. Yalcin, B. N. Nguyen, M. A. B. Meador, and M. Cakmak, “Flexible nanofiber-reinforced aerogel (Xerogel) synthesis, manufacture, and characterization,” *ACS Appl Mater Interfaces*, vol. 1, no. 11, pp. 2491–2501, Nov. 2009, doi: 10.1021/am900451x.

[23] S. Mulik, C. Sotiriou-Leventis, G. Churu, H. Lu, and N. Leventis, “Cross-linking 3D assemblies of nanoparticles into mechanically strong aerogels by surface-initiated free-radical polymerization,” *Chemistry of Materials*, vol. 20, no. 15, pp. 5035–5046, Aug. 2008, doi: 10.1021/cm800963h.

[24] J. P. Randall, M. A. B. Meador, and S. C. Jana, “Polymer reinforced silica aerogels: Effects of dimethyldiethoxysilane and bis(trimethoxysilylpropyl)amine as silane precursors,” *J Mater Chem A Mater*, vol. 1, no. 22, pp. 6642–6652, Jun. 2013, doi: 10.1039/c3ta11019b.

[25] T. Błaszczyński, A. Ślosarczyk, and M. Morawski, “Synthesis of silica aerogel by supercritical drying method,” in *Procedia Engineering*, Elsevier Ltd, 2013, pp. 200–206. doi: 10.1016/j.proeng.2013.04.028.

[26] C. A. García-González, M. C. Camino-Rey, M. Alnaief, C. Zetzl, and I. Smirnova, “Supercritical drying of aerogels using CO 2: Effect of extraction time on the end material textural properties,” *Journal of Supercritical Fluids*, vol. 66, pp. 297–306, Jun. 2012, doi: 10.1016/j.supflu.2012.02.026.

[27] L. M. Sanz-Moral, M. Rueda, R. Mato, and Á. Martín, “View cell investigation of silica aerogels during supercritical drying: Analysis of size variation and mass transfer mechanisms,” *Journal of Supercritical Fluids*, vol. 92, pp. 24–30, 2014, doi: 10.1016/j.supflu.2014.05.004.

[28] C. A. García-González, M. C. Camino-Rey, M. Alnaief, C. Zetzl, and I. Smirnova, “Supercritical drying of aerogels using CO 2: Effect of extraction time on the end material textural properties,” *Journal of Supercritical Fluids*, vol. 66, pp. 297–306, Jun. 2012, doi: 10.1016/j.supflu.2012.02.026.

[29] R. Al-Oweini and H. El-Rassy, “Synthesis and characterization by FTIR spectroscopy of silica aerogels prepared using several Si(OR)4 and R′′Si(OR′)3 precursors,” *J Mol Struct*, vol. 919, no. 1–3, pp. 140–145, Feb. 2009, doi: 10.1016/j.molstruc.2008.08.025.

[30] O. Slimi, D. Djouadi, L. Hammiche, A. Chelouche, and T. Touam, “Structural and optical properties of Cu doped ZnO aerogels synthesized in supercritical ethanol,” *Journal of Porous Materials*, vol. 25, no. 2, pp. 595–601, Apr. 2018, doi: 10.1007/s10934-017-0472-4.

[31] S. A. El-Safty and J. Evans, “Formation of highly ordered mesoporous silica materials adopting lyotropic liquid crystal mesophases,” *J Mater Chem*, vol. 12, no. 1, pp. 117–123, 2002, doi: 10.1039/b106077p.

[32] P. C. A. Alberius, K. L. Frindell, R. C. Hayward, E. J. Kramer, G. D. Stucky, and B. F. Chmelka, “General predictive syntheses of cubic, hexagonal, and lamellar silica and titania mesostructured thin films,” *Chemistry of Materials*, vol. 14, no. 8, pp. 3284–3294, Aug. 2002, doi: 10.1021/cm011209u.

[33] I. Honma, H. S. Zlion, D. Kimdn, and D. Endo, “Structural control of surfactant-templated hexagonal,cubic, and lamellar mesoporous silicate thin films prepared by spin-casting,” *Advanced Materials*, vol. 12, no. 20, pp. 1529–1533, Oct. 2000, doi: 10.1002/1521-4095(200010)12:20<1529::AID-ADMA1529>3.0.CO;2-U.

[34] I. L. Hyung, M. K. Ji, and G. D. Stucky, “Periodic mesoporous organosilica with a hexagonally pillared lamellar structure,” *J Am Chem Soc*, vol. 131, no. 40, pp. 14249–14251, Oct. 2009, doi: 10.1021/ja905245u.

[35] A. J. Karkamkar, S. S. Kim, S. D. Mahanti, and T. J. Pinnavaia, “Lamellar mesostructured silicas with chemically significant hierarchical morphologies,” *Adv Funct Mater*, vol. 14, no. 5, pp. 507–512, May 2004, doi: 10.1002/adfm.200305085.

[36] R. E. Morsi and R. S. Mohamed, “Nanostructured mesoporous silica: Influence of the preparation conditions on the physical-surface properties for efficient organic dye uptake,” *R Soc Open Sci*, vol. 5, no. 3, Mar. 2018, doi: 10.1098/rsos.172021.

[37] H.-Y. Lin and Y.-W. Chen, “Preparation of Spherical Hexagonal Mesoporous Silica,” 2005.

[38] N. M. Figueiredo, N. J. M. Carvalho, and A. Cavaleiro, “An XPS study of Au alloyed Al-O sputtered coatings,” *Appl Surf Sci*, vol. 257, no. 13, pp. 5793–5798, Apr. 2011, doi: 10.1016/j.apsusc.2011.01.104.

[39] M. P. Seah, “The quantitative analysis of surfaces by XPS: A review,” *Surface and Interface Analysis*, vol. 2, no. 6, pp. 222–239, 1980, doi: 10.1002/sia.740020607.

[40] H. Tamon, T. Sone, M. Mikami, and M. Okazaki, “Preparation and Characterization of Silica-Titania and Silica-Alumina Aerogels,” 1997.

[41] S. Iswar, W. J. Malfait, S. Balog, F. Winnefeld, M. Lattuada, and M. M. Koebel, “Effect of aging on silica aerogel properties,” 2016.

[42] J. L. R. Silveira, S. R. Dib, and A. M. Faria, “New support for high-performance liquid chromatography based on silica coated with alumina particles,” *Analytical Sciences*, vol. 30, no. 2, pp. 285–291, 2014, doi: 10.2116/analsci.30.285.

[43] J. Shen, Y. N. Wu, B. Zhang, and F. Li, “Preparation of mesoporous silica nanosheets through electrospinning: A novel scroll mechanism,” *RSC Adv*, vol. 4, no. 25, pp. 12805–12808, 2014, doi: 10.1039/c3ra47504b.

[44] Y. Tkachenko and P. Niedzielski, “FTIR as a Method for Qualitative Assessment of Solid Samples in Geochemical Research: A Review,” *Molecules*, vol. 27, no. 24. MDPI, Dec. 01, 2022. doi: 10.3390/molecules27248846.

[45] W. T. Al-Rubayee, O. F. Abdul-Rasheed, and N. M. Ali, “Preparation of a Modified Nanoalumina Sorbent for the Removal of Alizarin Yellow R and Methylene Blue Dyes from Aqueous Solutions,” *J Chem*, vol. 2016, 2016, doi: 10.1155/2016/4683859.

[46] F. Chen and M. Liu, “Preparation of mesoporous yttria-stabilized zirconia (YSZ) and YSZ-NiO using a triblock copolymer as surfactant,” *J Mater Chem*, vol. 10, no. 11, pp. 2603–2605, 2000, doi: 10.1039/b006561g.

[47] “The Colloid Chemistry of Silica.” [Online]. Available: https://pubs.acs.org/sharingguidelines

[48] W. Trisunaryanti, S. Larasati, T. Triyono, N. R. Santoso, and C. Paramesti, “Selective production of green hydrocarbons from the hydrotreatment of waste coconut oil over Ni- And NiMo-supported on amine-functionalized mesoporous silica,” *Bulletin of Chemical Reaction Engineering and Catalysis*, vol. 15, no. 2, pp. 415–431, Apr. 2020, doi: 10.9767/bcrec.15.2.7136.415-431.

[49] M. Thommes *et al.*, “Physisorption of gases, with special reference to the evaluation of surface area and pore size distribution (IUPAC Technical Report),” *Pure and Applied Chemistry*, vol. 87, no. 9–10, pp. 1051–1069, Oct. 2015, doi: 10.1515/pac-2014-1117.

[50] S. Brunauer, P. H. Emmett, and E. Teller, “Adsorption of Gases in Multimolecular Layers,” 1938. [Online]. Available: https://pubs.acs.org/sharingguidelines

[51] E. P. Barrett, L. G. Joyner, P. P. Halenda Vol, R. -RnAtn Apj, and R. A. Vn-Rn Atn Ac, “Vp2 = R2AV2-R2AT2 ACi Generalizing equation (4) and substituting (6a) for Vm* yields.”

[52] K. Djebaili, Z. Mekhalif, A. Boumaza, and A. Djelloul, “XPS, FTIR, EDX, and XRD analysis of Al2O3 scales grown on PM2000 alloy,” *Journal of Spectroscopy*, vol. 2015, 2015, doi: 10.1155/2015/868109.

[53] T. TAGO, N. KATAOKA, H. TANAKA, K. KINOSHITA, and S. KISHIDA, “XPS study from a clean surface of Al2O3 single crystals,” *Procedia Eng*, vol. 216, pp. 175–181, 2017, doi: 10.1016/j.proeng.2018.02.081.

[54] W. Zhu *et al.*, “Preparation of an Amine-Modified Cellulose Nanocrystal Aerogel by Chemical Vapor Deposition and Its Application in CO2Capture,” *Ind Eng Chem Res*, vol. 59, no. 38, pp. 16660–16668, Sep. 2020, doi: 10.1021/acs.iecr.0c02687.

[55] D. Brunel *et al.*, “Spectroscopic Studies on Aminopropyl-containing Micelle Templated Silicas. Comparison of grafted and co-condensation routes.”

[56] J. W. Bekina, “Low temperature deposition of photocatalytically active TiO2 coatings on polymers.” [Online]. Available: https://www.researchgate.net/publication/312784742

[57] H. Lei and P. Zhang, “Preparation of alumina/silica core-shell abrasives and their CMP behavior,” *Appl Surf Sci*, vol. 253, no. 21, pp. 8754–8761, Aug. 2007, doi: 10.1016/j.apsusc.2007.04.079.